Master Thesis

Precision calculations of QCD processes for the ATLAS experiment at $\sqrt{s} = 7$ TeV

Université de Genève

S. K. Argyropoulos

Geneva 2012

This work has been carried out in the Department of Nuclear and Particle Physics of the University of Geneva from June to December 2011.

I want to thank Giuseppe Iacobucci and Allan Clark for hiring me as a student in the Geneva ATLAS Group and also Alessandro Bravar for accepting to review this thesis.

I owe my deepest gratitude to William Bell for supervising this thesis on a day-to-day basis and from whom I have learnt a great deal not only about the LHC physics but also about how one should work in an experimental collaboration.

I am grateful to Alison Lister for supervising my work when Will was away and for her help and advice on the PhD search. I would also like to thank Paul Bell for getting me started with the Alpgen production.

Many thanks to Kilian Rosbach and Valerio Dao, who were always willing to offer programming and debugging advice that has been critical for getting me unstuck in various stages of this work. Thanks to Ian Watson for sharing his Python expertise, which helped me to write the LHEF splitters. Thanks to Gaetano Barone for his advice on writing the thesis and the presentation.

I would also like to thank Catherine Blanchard for her help with administrative matters and all of my colleagues in the Geneva ATLAS group for creating an excellent and inspiring working atmosphere at CERN.

People from the aMC@NLO team deserve a special mention: Stefano Frixione for his availability and willingness to answer a lot of my questions concerning QCD calculations and for cross-checking the produced samples, Rikkert Frederix for his critical help on running and modifying the aMC@NLO software and Valentin Hirschi, with whom I have passed a considerable amount of time, trying to track down the FPE in MadLoop.

I have to acknowledge the help of M.L. Mangano in clarifying some delicate matters concerning the matching procedure in Alpgen and I also thank Małgorzata Worek for proposing the study carried out in the third chapter of this thesis.

I feel indebted to James Ferrando for his willingness and quickness to respond to my questions about the Alpgen production and for providing the $t\bar{t}+\mathrm{jets}$ *samples that were used in this thesis. I also thank Liza Mijovic for her helpful instructions on how to run HERWIG through the Athena framework.*

I have to thank Claire Gwenlan, Peter Loch and Andy Buckley for getting me involved in aMC@NLO and for proposing such an interesting topic for my qualification task.

I owe a big thanks to Nikolaos Rompotis, who has challenged and enriched my understanding of particle physics during our numerous discussions and for all the good times that we had in Geneva. Many thanks to Ahmad, Lazaros and Anna, without whom life in Lyon would have been unbearable. $\aleph_0$ *thanks to Katerina for all the ways, in which she has made my life better all these years.*

I also have to thank my family for their practical and moral support, particularly during my stay abroad.

S.K.A.

CONTENTS

Abstract **iv**

1 THEORETICAL INTRODUCTION **1**
- 1.1 The Standard Model 1
- 1.2 QCD as the gauge theory of strong interactions 3
  - 1.2.1 Perturbative QCD 4
  - 1.2.2 From partons to hadrons 5
- 1.3 Going beyond the LO approximation 8
  - 1.3.1 NLO corrections and associated divergences 9
  - 1.3.2 The Parton Shower approach 10
  - 1.3.3 Jets and Jet Algorithms 14
  - 1.3.4 Matching ME and PS calculations 16
- 1.4 Monte Carlo Generators 20
- 1.5 Parameter inputs for MC11 production in ATLAS with aMC@NLO 21

2 THE ATLAS EXPERIMENT **23**
- 2.1 The LHC 23
- 2.2 The ATLAS detector 24
- 2.3 Trigger 25
- 2.4 Coordinate system 26

3 STUDY OF THE INFRARED AND COLLINEAR REGION IN $t\bar{t}jj$ EVENTS **29**
- 3.1 Motivation 29
- 3.2 Matrix element calculation 31
- 3.3 Study of infrared and collinear divergences 32
- 3.4 Conclusions 34

4 CALCULATION OF $Wb\bar{b}$ WITH aMC@NLO **35**
- 4.1 Motivation 35
- 4.2 The aMC@NLO framework and details on the calculation 35
- 4.3 Consistency checks on the $Z/\gamma^* b\bar{b}$ sample 37
- 4.4 Results from the $Wb\bar{b}$ calculation with the ATLAS MC11 defaults 37
- 4.5 Comparison with ATLAS data 40

Summary and Prospects **49**

A Input parameters for the generation of the $t\bar{t}+$ jets and $Wb\bar{b}$ samples **51**
- A.1 Alpgen parameters 51
- A.2 HERWIG parameters for $Z/\gamma^* b\bar{b}$ showering and hadronization 51
- A.3 aMC@NLO parameters for $Wb\bar{b}$ generation with the ATLAS MC11 defaults 52

References **55**

ABSTRACT

The goal of this thesis is twofold: (i) the study of the infrared and collinear region in $t\bar{t}jj$ events and (ii) the NLO calculation of $Wb\bar{b}$ with the aMC@NLO software for the ATLAS experiment. An overview of the Standard Model with particular emphasis on QCD is given and the theoretical tools used in precision QCD calculations are presented. The LHC accelerator and the ATLAS detector and Data Acquisition System are briefly described. The soft and collinear region in $t\bar{t}jj$ events is studied using matrix element and parton-shower calculations provided by Alpgen and HERWIG. The region of dominance of the two components is established, by comparing the matrix element with the parton-shower spectra. After a brief description of the aMC@NLO generator, a consistency check is performed on an existing $Z/\gamma^* b\bar{b}$ parton-level sample. This consists in reproducing the results found in [1]. A NLO calculation of $Wb\bar{b}$ including an off-diagonal CKM matrix and decays to all lepton families is presented. The calculation assumes massive b quarks and also includes spin-correlations and off-shell effects, as presented in [1]. The aMC@NLO prediction for $Wb\bar{b}$ production is compared against the recent ATLAS measurement [2] of the cross section for the production of a W boson in association with one or two b jets.

Chapter 1

THEORETICAL INTRODUCTION

> "*Had I foreseen that, I would have gone into botany.*"
> Attributed to W. Pauli.

1.1 The Standard Model

Our current understanding of High Energy Physics can be summarized in the theory known as the Standard Model [3]. The Standard Model describes collectively the electromagnetic, weak and strong interactions between the fundamental constituents of matter, quarks and leptons. In mathematical terms, the Standard Model is a non-Abelian gauge theory based on the symmetry group $SU(3) \times SU(2)_L \times U(1)_Y$. As a gauge theory, the Standard Model is based on the fundamental concept of gauge symmetries. Unlike global symmetries, gauge symmetries are not new symmetries of nature, in the sense that they don't imply the existence of new conserved charges. However, their existence is of a much deeper significance, since they determine in a unique way how the the fields (particles) interact.

The development of the Standard Model proved to be difficult, due to the fact that gauge symmetries can be broken, i.e. they may not be manifest in physical observables. Symmetry breaking in the form of phase transitions was well known in classical physics and had been formalized by Landau [4, 5]. Considering for instance a ferromagnet, we know that, above the Curie temperature, the net magnetization is zero, the spins are randomly oriented and the system displays a symmetry under $SO(3)$ transformations (3-dimensional rotations). Below the Curie temperature, the system obtains a net magnetization with the spins pointing along a certain direction and the symmetry being reduced ("broken") from $SO(3)$ to $SO(2)$ (rotations about the external field direction). In this less symmetric phase, one needs additional degrees of freedom[1] in order to describe the system. These have been dubbed *order parameters*. In an analogous way, Higgs, Brout, Englert, Guralnik, Hagen and Kibble proposed a way to apply these principles in systems of quantum fields [6–10]. Glashow, Weinberg and Salam then applied the idea of symmetry breaking into the description of the electromagnetic and weak interactions as a unified gauge field theory.

In the *electroweak theory* [11–13], one starts from a symmetric phase which is invariant under the transformations of the gauge group $SU(2)_L \times U(1)_Y$, where $Y = 2(Q - I_3)$ is the hypercharge, Q is the charge and I_3 the projection of the isospin along the z axis. Along with the electroweak gauge bosons, the electroweak theory predicts the existence of a scalar field (dubbed the *Higgs field*), which plays the role of the order parameter of the theory. Below a certain energy scale, the Higgs field acquires a non-zero vacuum expectation value and the $SU(2)_L \times U(1)_Y$ symmetry is broken down to $U(1)_Q$, which is the gauge symmetry of electromagnetism. In the process, the weak bosons acquire masses and appear thus to be non-invariant under the gauge transformations. The electroweak theory has been consolidated by the discovery of the neutral current interactions and the W and Z bosons by the Gargamelle and UA1 experiments at CERN. This paved the way towards the construction of the Standard Model, which started with the works of Glashow, Weinberg and Salam [11–13].

---

[1] In this case the net magnetization.

The development of Quantum Chromodynamics (QCD) as the gauge theory of strong interactions began with the introduction of the quark model for the classification of hadron resonances [14, 15]. The colour charge was introduced as a new degree of freedom in an attempt to solve the Δ^{++} puzzle, i.e. to allow for the existence of resonances with antisymmetric wave-functions comprised of three quarks with identical flavour and spin [16]. The measurement of the cross-section ratio $\sigma(e^-e^+ \to \text{hadrons})/\sigma(e^-e^+ \to \mu^-\mu^+)$ at SLAC [17] provided evidence for the existence of three colours and the discovery of 3-jet events in e^-e^+ collisions by the TASSO experiment at DESY [18] established the existence of gluons thus proving that the strong interactions could be described as a gauge theory with a $SU(3)$ symmetry group.

The Standard Model accommodates twelve fundamental fermions of spin 1/2 that are divided into two categories - leptons which do not interact with strong interactions and quarks which interact with strong interactions and come in three colours - and three generations, as shown in Table 1.1. To each of these particles one associates an antiparticle by charge conjugation. The fundamental fermions are described by different representations of the Standard Model gauge group $G_{SM} = SU(3) \times SU(2)_L \times U(1)_Y$. Right-handed quarks and right-handed leptons are $SU(2)$ singlets and the right-handed neutrinos are G_{SM} singlets. Fermion interactions are mediated by the gauge bosons shown in Table 1.2, that transform under the adjoint representation[2] of G_{SM}. The Standard Model also predicts the existence of a Higgs boson, which is a spin 0 $SU(2)$ doublet with weak hypercharge $Y = -1$. Its discovery is the main goal of the physics program of the LHC.

TABLE 1.1: The Standard Model fermion families.

Fermion Generation	Leptons	Quarks
I	e_L^- $\nu_{e,L}$	u^r, u^g, u^b d^r, d^g, d^b
II	μ_L^- $\nu_{\mu,L}$	c^r, c^g, c^b s^r, s^g, s^b
III	τ_L^- $\nu_{\tau,L}$	t^r, t^g, t^b b^r, b^g, b^b

TABLE 1.2: The Standard Model gauge bosons.

Interaction	Gauge Boson
Electromagnetic	γ
Weak	$W^{\pm}, Z^0$
Strong	$g_1, \ldots, g_8$

---

[2] The adjoint representation is the representation whose matrix elements are given by the structure constants of the algebra.

1.2 QCD as the gauge theory of strong interactions

The QCD Lagrangian is comprised of two parts: the part that describes the gauge bosons (gluons) and the part that describes the fermions which transform in a representation of the gauge group (quarks). One can schematically write[3]

$$\mathcal{L}^0_{QCD} = \mathcal{L}^0_{YM} + \mathcal{L}^0_{Dirac}, \tag{1.1}$$

with

$$\begin{aligned} \mathcal{L}^0_{YM} &= -\frac{1}{4}\mathrm{Tr}\left[F^0_{\mu\nu}F^{0,\mu\nu}\right], \qquad (1.2)\\ \mathcal{L}^0_{Dirac} &= \sum_i \bar{\Psi}_i \left(i\partial\!\!\!/ - m_i\right)\Psi_i, \qquad (1.3) \end{aligned}$$

where $F^{0,\mu\nu}_{\alpha} = \partial^\mu A^\nu_\alpha - \partial^\nu A^\mu_\alpha$ is the *field strength* and the indices a and i run over the colour charges and the fermion flavours respectively. This Lagrangian describes freely propagating gluons and quarks without interactions and it is not invariant under $SU(3)$ gauge transformations. By introducing a local infinitesimal $SU(3)$ transformation on the quark fields $\Psi'_i = \exp\left(ig\lambda^a \left[t_a\right]^j_i\right)\Psi_j$,

$$\Psi'_i - \Psi_i = \delta\Psi_i = ig\lambda^a(x)\left[t_a\right]^j_i \Psi_j, \tag{1.4}$$

where t_a are the $SU(3)$ generators[4]. Then

$$\partial_\mu(\delta\Psi_i) = ig\lambda^a\left[t_a\right]^j_i \partial_\mu\Psi_j + ig\left(\partial_\mu\lambda^a\right)\left[t_a\right]^j_i\Psi_j, \tag{1.5}$$

with the second term in (1.5) spoiling the gauge invariance. In order to restore the gauge invariance, one has to replace ∂_μ with the *covariant derivative* $\nabla_\mu \equiv \partial_\mu - igA^a_\mu\left[t_a\right]^j_i$, where A^a_μ must transform according to[5]

$$\begin{aligned} \delta A^a_\mu &= \partial_\mu\Lambda^a + ig\left[\Lambda, A_\mu\right]\\ &= \partial_\mu\Lambda^a + gC^a_{bc}\Lambda^c A^b_\mu \equiv \nabla_\mu\Lambda^a. \qquad (1.6) \end{aligned}$$

Thus demanding invariance under local $SU(3)$ transformations leads to the introduction of a new gauge field which has to transform in the adjoint representation of the gauge group[6] as dictated by (1.6). With this modification, the interacting QCD Lagrangian becomes

$$\begin{aligned} \mathcal{L}_{QCD} &= -\frac{1}{4}\mathrm{Tr}\left[F_{\mu\nu}F^{\mu\nu}\right] + \sum_i \bar{\Psi}_i\left(i\nabla\!\!\!\!/ - m_i\right)\Psi_i, \qquad (1.7)\\ F_{\mu\nu} &= \nabla_\mu A_\nu - \nabla_\nu A_\mu = \partial_\mu A_\nu - \partial_\nu A_\mu - ig\left[A_\mu, A_\nu\right]. \qquad (1.8) \end{aligned}$$

Intuitively, one can picture the gauging procedure described above by drawing an analogy to general relativity. In order to compare vectors attached to different points on a curved surface, one has to introduce the notion of parallel transport. The effects of the parallel transport from point to point can then be described by the Christoffel symbols (affine connection). Also parallel transport along a closed contour provides a measure of the curvature of space-time and is described by the Riemann curvature tensor. An analogous picture for QCD is illustrated in Fig. 1.1. The QCD fields take values on a *base space*, which is the 4-dimensional Minkowski space-time of special relativity. At every space-time point there is a *fibre*, that is a copy of the gauge group $SU(3)$. In order to compare quark fields at different space-time points, one has to introduce a *connection*, namely the gluon fields, that determines how the quark fields must be transported from one point to another. In this sense, the analogues of the Christoffel symbols are given by the gluon fields and the analogue of the curvature is given by the field strength $F_{\mu\nu}$.

---

[3] Upon attempting to quantize the QCD Lagrangian, one has to add an additional gauge fixing term, in order to eliminate unphysical degrees of freedom from the spectrum. This is not of crucial importance for the following discussion and will not be treated here.

[4] We remind that a well-known representation of t_a is given by the Gell-Mann matrices.

[5] In matrix notation we have $\Lambda_{ij} = \lambda^a\left[t_a\right]^j_i$ and $A^{ij}_\mu = \left[A^a_\mu t_a\right]^j_i$. By definition, the covariant derivative must satisfy $\delta(\nabla_\mu\Psi_i) = ig\Lambda^j_i(\nabla_\mu\Psi_j)$.

[6] The adjoint representation is defined by $\left[t_a\right]^c_b \equiv iC^c_{ab}$, where C^c_{ab} are the structure constants of the gauge group.

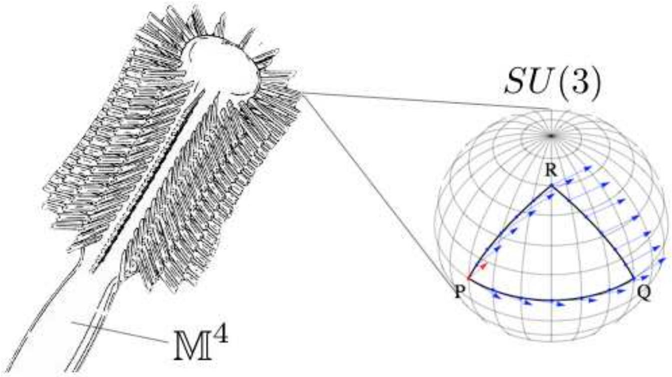

FIGURE 1.1: QCD as a hairbrush (*fibre bundle*). The handle (*base space*) is identified with the 4-dimensional Minkowski space-time and the bristles (*fibres*) are identified with the $SU(3)$ group. The gauge fields (*connection*) determine how quark fields are parallel-transported from point to point.

1.2.1 Perturbative QCD

From (1.7),(1.8) one can derive the Feynman rules for QCD [19]. These rules are depicted in Fig. 1.2. The gluon, quark and ghost propagators in a covariant gauge are,

$$D^{\mu\nu}_{ba}(k) = i\frac{\delta_{ba}}{k^2+i\epsilon}\left[-g^{\mu\nu}+\left(1-\frac{1}{\lambda}\right)\frac{k^\mu k^\nu}{k^2+i\epsilon}\right], \tag{1.9}$$

$$S^{ij}_{\beta\alpha}(k) = i\frac{\delta_{ij}}{k^2-m^2+i\epsilon}\left[\not{k}+m\right]_{\beta\alpha}, \tag{1.10}$$

$$G_{ba}(k) = i\frac{\delta_{ba}}{k^2+i\epsilon.} \tag{1.11}$$

The QCD vertices are,

$$(i) \;:\; -ig\,[t_c]\,i^j\,[\gamma_\mu]_{\beta\alpha} \tag{1.12}$$

$$(ii) \;:\; gC_{abc}k'_a \tag{1.13}$$

$$(iii) \;:\; -gC_{a_1a_2a_4}\left[g^{\nu_1\nu_2}(p_1-p_2)^{\nu_3}+g^{\nu_2\nu_3}(p_2-p_3)^{\nu_1}+g^{\nu_3\nu_1}(p_3-p_1)^{\nu_2}\right] \tag{1.14}$$

$$\begin{aligned}(iv) \;:\; & -ig^2\left[C_{ea_1a_2}C_{ea_3a_4}\left(g^{\nu_1\nu_3}g^{\nu_2\nu_4}-g^{\nu_1\nu_4}g^{\nu_2\nu_3}\right)\right.\\ & +C_{ea_1a_3}C_{ea_4a_2}\left(g^{\nu_1\nu_4}g^{\nu_3\nu_2}-g^{\nu_1\nu_2}g^{\nu_3\nu_4}\right)\\ & \left.+\,C_{ea_1a_4}C_{ea_2a_3}\left(g^{\nu_1\nu_2}g^{\nu_4\nu_3}-g^{\nu_1\nu_3}g^{\nu_4\nu_2}\right)\right]\end{aligned} \tag{1.15}$$

Using these rules one can calculate the invariant matrix element $\mathcal{M}$, which represents the non-trivial part of the scattering matrix[7] and expresses the dynamics of the interactions that come into play.

---

[7] For an interacting quantum field theory, the scattering matrix relates asymptotic incoming and outgoing states $\Psi(\alpha)$, described by the set of quantum numbers α, through the relation $S_{\beta\alpha} \equiv \langle\Psi_{\rm out}(\beta)|\Psi_{\rm in}(\alpha)\rangle$. In terms of the invariant matrix element $\mathcal{M}$, the scattering matrix can be written as $S_{\beta\alpha} = \delta_{\beta\alpha} + iT_{\beta\alpha}$ with $iT = (2\pi)^4\delta^{(4)}\left(\sum_i p_i - \sum_f p_f\right) i\mathcal{M}$.

The cross section is then built up by convolving the dynamics with the kinematics. For a process $p_1 p_2 \to k_1 \dots k_n$, the cross section is,

$$d\sigma = \frac{1}{F}|\mathcal{M}|^2 d\Phi_n, \tag{1.16}$$

where F is the incoming particle flux and $d\Phi_n$ is the n-particle final state phase space. Since the scattering matrix cannot be calculated analytically in QCD, one resorts to perturbation theory. The scattering matrix takes the form

$$S = \mathbf{1} + \alpha_s C + \alpha_s^2 C^2 + \dots, \tag{1.17}$$

where α_s is the strong coupling constant $\alpha_s \equiv g^2/4\pi$ and the factors C incorporate the Feynman diagram calculations. If α_s is small, it is sufficient to retain only the first few terms to approximate the complete solution. As a consequence of vacuum polarization, α_s is not fixed, but it evolves with energy. This evolution is governed by the *renormalization group equation*, which reads

$$\beta\left(g(\mu)\right) \equiv \mu \frac{dg(\mu)}{d\mu} = -g\left[\frac{\alpha_s}{4\pi}\beta_1 + \left(\frac{\alpha_s}{4\pi}\right)^2 \beta_2 + \dots\right] \approx -g\frac{\alpha_s}{4\pi}\left(11 - \frac{2N_f}{3}\right), \tag{1.18}$$

where β_i are the i-loop contributions to the beta function, μ is an energy scale, N_f is the number of flavours and the last approximation refers to the 1-loop calculation. Solving for α_s one obtains

$$\alpha_s(\mu^2) = \frac{\alpha_s(\mu_0^2)}{1 + \frac{\alpha_s(\mu_0^2)}{4\pi}\left(11 - \frac{2N_f}{3}\right)\ln\frac{\mu^2}{\mu_0^2}}. \tag{1.19}$$

From (1.19) we can see that α_s grows with decreasing energy. As shown in Fig. 1.3, α_s is large for energies of the order of the proton mass. Therefore, at values of α_s close to the hadronization scale (~ 1 GeV), perturbation theory cannot be trusted. In practice, the coefficients C can be ill-behaved, e.g. they can contain large logarithms.

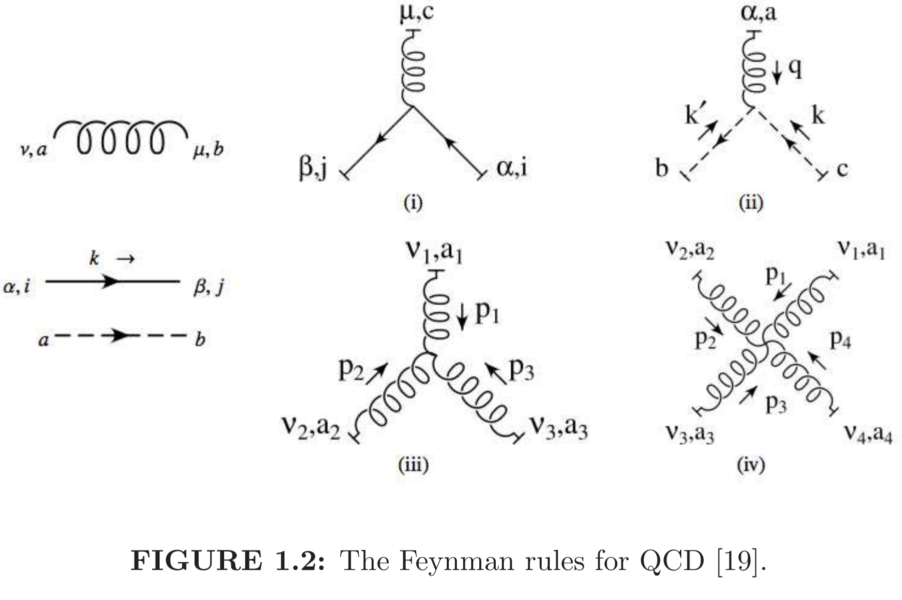

FIGURE 1.2: The Feynman rules for QCD [19].

1.2.2 From partons to hadrons

In the previous sections, the theory was set-up using quarks and gluons as the fundamental degrees of freedom. However, except for the top quark, experimentally one sees only colourless degrees of

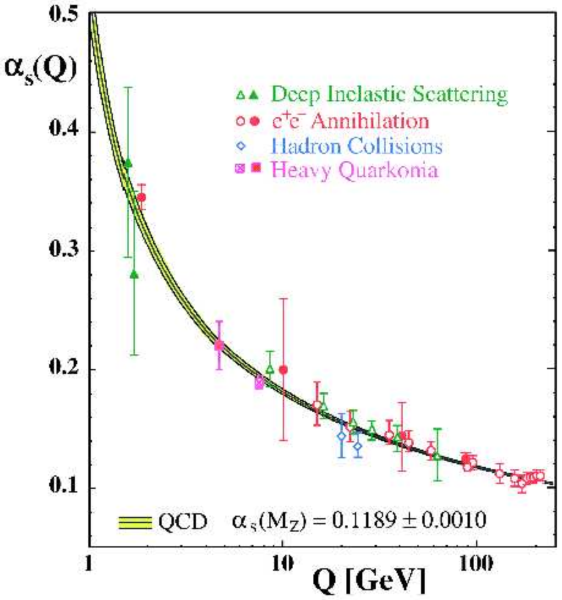

FIGURE 1.3: The QCD running coupling [20].

freedom, i.e. hadrons. Here we explain how we can use the parton level calculations to extract results for hadron observables.

It was first proposed by Feynman [21], that lepton-hadron scattering in the limit of large momentum transfer can be explained by the *parton model*, where the hadron is replaced by fundamental point-like constituents[8]. As it was further elaborated by Bjorken and Paschos [22], the essential ingredient of the parton model is to consider a class of infinite momentum frames, in which a parton i will carry a fraction $0 < x_i < 1$ of the hadron's momentum. Lepton-hadron scattering can then be described by an incoherent sum[9] of all the possible lepton-parton scatterings. This idea was reversed by Drell and Yan [23] in the study of what is today known as the Drell-Yan process (i.e. lepton hadroproduction). It was there postulated that the hadronic cross section $\sigma(H_1 H_2 \to \mu^+\mu^- + X)$ could be obtained by convolving the cross section for hard-scattering subprocess $\hat{\sigma}(q\bar{q} \to \mu^+\mu^-)$ with the *Parton Distribution Functions* f_{i/H_1}

$$\sigma_{H_1 H_2} = \sum_{i,j} \int dx_1 dx_2 f_{i/H_1}(x_1) f_{j/H_2}(x_2) \hat{\sigma}(ij \to \mu^+\mu^-). \tag{1.20}$$

The PDFs $f_{i/H}(x)$ express the probability of finding a parton i inside the hadron H, carrying a momentum fraction x. The domain of validity of (1.20) is the asymptotic scaling limit: $s = Q^2 \to \infty, x$ fixed. It was later discovered in SLAC and PETRA experiments that the cross sections in hadron scattering do not scale according to (1.20), but instead display a logarithmic dependence on the annihilation energy. The appearance of these logarithms was attributed to the emission of gluons that were collinear to the incoming beam and it was shown that such contributions could be factored into the the PDFs, with (1.20) becoming

$$\sigma_{H_1 H_2} = \sum_{i,j} \int dx_1 dx_2 f_{i/H_1}(x_1, Q^2) f_{j/H_2}(x_2, Q^2) \hat{\sigma}(ij \to \mu^+\mu^-), \tag{1.21}$$

where Q is a momentum scale which characterizes the hard subprocess. Eq (1.21) is an example of theorems called *factorization theorems* [24] which essentially express the fact that in certain kinematic regimes the non-perturbative dynamics can be separated from the perturbative dynamics. Let us see how one obtains (1.21).

---

[8] These were later identified with the QCD quarks and gluons.

[9] Incoherent sum is a sum which does not include interference terms.

The DGLAP equations

A complete derivation of how the scaling violations are obtained from QCD goes outside the scope of this thesis. Here we sketch the most important points in the proof and for further details we refer the reader to QCD textbooks such as [25]. One of the fundamental ideas of QFT is the fact that there are no bare fields (or point-like particles). Everything is instead surrounded by a cloud of fermion-antifermion pairs and gauge bosons. The naïve parton model, in which exact scaling holds, is based on the assumption that partons are point-like objects. In this case the electromagnetic structure function reads

$$F_2(x) = \sum_q e_q^2 x f_q(x). \tag{1.22}$$

Scaling violations arise naturally when one abandons the concept of point-like partons and adopts the correct field-theoretic concept of "dressed" particles. The first step in this way is to consider the NLO correction to (1.20) or in more physical terms, consider that the quarks participating in the interactions can *branch*, i.e. emit a gluon (Fig. 1.4). If in the no-branching case we have n particles in the final state, after the branching the final state consists of $(n+1)$ particles. The cross section then reads [25]

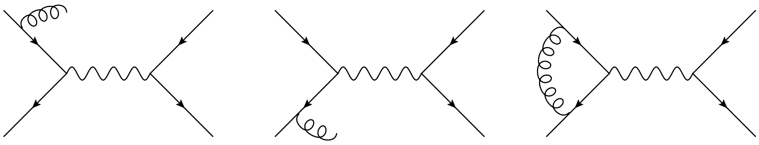

FIGURE 1.4: NLO corrections to $q\bar{q} \to l^+l^-$.

$$d\sigma_{n+1} = d\sigma_n \frac{\alpha_s}{2\pi} \hat{P}_{ij}(z) \frac{dt}{t} dz, \tag{1.23}$$

where z is the fraction of energy carried away by the gluon, t is the virtuality of the quark propagator and $\hat{P}_{ij}$ is the *unregularized splitting function* that describes the probability of the $i \to j$ parton splitting. In the case of massless $q \to q$ branching, it reads

$$\hat{P}_{qq}(z) = C_F \frac{1+z^2}{1-z}, \tag{1.24}$$

where $C_F = 4/3$ is the colour factor associated to the corresponding Feynman diagram. From (1.23),(1.24), we observe that the cross section has two types of singularities, in the limit $t \to 0$ and $z \to 1$. The latter is called an *infrared singularity* and corresponds to the emission of a very soft quark. The former gives a *collinear singularity* and corresponds to the limit in which the gluon is emitted parallel to one of the quarks[10]. The infrared singularity in (1.24) is compensated by the virtual corrections at $z = 1$ and introducing the "plus distribution"

$$f(x)_+ = f(x) - \delta(1-x) \int_0^1 dx' f(x'), \tag{1.25}$$

one can write the *regularized splitting function* as the sum of the real and virtual contributions

$$P_{qq}(z) = C_F \left[\frac{1+z^2}{(1-z)_+} + \frac{3}{2}\delta(1-z) \right]. \tag{1.26}$$

---

[10] As we will see later in this chapter, in the limit of small-angle emission we have $t = E_i E_j \theta_j^2$ and thus the limit $t \to 0$ with $E_i, E_j \neq 0$ corresponds to $\theta_j \to 0$.

With these contributions (1.22) becomes

$$F_2(x,Q^2) = x\sum_q e_q^2 \int_x^1 \frac{d\xi}{\xi} f_q(\xi) \left[\delta\left(1-\frac{x}{\xi}\right) + \frac{\alpha_s}{2\pi} P_{qq}\left(\frac{x}{\xi}\right) \ln\frac{Q^2}{\kappa^2} + C\left(\frac{x}{\xi}\right)\right], \tag{1.27}$$

where the logarithm comes from the t integration with a cutoff κ and C is a calculable function which contains a finite contribution. The collinear singularity, which introduces the logarithmic Q^2 dependence in the structure function corresponds to the long-range limit, where we know that α_s is big and perturbation theory is no longer valid. This singularity can be absorbed at a *factorization scale* μ_F in a definition of a *renormalized PDF*

$$f_q(x,\mu_F^2) = f_q(x) + \frac{\alpha_s}{2\pi} \int_x^1 \frac{d\xi}{\xi} f_q(\xi) \left[P\left(\frac{x}{\xi}\right) \ln\frac{\mu_F^2}{\kappa^2} + C\left(\frac{x}{\xi}\right)\right]. \tag{1.28}$$

In terms of the renormalized PDF, the structure function (1.27) becomes

$$F_2(x,Q^2) = x\sum_q e_q^2 \int_x^1 \frac{d\xi}{\xi} f_q(\xi,\mu_F^2) \left[\delta\left(1-\frac{x}{\xi}\right) + \frac{\alpha_s}{2\pi} P_{qq}\left(\frac{x}{\xi}\right) \ln\frac{Q^2}{\mu_F^2}\right]. \tag{1.29}$$

The structure function being an observable, it cannot depend on non-physical scales such as μ_F. Thus we should have

$$\frac{\partial F_2(x,Q^2)}{\partial \ln \mu_F^2} = 0, \tag{1.30}$$

which leads to[11] the evolution equation

$$t\frac{\partial}{\partial t} f_q(x,t) = \frac{\alpha_s}{2\pi} \int_x^1 \frac{d\xi}{\xi} P_{qq}\left(\frac{x}{\xi}\right) f_q(\xi,t). \tag{1.31}$$

More generally, considering all possible types of quark-gluon splittings, we arrive at the Dokshitzer-Gribov-Lipatov-Altarelli-Parisi equations [26–29]

$$t\frac{\partial}{\partial t} \begin{pmatrix} f_{q_i}(x,t) \\ f_g(x,t) \end{pmatrix} = \frac{\alpha_s}{2\pi} \sum_j \int_x^1 \frac{d\xi}{\xi} \begin{pmatrix} P_{q_iq_j}\left(\frac{x}{\xi},\alpha_s(t)\right) & P_{q_ig}\left(\frac{x}{\xi},\alpha_s(t)\right) \\ P_{gq_j}\left(\frac{x}{\xi},\alpha_s(t)\right) & P_{gg}\left(\frac{x}{\xi},\alpha_s(t)\right) \end{pmatrix} \begin{pmatrix} f_{q_j}(x,t) \\ f_g(x,t) \end{pmatrix}. \tag{1.32}$$

We note that although the DGLAP equations determine the evolution of the PDFs with the energy transfer, the x-dependence can only be determined by data using (1.22). We further note that the splitting functions have a perturbative expansion in α_s

$$P_{q_iq_j(z,\alpha_s)} = \delta_{ij} P_{qq}^{(0)}(z) + \frac{\alpha_s}{2\pi} P_{q_iq_j}^{(1)}(z) + \ldots. \tag{1.33}$$

In the derivations above we used the leading order expressions for the splitting functions[12]. The DGLAP equations are the analogue of the beta function for the QCD running coupling (Eq. 1.18).

1.3 Going beyond the LO approximation

In the previous section we saw that it is necessary to go beyond the Leading Order in perturbation theory in order to explain the scaling violations. We also saw that in order to deal with divergences within perturbation theory, we need to introduce non-physical scales (cf. Eq. 1.18,1.29). If one retains all the orders of the perturbative expansion these scale dependencies will cancel out, since physical observables cannot depend on non-physical scales. However, truncating the perturbative expansion at a certain order introduces a dependence on these scales. Let us see what happens if we make a LO expansion. Consider a dimensionless physical observable $\mathcal{O}$. We have seen that in order to avoid divergences associated to higher-order effects, one needs to introduce an arbitrary scale μ in the perturbative expansion. Then $\mathcal{O}$ will acquire a dependence on Q^2/μ^2, where Q is a large energy scale and the renormalized coupling $\alpha_s(\mu^2)$. The perturbative expansion of $\mathcal{O}$ reads

---

[11] We defined $t \equiv \mu_F^2$.

[12] Today the splitting functions are the only quantity calculated with N^{3}LO precision in QCD.

$$\mathcal{O}\left(\frac{Q^2}{\mu^2}=1,\alpha_s(Q^2)\right)=\mathcal{O}_1\alpha_s(Q^2)+\mathcal{O}_2\alpha_s^2(Q^2)+\dots. \tag{1.34}$$

From (1.19) we have

$$\alpha_s(Q^2)=\alpha_s(\mu^2)-b_1\ln\frac{Q^2}{\mu^2}\alpha_s^2(\mu^2)+\dots, \tag{1.35}$$

where $b_1=\frac{1}{4\pi}\left(11-\frac{2N_f}{3}\right)$. Thus (1.34) becomes

$$\mathcal{O}\left(1,\alpha_s(Q^2)\right)=\mathcal{O}_1\alpha_s(\mu^2)+\left(\mathcal{O}_2-\mathcal{O}_1b_1\ln\frac{Q^2}{\mu^2}\right)\alpha_s^2(\mu^2)+\dots. \tag{1.36}$$

We see thus that the LO expansion $\mathcal{O}\left(1,\alpha_s(Q^2)\right)=\mathcal{O}_1\alpha_s(\mu^2)$ gives no information on the absolute normalization, since $\alpha_s(\mu)$ can take any value by changing the value of μ. Beginning at NLO, the μ dependence of $\ln\frac{Q^2}{\mu^2}$ starts to compensate the μ dependence of α_s and thus we can obtain information about the absolute normalization and also lessen the scale dependence of $\mathcal{O}$. Moreover NLO can open up new channels that are inaccessible at LO and can lead to non-trivial distributions for observables that are trivial at LO. The aim of this section is to explain the technical problems that one faces when performing a NLO calculation, and their solutions.

1.3.1 NLO corrections and associated divergences

At Next-to-Leading Order, the differential cross section (1.21) becomes

$$d\sigma_{ij\to X}^{NLO}=\sum_{i,j}\int dx_1dx_2f_{i/p}(x_1,\mu_F)f_{j/p}(x_2,\mu_F)d\hat{\sigma}_{ij\to X}^{NLO}(x_1,x_2,\mu_R), \tag{1.37}$$

where $d\hat{\sigma}_{ij\to X}^{NLO}$ contains the α_s correction to the Leading Order result. One can symbolically write

$$\hat{\sigma}^{NLO}=\int_n d\hat{\sigma}^B+\int_{n+1}d\hat{\sigma}^R+\int_n d\hat{\sigma}^V, \tag{1.38}$$

with $d\hat{\sigma}^B, d\hat{\sigma}^R, d\hat{\sigma}^V$ representing the LO (Born), real and virtual contributions respectively and the integration subscripts represent the size of the final state phase space. The corresponding Feynman diagrams are shown in Fig. 1.5. The general nomenclature is that N^{k}LO contributions correspond to adding k gluons to the LO contribution. From (1.37) one sees that in a NLO calculation one should use a NLO calculation for the running coupling and match with NLO PDFs. It is evident from Fig. 1.5 that the virtual diagrams are physically indistinguishable from the Born ones and thus the corresponding contribution to the cross section will be given by the interference of the two terms

$$d\hat{\sigma}^V=d\Phi_n\sum 2\mathrm{Re}\left(\mathcal{M}_1^V\mathcal{M}_0^*\right), \tag{1.39}$$

where the sum runs over all possible 1-loop contributions and the subscripts 1 and 0 refer to the NLO and LO matrix elements respectively. The corresponding contributions from the real emissions read

$$d\hat{\sigma}^R=d\Phi_{n+1}\sum\left|\mathcal{M}_1^R\right|^2. \tag{1.40}$$

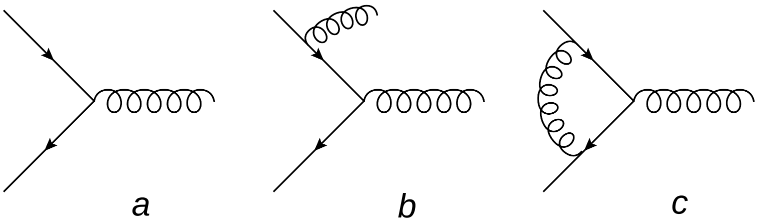

FIGURE 1.5: Example of Born (a), Real (b) and Virtual (c) Feynman diagrams.

The NLO contributions involve three types of divergences: *ultraviolet divergences* from the $k \to \infty$ limit of the loop integrals in the virtual contributions, *infrared divergences* from the $k \to 0$ limit of loop diagrams and the emission of soft gluons in the real contributions and *collinear divergences* coming from real emission diagrams which involve branchings between three massless partons. These divergences are not physical but signal the breakdown of perturbation theory. It has been formally established by the Bloch-Nordsieck and Kinoshita-Lee-Nauenberg theorems [30–32], that sufficiently inclusive quantities are finite in the massless limit. Ultraviolet divergences are regularized and absorbed in the running of the coupling constant. Infrared divergences cancel exactly between the real, collinear and virtual contributions in the final state[13]. Collinear singularities in the initial state do not cancel after summing the different contributions and have thus to be absorbed in the PDFs by virtue of the factorization theorem, as we have seen in the previous section. Since these kind of singularities are particularly important for the studies performed in this thesis, we provide more details in the following section.

1.3.2 The Parton Shower approach

We saw in the previous section that collinear singularities arise in massless-parton branchings. In order to study their origin in perturbation theory, let us start by calculating a concrete example $\gamma^* \to q\bar{q}g$ (Fig. 1.6). The real emission matrix element reads

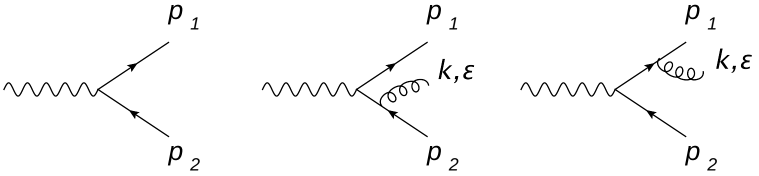

FIGURE 1.6: Born and real emission contributions to $\gamma^* \to q\bar{q}g$.

$$\mathcal{M}_{q\bar{q}g} = \bar{u}(p_1) ig\not{\epsilon} t^a \frac{i}{\not{p}_1 + \not{k}} ie\gamma_\mu v(p_2) - \bar{u}(p_1) ie\gamma_\mu \frac{i}{\not{p}_2 + \not{k}} ig\not{\epsilon} t^a v(p_2), \tag{1.41}$$

where we have assumed $m_q = m_{\bar{q}} = 0$. In the soft limit $k \ll p_1, p_2$ we can ignore terms suppressed by powers of k and using the equations of motion, (1.41) becomes

$$\mathcal{M}_{q\bar{q}g} = \bar{u}(p_1) ie\gamma_\mu t^a v(p_2) g \left(\frac{p_1 \cdot \epsilon}{p_1 \cdot k} - \frac{p_2 \cdot \epsilon}{p_2 \cdot k} \right). \tag{1.42}$$

---

[13] For technical details see e.g. [25].

Upon squaring we obtain

$$\begin{aligned} |\mathcal{M}_{q\bar{q}g}|^2 &= |\mathcal{M}_{q\bar{q}}|^2 C_F g^2 \frac{2p_1 \cdot p_2}{(p_1 \cdot k)(p_2 \cdot k)} \\ &= |\mathcal{M}_{q\bar{q}}|^2 C_F g^2 \frac{2E_1 E_2 (1-\cos\theta_{p_1 p_2})}{E_1 E_g (1-\cos\theta_{p_1 g}) E_2 E_g (1-\cos\theta_{p_2 g})}, \end{aligned} \tag{1.43}$$

with $\mathcal{M}_{q\bar{q}} = -\bar{u}(p_1) ie\gamma_\mu v(p_2)$. We see that the matrix element diverges in the limit of soft gluon emission $E_g \to 0$ and for collinear emission $\theta_{p_i g} \to 0$. Introducing the energy fractions[14] $x_i \equiv 2E_i/\sqrt{s}$ the squared invariant amplitude becomes proportional to $[(1-x_1)(1-x_2)]^{-1}$, which diverges in the limits $x_3 = x_g = 0$ with x_1/x_2 fixed (soft singularity) and in the limit $x_{1(2)} \to 1$ with $x_{2(1)}$ fixed (collinear singularity). The region that is close to the boundary of the phase space is called the *Sudakov region* (Fig. 1.7). This region is where logarithms from soft and collinear emission become large and the cross section becomes divergent.

Let us now generalize a step further and consider a general branching $a \to bc$ in the final or initial state, as shown in Fig. 1.8. Defining t as the virtuality of the propagator in the branching, we can easily see that[15] $t \equiv p_b^2 = -2p_a \cdot p_c < 0$ in initial state branching and $t \equiv p_a^2 = 2p_b \cdot p_c > 0$ in final-state branching. Hence initial-state branching is usually referred to as *spacelike branching* and final-state branching as *timelike branching*. Defining $z \equiv \frac{E_b}{E_a}$ and noting that $\theta = \theta_a + \theta_b$, in the small-angle limit we have

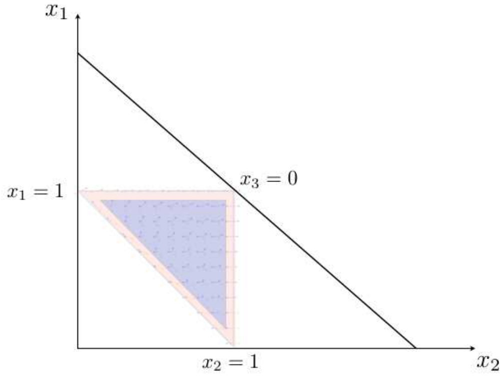

FIGURE 1.7: The gluon emission phase-space in terms of the energy fractions x_i. The Sudakov region is shown in red.

$$t = \begin{cases} z(1-z)E_a^2\theta^2 & \text{for timelike branching} \\ E_a E_b \theta_c^2 & \text{for spacelike branching} \end{cases} \tag{1.44}$$

Considering the phase space for gluon emission at fixed p_b, we have

$$\begin{aligned} d\Phi_{n+1}^{\mathrm{FSB}} &= \ldots \frac{d^3\mathbf{p}_b}{(2\pi)^3 2E_b} \frac{d^3\mathbf{p}_c}{(2\pi)^3 2E_c} \\ &= \ldots \frac{d^3\mathbf{p}_a}{(2\pi)^3 2E_a} \frac{E_a}{E_c} \frac{d^3\mathbf{p}_b}{(2\pi)^3 2E_b} \\ &= d\Phi_n \frac{1}{2(2\pi)^3} \int E_b dE_b \theta_b d\theta_b d\phi dt \frac{dz}{1-z} \delta(t - E_b E_c \theta^2) \delta\left(z - \frac{E_b}{E_a}\right) \\ &= d\Phi_n \frac{1}{4(2\pi)^3} dt dz d\phi, \end{aligned} \tag{1.45}$$

---

[14] One can confirm that $\sum_i x_i = 2$ and $0 < x_i < 1$.

[15] All partons are considered massless throughout this section.

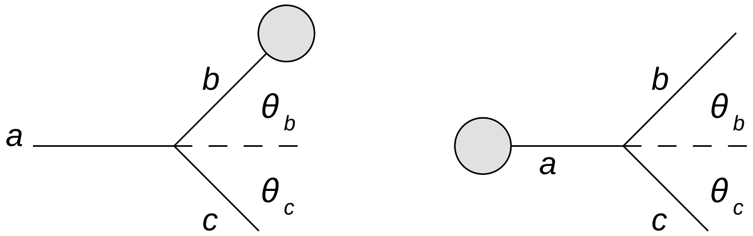

FIGURE 1.8: Spacelike (initial state) and timelike (final state) parton branching. The blob represents the $\mathcal{M}_n$ contribution.

where FSB stands for final-state branching and we used the relations $t = 2E_bE_c(1-\cos\theta) = z(1-z)E_a^2\theta^2$ and $\theta = \theta_b/(1-z)$ that follow from energy and momentum conservation in the collinear limit. For initial-state branching the corresponding relation reads

$$d\Phi_{n+1}^{\text{ISB}} = d\Phi_n \frac{1}{4(2\pi)^3} dt \frac{dz}{z} d\phi. \tag{1.46}$$

Remembering that

$$d\sigma_n = \frac{1}{F}|\mathcal{M}|^2 d\Phi_n, \tag{1.47}$$

and integrating over the azimuthal angle, we find (1.23) for both initial and final-state branching

$$d\sigma_{n+1} = d\sigma_n \frac{dt}{t} dz \frac{d\phi}{2\pi}\frac{\alpha_s}{2\pi}\hat{P}_{ba}(z). \tag{1.48}$$

The variable t is called the *ordering* or *evolution variable* and it can be defined in multiple ways, e.g. for final-state branching

virtuality	$t \equiv z(1-z)E^2\theta^2$
p_T^2	$t \equiv z^2(1-z)^2E^2\theta^2$
angle	$t \equiv E^2\theta^2$

Coherence and angular ordering

It has been shown [33] that in order to correctly take into account *coherence* effects, the correct evolution variable should be a function of the emission angle[16]. In order to see how colour coherence leads to angular ordering, we study gluon emission from a fully coloured object as shown in Fig. 1.9. The matrix element for this process reeds

$$\mathcal{M} = g^2\left(t^at^b\right)_{ij}\left[\frac{Q\cdot\epsilon}{Q\cdot k} - \frac{\bar{p}\cdot\epsilon}{\bar{p}\cdot k}\right] + g^2\left(t^bt^a\right)_{ij}\left[\frac{p\cdot\epsilon}{p\cdot k} - \frac{Q\cdot\epsilon}{Q\cdot k}\right], \tag{1.49}$$

where Q is the virtuality of the intermediate propagator and the sequence of the terms corresponds to the sequence of the colour flows drawn in Fig. 1.9. The squared invariant amplitude summed over all colours will be proportional to

$$\sum_{a,b,i,j}\left|\left(t^at^b\right)_{ij}\right|^2 = \sum_{a,b}\text{Tr}\left[t^at^bt^bt^a\right] = \frac{N_c^2-1}{2}C_F, \tag{1.50}$$

---

[16] See also [34] and references therein.

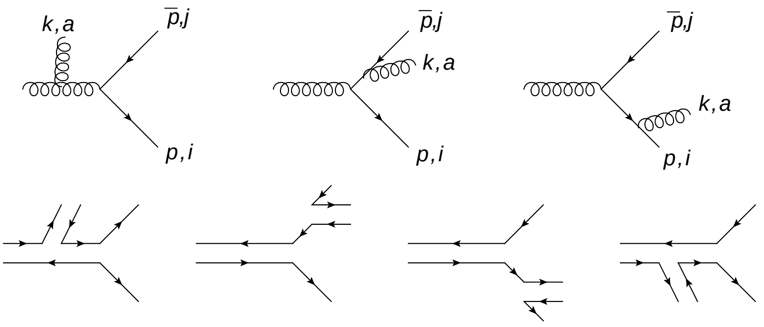

FIGURE 1.9: Gluon emission from a fully coloured system with its associated colour flows.

while the interference term will be proportional to

$$\sum_{a,b,i,j}\left(t^at^b\right)_{ij}\left(t^bt^a\right)^*_{ij}=\sum_{a,b}\mathrm{Tr}\left[t^at^bt^at^b\right]=\frac{N_c^2-1}{2}\left(C_F-\frac{C_A}{2}\right) \tag{1.51}$$

and with $C_F=\frac{N_c^2-1}{2N_c}$ and $C_A=N_c$, one can see that the interference effects are suppressed by $1/N_c^2$. Equivalently one says that to leading order in $1/N_c^2$ the emission of soft gluons can be described as a sum of incoherent emissions. This is particularly important for the Monte Carlo implementation of the parton shower algorithms which is formulated as a Markov process. In order to see how the *angular ordering* arises formally we recall (eq. 1.43) that the matrix element for gluon emission is proportional to the function

$$W_{p_1p_2}=\frac{1-\cos\theta_{p_1p_2}}{(1-\cos\theta_{p_1g})\,(1-\cos\theta_{p_2g})}. \tag{1.52}$$

This can be rewritten as

$$\begin{aligned} W_{p_1p_2} &= W^{[p_1]}_{p_1p_2}+W^{[p_2]}_{p_1p_2}=\frac{1}{2}\left(W_{p_1p_2}+\frac{1}{1-\cos\theta_{p_1g}}-\frac{1}{1-\cos\theta_{p_2g}}\right) \\ &+ \frac{1}{2}\left(W_{p_1p_2}\frac{1}{1-\cos\theta_{p_2g}}-\frac{1}{1-\cos\theta_{p_1g}}\right). \end{aligned} \tag{1.53}$$

Now one can prove [25] that

$$\int_0^{2\pi}\frac{d\phi_{p_1g}}{2\pi}W^{[p_1]}_{p_1p_2}=\begin{cases}\frac{1}{1-\cos\theta_{p_1g}} & \text{if } \theta_{p_1g}<\theta_{p_1p_1}\\ 0 & \text{otherwise}\end{cases} \tag{1.54}$$

We thus see that the angle for successive emissions will keep getting smaller and smaller. Radiation is forced to be inside the two cones that are centered at the parent partons with an aperture twice the opening angle of the emitting partons. In this way gluon radiation gets self-collimated and jet structure arises naturally.

The Sudakov form factor

From (1.48) we see that the probability for a single emission integrated over all azimuthal angles is given by

$$dP_1(t,t+dt)=\frac{\alpha_s(t)}{2\pi}\frac{dt}{t}\int\hat{P}_{ij}(z)dz, \tag{1.55}$$

where $\hat{P}_{ij}$ is the regularized splitting function. The probability of no-emission then reads

$$dP_0(t, t+dt) = 1 - \frac{\alpha_s(t)}{2\pi}\frac{dt}{t}\int \hat{P}_{ij}(z)dz. \tag{1.56}$$

We note that unitarity enforces that the probabilities for resolvable and non-resolvable emission add up to 1. In turn non-resolvable emissions contain soft and collinear emissions as well as virtual corrections, as shown in Fig. 1.10. We conclude thus that the '1' of eq. (1.56) contains all the virtual contributions at the collinear limit.

With the above ingredients, we can calculate the probability of no emission taking place between the scales t_1 and t_2

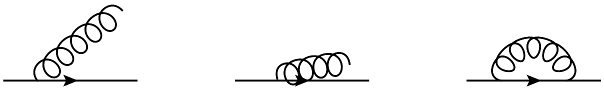

FIGURE 1.10: Resolvable (left) and non-resolvable (center and right) emissions.

$$\begin{aligned} P_0(t_1, t_2) &= \sum_j \lim_{N\to\infty}\prod_{n=1}^{N}\left[1 - \frac{dt}{t_n}\frac{\alpha_s(t_n)}{2\pi}\int dz\hat{P}_{ij}(z)\right] \\ &= \exp\left\{-\sum_j \int_{t_1}^{t_2}\frac{dt}{t}\frac{\alpha_s(t)}{2\pi}\int dz\hat{P}_{ij}(z)\right\} \\ &\equiv \Delta(t_1, t_2), \end{aligned} \tag{1.57}$$

where $\Delta(t_1, t_2)$ is called the *Sudakov form factor* and expresses the probability of evolving from t_1 to t_2 without any resolvable branching. This obeys the evolution equation

$$t\frac{\partial}{\partial t}\left(\frac{f}{\Delta}\right) = \frac{1}{\Delta}\int \frac{dz}{z}\frac{\alpha_s}{2\pi}\hat{P}(z) f\left(\frac{x}{z}, t\right), \tag{1.58}$$

which is nothing other but the DGLAP equation (1.32) with the substitutions $f \to f/\Delta$ and $P(z) \to \hat{P}(z)$. Integrating (1.58) and expanding the solution we obtain

$$\begin{aligned} f(x,t) &= \Delta(t) f(x, t_0) + \int_{t_0}^{t}\frac{dt'}{t'}\frac{\Delta(t)}{\Delta(t')}\int\frac{dz}{z}\frac{\alpha_s}{2\pi}\hat{P}(z) f\left(\frac{x}{z}, t'\right) \\ &= \Delta(t) f(x, t_0) + \int_{t_0}^{t}\frac{dt'}{t'}\frac{\Delta(t)}{\Delta(t')}\int\frac{dz}{z}\frac{\alpha_s}{2\pi}\hat{P}(z) \\ &\times \left[\Delta(t') f\left(\frac{x}{z}, t_0\right) + \int_{t_0}^{t'}\frac{dt''}{t''}\frac{\Delta(t')}{\Delta(t'')}\int\frac{dz}{z}\frac{\alpha_s}{2\pi}\hat{P}(z) f\left(\frac{x}{zz'}, t''\right)\right] + \ldots \end{aligned} \tag{1.59}$$

which is an exponential expansion containing terms of order $\left(\frac{\alpha_s}{2\pi}\ln\frac{t}{t_0}\right)^n$. We thus say that the parton shower resums the leading collinear logarithms in all orders of perturbation theory. We stress out that the above equations were derived in the limit of small-angle gluon emission. As a consequence, although the Sudakov region is correctly described by the parton shower, hard emissions will not be correctly described and one would have to resort to an exact matrix element calculation for these.

1.3.3 Jets and Jet Algorithms

As it has been shown in the previous section, the parton shower evolution induces sequential parton branchings which are forced to self-collimate with the parent partons. After hadronization, this will produce a collimated bunch of hadrons, which is called a jet. The different ways in which one can define a jet are known as jet algorithms and they have to obey to a minimal set of rules[17].

Jet algorithms can be classified into two broad categories: *cone algorithms* and *sequential recombination algorithms*. Cone algorithms use conical structures to cluster particles within a certain angular distance, such that the sum of the clustered particle momenta coincides with the cone axis. Sequential recombination algorithms start by identifying the closest particles in some distance measure, recombine them and iterate the procedure until a stopping criterion is reached. Here we will only describe a certain class of sequential recombination algorithms that are used for the studies reported here.

A very important property that a jet algorithm must satisfy is the *Infrared and Collinear* (IRC) *Safety*, which states that the set of hard events in an event should be insensitive to a collinear splitting or a soft emission. As we have already seen, collinear and soft gluons lead to divergences in perturbation theory, whose cancellation depends on the correct summation of the real and virtual contributions of the corresponding process. The situation might change in the case of IRC unsafe algorithms as illustrated in Fig. 1.11: IRC unsafe algorithms can lead to different classes of events for real and virtual contributions, thus spoiling the cancellation of their divergences. The use of IRC safe algorithms also leads to a reduced sensitivity to hadronization effects.

The Cambridge/Aachen, k_t and anti-k_t algorithms are based on the generalized distance measures [36]

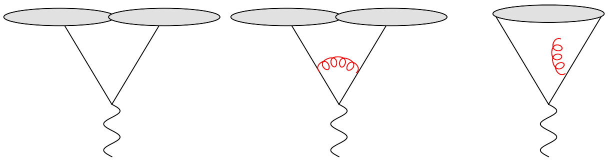

FIGURE 1.11: Illustration of IRC unsafety. The addition of a soft gluon changes the number of hard jets, spoiling the cancellation between real and virtual contributions.

$$\begin{aligned} d_{ij} &= \min\left(k_{ti}^{2p}, k_{tj}^{2p}\right)\frac{\Delta R_{ij}^2}{R^2} \\ d_{iB} &= k_{ti}^{2p} \\ \Delta R_{ij}^2 &= (y_i - y_j)^2 + (\phi_i - \phi_j)^2, \end{aligned} \tag{1.60}$$

where k_{t_i}, y_i, ϕ_i are the transverse momentum, rapidity and azimuth of particle i, d_{ij} and d_{iB} are the distances between the entities i and j and the distance between entity i and the beam respectively. The parameter p takes the values

$$p = \begin{cases} 1 & k_t \\ 0 & \text{Cambridge/Aachen} \\ -1 & \text{anti-}k_t \end{cases} \tag{1.61}$$

The clustering algorithm starts by identifying the smallest of the distances d_{ij}, d_{iB} and recombining i and j if d_{ij} is the smallest distance or defining i as a jet and removing it from the list of entities if d_{iB} is the smallest distance. This procedure is iterated until no entities are left. It is evident that soft and collinear emissions will be clustered right at the beginning of the clustering procedure and thus the anti-k_t is an IRC safe algorithm (as is the case for sequential recombination algorithms). It has been shown [36] that the choice $p = -1$ favors clustering around hard particles, as opposed to the k_t algorithm which favors soft-particle clustering or the Cambridge/Aachen algorithm which favors energy-independent clusterings. As a result anti-k_t gives circular hard jets (as opposed to irregularly shaped jets obtained with k_t and Cambridge/Aachen - cf. Fig. 1.12) which is an appealing property for experimental jet reconstruction.

---

[17] See [35] and references therein.

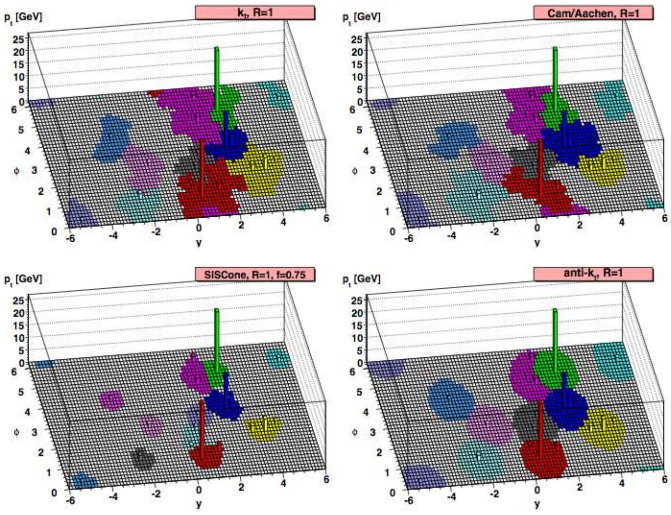

FIGURE 1.12: Parton-level jets with soft “ghosts” reconstructed with different jet algorithms [36].

1.3.4 Matching ME and PS calculations

From the previous discussion it should be clear that there are two different approaches for the calculation of observables in hadron collisions: the matrix element approach which relies on perturbative QCD and is thus a fixed order approach and the parton shower approach which includes all-order contributions in the collinear limit. The two approaches are complementary in the sense that in the Sudakov region, where the parton shower approach is valid, the matrix-element calculation breaks down due to the appearance of large logarithms, while in the hard-emission region, where the matrix-element calculation provides a good description, the approximations involved in the parton shower approach become invalid. A naïve combination of these two methods would result in a *double counting* of certain configurations, e.g. a $(N+1)$-jet event can be obtained both from a hard, large-angle emission off a N-jet event and from a soft or collinear emission from a $(N+1)$-jet event. There have been several studies on how to combine these two approaches, which led to the so-called matrix element with parton shower matching or merging schemes. These are divided into two categories according to whether the matrix element calculation is performed with LO or NLO accuracy, with the corresponding approaches collectively referred to as MEPS and NLOPS respectively[18].

Tree level: MEPS

There are three schemes for merging matrix-element calculations with parton showers: CKKW [39], CKKW-L [40] and MLM[19]. The fundamental concept of these merging schemes is the partitioning of the phase space into two regions with the use of a transition scale y_{ini} defined by a given jet measure y. If y_{cut} is the resolution variable of a given jet algorithm, then for $y_{\text{cut}} > y_{\text{ini}}$ the observables are taken from matrix elements modified by Sudakov form factors, while for $y_{\text{cut}} < y_{\text{ini}}$ the observables are taken from the parton showers subjected to a veto procedure. In more detail, the different merging schemes follow the same basic procedure

1. definition of a jet measure y and calculation of the cross sections for the processes $pp \to X + n$−jets with $n = 0, 1, \ldots, n_{\max}$

---

[18] We note that there is intensive ongoing work in merging the MEPS and NLOPS approaches, thus allowing a description of events with multiple hard jets at NLO accuracy. This approach has been dubbed MENLOPS [37,38].

[19] See e.g. [41].

2. generation of hard partons with a probability proportional to the total cross section and a kinematic configuration given by the matrix element

3. acceptance or rejection of the configuration with a probability that includes Sudakov and running coupling effects

4. parton showering with a 'veto' that rejects events with extra jets

The differences between the merging schemes lie in

- the definition of the jet measure

- the way the acceptance/rejection of step (2) above is carried out

- the initial conditions for the parton shower algorithms and the application of the 'veto'

The MLM approach is the simplest of the three since it doesn't involve an analytic computation of the Sudakov form factors. The MLM matching proceeds as follows

1. generation of parton level configurations for a given jet multiplicity n with $p_T > p_T^{\min}$, $\Delta R_{ij} > \Delta R_{ij}^{\min}$, $|\eta| < \eta_{\max}$ and with a weight given by

$$P(n) = \frac{\sigma_{X+n}}{\sum_{i=0}^{n_{\max}} \sigma_{X+i}}$$

2. a configuration is chosen according to the relative size of the cross section and clustered according to the k_t algorithm, in order to find the scales at which two partons merge into one. A branching history (consistent with the colour flow) is thus constructed as shown in Fig. 1.13.

3. the coupling constant is reweighted by the factor $\frac{\alpha_s(d_i^2)}{\alpha_s(Q_0^2)}$ at each node i, with Q_0 the hard scattering scale

4. the event is passed to the parton shower, which is run without a veto

5. a jet algorithm is used to cluster the showered event using the clustering parameters $E_T^{clus}, R_{clus}, \eta_{clus}$. Usually the clustering parameters are looser than the generation parameters to insure full coverage of the phase space.

6. starting from the hardest parton, jets with the smallest ΔR are selected and if $\Delta R < 1.5 R_{clus}$ the parton is matched to the jet and removed from the sample. If all jets are matched to partons the event is matched. Unmatched events are rejected.

7. if no extra jets are present, event is matched. Extra jets are retained only for highest multiplicity inclusive sample and iff their E_T is smaller than the E_T of the softest matched jet

8. the cross section is multiplied by the ratio of events accepted by the matching procedure over the total number of events . This reproduces the Sudakov reweighting of the CKKW scheme.

For the study of a final state containing $X + n_{\max}-$jets, one generates the $X + n_i-$jets samples with $i < n_{\max}$ in exclusive mode and the highest multiplicity sample in inclusive mode, combining all samples according to their relative weights.

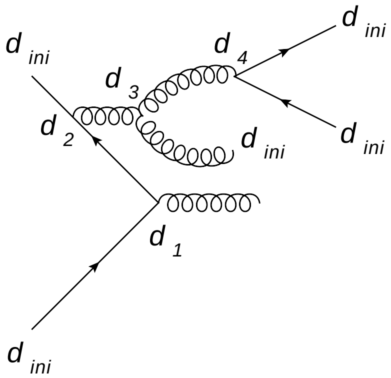

FIGURE 1.13: Example of branching history in the MLM procedure. The nodal values of the k_t measure satisfy $d_{\text{ini}} < d_4 < d_3 < d_2 < d_1$, where d_1 corresponds to the hard scattering scale.

Beyond the tree level: NLOPS

The MEPS approach is based on LO matrix elements and thus it is bound to suffer from large uncertainties associated to the scale variations as well as being unreliable for the estimation of total event rates. The question thus arises if one can use NLO instead of LO matrix elements. This problem had been solved until recently only for the case of the first (hardest) emission by the MC@NLO [42] and POWHEG [43,44] methods. In both of these methods, the first emission is taken from NLO matrix element (with the shower approximation subtracted so as to avoid the collinear and soft singularities) and the following emissions are taken from the parton shower and are thus only reliable in the collinear limit.
Using (1.38), an observable at NLO accuracy is given by the quantity[20]

$$\langle\mathcal{O}\rangle = \int \mathcal{O} d\sigma = \int d\Phi_n \mathcal{O}(\Phi_n)\left[B(\Phi_n) + V_b(\Phi_n)\right] + \int d\Phi_n d\Phi_r \mathcal{O}(\Phi_n,\Phi_r) R(\Phi_n,\Phi_r), \tag{1.62}$$

where $d\Phi_r$ is the 1-particle emission phase-space and B, V_b, R are the Born, virtual and real contributions respectively[21] (which incorporate their associated divergences). As we have seen the integrals over the real and virtual contributions are separately divergent and their divergences cancel out only after summing the two contributions after the integration. Thus this problem is not suitably formulated for numerical integration. In order to perform Monte Carlo calculations, the divergences have to be dealt with separately. This is done, e.g. using a *subtraction method*[22]

$$\begin{aligned}
\langle\mathcal{O}\rangle &= \int d\Phi_n \mathcal{O}(\Phi_n)\left[B(\Phi_n) + V_b(\Phi_n) + \int d\Phi_r C(\Phi_n,\Phi_r)\right] \\
&+ \int d\Phi_n d\Phi_r \left[\mathcal{O}(\Phi_n,\Phi_r) R(\Phi_n,\Phi_r) - \mathcal{O}(\Phi_n) C(\Phi_n,\Phi_r)\right] \\
&\equiv \int d\Phi_n \mathcal{O}(\Phi_n)\left[B(\Phi_n) + V(\Phi_n)\right] \\
&+ \int d\Phi_n d\Phi_r \left[\mathcal{O}(\Phi_n,\Phi_r) R(\Phi_n,\Phi_r) - \mathcal{O}(\Phi_n) C(\Phi_n,\Phi_r)\right],
\end{aligned} \tag{1.63}$$

where C is a suitably chosen function (called a *counterterm*) that cancels the singularities of the divergent contributions. In the last equation we have singled out the finite part of the virtual contribution.

---

[20] In the rest we omit the hat from $\hat{\sigma}$, knowing that the rest of the chapter refers to parton-level results.

[21] We define $B \equiv \mathcal{L}\mathcal{B}, R \equiv \mathcal{L}\mathcal{R}, V \equiv \mathcal{L}\mathcal{V}$, where $\mathcal{B}, \mathcal{R}, \mathcal{V}$ are the matrix elements and $\mathcal{L}$ is the parton luminosity.

[22] Another solution is given by the so-called *phase-space slicing method*, which separates the divergent part of the phase space from the non-divergent one. This approach is no longer being used by the current MC generators and will thus not be treated here.

All the integrals in (1.63) are now finite[23]. Introducing the quantity

$$\bar{B}(\Phi_n) = B(\Phi_n) + V(\Phi_n) + \int d\Phi_r \left[R(\Phi_n, \Phi_r) - C(\Phi_n, \Phi_r)\right], \tag{1.64}$$

(1.63) can be written as

$$\langle \mathcal{O} \rangle_{NLO} = \int d\Phi_n \bar{B}(\Phi_n) \mathcal{O}(\Phi_n) + \int d\Phi_n d\Phi_r R(\Phi_n, \Phi_r) \left[\mathcal{O}(\Phi_n, \Phi_r) - \mathcal{O}(\Phi_n)\right], \tag{1.65}$$

where the subscript NLO denotes that the observable is being calculated by the matrix element with NLO accuracy. Calculating the same observable from the parton shower, one would have to compute the probability of having a single emission up to a scale t plus the probability of having no further emissions down to the cutoff scale t_0. Using the Sudakov form factors to express the no-emission probability, the one-emission cross section is given by[24] (cf. eq. 1.38, 1.48)

$$d\sigma = B(\Phi_n) d\Phi_n \Delta_{t_0} + R^s d\Phi_n d\Phi_r \Delta_t = B(\Phi_n) d\Phi_n \Delta_{t_0} + B(\Phi_n) \frac{\alpha_s}{2\pi} \frac{dt}{t} P(z) dz \frac{d\phi}{2\pi} \Delta_t, \tag{1.66}$$

where R^s denotes the real contribution in the soft and collinear limit and

$$\Delta_{t_i} = \exp\left[-\int_{t_i} \frac{dt}{t} \int dz \frac{\alpha_s(t)}{2\pi} P(z)\right] = \exp\left[-\int_{t_i} \frac{R^s}{B} d\Phi_r\right]. \tag{1.67}$$

We have thus

$$\langle \mathcal{O} \rangle = \int d\Phi_n B(\Phi_n) \left[\mathcal{O}(\Phi_n) \Delta_{t_0} + \int_{t_0} \frac{dt}{t} dz \frac{d\phi}{2\pi} \mathcal{O}(\Phi_n, \Phi_r) \Delta_t \frac{\alpha_s}{2\pi} P(z)\right]. \tag{1.68}$$

Expanding to first order in α_s, we get the parton shower result

$$\langle \mathcal{O} \rangle_{PS} = \int d\Phi_n B(\Phi_n) \left\{\mathcal{O}(\Phi_n) + \int_{t_0} \frac{dt}{t} dz \frac{d\phi}{2\pi} \left[\mathcal{O}(\Phi_n, \Phi_r) - \mathcal{O}(\Phi_n)\right] \frac{\alpha_s}{2\pi} P(z)\right\}. \tag{1.69}$$

We observe that (1.69) and (1.65) differ by the substitutions $B(\Phi_n) \longleftrightarrow \bar{B}(\Phi_n)$ and $R(\Phi_n, \Phi_r) \longleftrightarrow B(\Phi_n) \frac{1}{t} \frac{\alpha_s}{2\pi} P(z)$. Substituting these expressions into (1.68) we get the all-orders emission probability

$$\begin{aligned} \langle \mathcal{O} \rangle_{NLOPS} &= \int d\Phi_n \bar{B}(\Phi_n) \left\{\mathcal{O}(\Phi_n) \Delta_{t_0} + \int d\Phi_r \mathcal{O}(\Phi_n, \Phi_r) \Delta_t \frac{R(\Phi_n, \Phi_r)}{B(\Phi_n)}\right\} \\ &+ \int d\Phi_{n+1} \mathcal{O}(\Phi_{n+1}) \left[R(\Phi_{n+1}) - R^s(\Phi_{n+1})\right], \end{aligned} \tag{1.70}$$

with

$$\Delta_t = \exp\left[-\int d\Phi'_r \frac{R(\Phi_n, \Phi'_r)}{B(\Phi_n)} \theta(t' - t)\right]. \tag{1.71}$$

The last term in (1.70) is the so-called *matrix element correction*, which provides the hard, large-angle contribution to the first emission calculated from the NLO matrix element.

Some comments are in order with respect to the specific implementation of the NLOPS formalism in the POWHEG and MC@NLO approaches. The first term of (1.70) $\bar{B}(\Phi_n) d\Phi_B$ is what is called a $\mathbb{S}$ event (for Standard MC evolution) and the last term $[R(\Phi_{n+1}) - R^s(\Phi_{n+1})] d\Phi_{n+1}$ is called a $\mathbb{H}$ event (for Hard MC evolution). In MC@NLO the difference $R(\Phi_{n+1}) - R^s(\Phi_{n+1})$ can become negative, thus leading to the appearance of negative events. In POWHEG on the other hand, one has a freedom to choose a parametrization $R^s(\Phi_{n+1}) = R(\Phi_{n+1})F(\Phi_{n+1})$ with $0 \leq F(\Phi_{n+1}) \leq 1$ and $F(\Phi_{n+1}) \to 1$ in the soft and collinear limit. Thus $R(\Phi_{n+1}) - R^s(\Phi_{n+1}) = R(\Phi_{n+1})[1 - F(\Phi_{n+1})] \geq 0$. Another difference with MC@NLO is that the part within the curly braces in (1.70), which corresponds to the first emission, is generated within POWHEG and is thus independent of the showering generator. Finally, we note that although the two approaches are equivalent at NLO, differences may arise at NNLO. In order to see how these differences arise, one can calculate an observable computed with MC@NLO at the high-p_T region[25]

---

[23] This holds only if the underlying Born contribution is finite. For the case of divergent Born contributions, see [45].

[24] We note that the expressions that follow give a rather schematic proof of concept for the NLOPS formalism. For rigorous mathematical proofs we refer to the original publications [42–44].

$$\begin{aligned}
\langle\mathcal{O}\rangle &= \int d\Phi_n \bar{B}_{HW}(\Phi_n)\left[\mathcal{O}(\Phi_n)\Delta_{HW}(p_T^{\min}) + \int d\Phi_r \mathcal{O}(\Phi_n,\Phi_r)\Delta_{HW}(p_T)\frac{R_{HW}(\Phi_n,\Phi_r)}{B(\Phi_n)}\right] \\
&+ \int d\Phi_{n+1}\mathcal{O}(\Phi_{n+1})\left[R(\Phi_{n+1}) - R(\Phi_{n+1})\right] \\
&\approx \int d\Phi_{n+1}\mathcal{O}(\Phi_{n+1})\left\{R(\Phi_{n+1}) + \left[\frac{\bar{B}(\Phi_n)}{B(\Phi_n)} - 1\right]R_{HW}(\Phi_{n+1})\right\} \qquad (1.72)
\end{aligned}$$

where we used the fact that $\Delta_{HW}(p_T^{\min}) = 0$ and $\Delta_{HW}(p_T) = 1$ for $p_T^{\min} \to 0$ and $p_T \to \infty$. The last term in (1.72) is of order $\mathcal{O}(\alpha_s R)$ (and thus NNLO with respect to the underlying Born), so the differences between POWHEG and MC@NLO should be small. However, for certain processes the NNLO corrections can be quite big and then the difference of the two approaches is manifest in some observables. A characteristic case is e.g. the dip in the central rapidity region of the hardest jet in $t\bar{t}$ events produced with MC@NLO [41]. The dip in MC@NLO grows with increasing p_T^{jet}, while the POWHEG spectrum displays no dip. This behavior is inherited to MC@NLO from HERWIG[26]. On the other hand POWHEG produces the first emission itself, filling-in the dead zone of HERWIG.

1.4 Monte Carlo Generators

As we saw in the above discussion a critical point for the calculation of observables in hadron collisions is the computation of the cross section. For a process $1\ 2 \to N$ this involves a multidimensional integration over the final-state phase space. These integrals are almost always impossible to compute analytically and one has to resort to numerical methods. One of the most popular methods is the Monte Carlo technique. The Monte Carlo technique is based on the approximation of an integral as follows

$$I = \int_{x_1}^{x_2} f(x)dx = (x_2 - x_1)\langle f(x)\rangle \approx (x_2 - x_1)\frac{1}{N}\sum_{i=1}^{N} f(x_i). \qquad (1.73)$$

For the cross section one would get in a similar way

$$\sigma = \int_0^1 dx\frac{d\sigma}{dx} \approx \frac{1}{N}\sum_{i=1}^{N}\left.\frac{d\sigma}{dx}\right|_i, \qquad (1.74)$$

where x is an arbitrary parametrization of the phase space chosen so that the boundaries lie at $x = 0, 1$. The differential cross section $\left.\frac{d\sigma}{dx}\right|_i$ is called the *weight* of the event parametrized by x_i. After calculating the cross section for a process, one wants to go one step further and simulate physical events as they occur in nature, i.e. generate a set of 4-momenta distributed according to the dynamical laws governing the process under study. This step in the HEP language is called *event generation.* In a mathematical language the event generation amounts to choosing a value $x \in [x_{\min}, x_{\max}]$ distributed according to $f(x)$ or equivalently to selecting uniformly (x, y) in $x_{\min} < x < x_{\max}$, $0 < y < f(x)$. In the case where the primitive F of f is known, the problem can be solved analytically by noting that

---

[25] The subscript HW indicates quantities calculated from the HERWIG parton shower.

[26] Since HERWIG uses an angular ordered shower, hard radiation which is produced after the first emission is suppressed. This gives rise to a "dead cone" where there is no emission at all from the parton shower.

$$\int_{x_{\min}}^{x} f(x')dx' = R\int_{x_{\min}}^{x_{\max}} f(x')dx'. \tag{1.75}$$

Then

$$x = F^{-1}\left[F(x_{\min}) + RA_{tot}\right], \tag{1.76}$$

where $A_{tot} = \int_{x_{\min}}^{x_{\max}} f(x)dx$. In most of the cases, F is unknown and the problem is tackled using the *hit-and-miss* technique. The hit-and-miss algorithms proceeds as follows

1. generate two random numbers R, R' uniformly[27] distributed in $(0, 1)$
2. calculate $x = x_{\min} + R(x_{\max} - x_{\min})$ and $y = R' f_{\max}$
3. if $y < f(x)$ accept the event (hit), else go to (1)

One can write

$$I = \frac{\int_{x_{\min}}^{x_{\max}} f(x)dx}{f_{\max}(x_{\max} - x_{\min})}\Omega = \frac{N_{hit}}{N_{try}}\Omega, \tag{1.77}$$

where $\Omega = f_{\max}(x_{\max} - x_{\min})$ and N_{hit}, N_{try} is the number of hits and number of total tries respectively. Then the integral of a function can be computed with the hit-and-miss technique:

$$\int_{x_{\min}}^{x_{\max}} f(x)dx = f_{\max}(x_{\max} - x_{\min})\frac{N_{hit}}{N_{try}}. \tag{1.78}$$

Thus the probability of a hit is proportional to $f/f_{\max}$. Performing the hit-and-miss technique on a sample of events generated with a uniform sampling over the phase space (*weighted events*) gives a final sample of events which occur with the same probability as in nature (*unweighted events*). The probability for an event to be accepted by the hit-and-miss technique is $\frac{(d\sigma/dx)_i}{(d\sigma/dx)_{\max}}$ while the unweighting efficiency is given by $\frac{(d\sigma/dx)_{ave}}{(d\sigma/dx)_{\max}}$.

This procedure has been automated by codes that are collectively called Monte Carlo Generators. These are separated into two categories: *cross-section integrators*, which calculate cross sections for specific processes, and *event generators*, which generate weighted and unweighted events and can thus be used for simulating physical processes. This simulation is a multistep process (Fig. 1.14) starting with the matrix element calculation and continuing through the parton shower, hadronization, clustering, simulation of the underlying event and multiple parton interactions etc.

1.5 Parameter inputs for MC11 production in ATLAS with aMC@NLO

Here we give a brief overview of some of the input values of physical parameters that are critical for MC production with aMC@NLO and in particular in the studies mentioned in this report.

- The PDFs are given by the CT10 set [87], which includes 52 uncertainty eigenvector sets. The PDF related uncertainties are given by the formulae [47]

$$\Delta\sigma_{PDF+} = \sqrt{\sum_i \left(\max\left[\sigma(\text{set}_{+i}) - \sigma(\text{set}_0), \sigma(\text{set}_{-i}) - \sigma_{\text{set}_0}, 0)\right]\right)^2} \tag{1.79}$$

$$\Delta\sigma_{PDF-} = \sqrt{\sum_i \left(\max\left[\sigma(\text{set}_0) - \sigma(\text{set}_{+i}), \sigma_{\text{set}_0} - \sigma(\text{set}_{-i}), 0)\right]\right)^2} \tag{1.80}$$

---

[27] Many recent integration algorithms do not use uniform sampling.

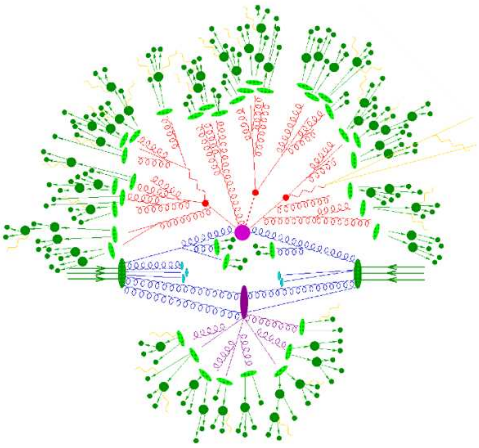

FIGURE 1.14: Typical structure of a hadron collision event with different steps in the event generation chain.

For completeness we note here that the uncertainties related to the variation of the factorization and renormalization scales are given by

$$\Delta\sigma_{\mu+} = \max_{\{\xi_F,\xi_R\}} [\sigma(\xi_F,\xi_R) - \sigma(1,1)] \tag{1.81}$$

$$\Delta\sigma_{\mu-} = -\min_{\{\xi_F,\xi_R\}} [\sigma(\xi_F,\xi_R) - \sigma(1,1)] \,, \tag{1.82}$$

where $\xi = \mu/\mu_0$. One usually varies independently ξ_R and ξ_F in the region $0.5 \leq \xi \leq 2$.

- The bottom-quark mass is set equal to the value used for the extraction of the CT10 PDF set ($m_b = 4.75$ GeV) for consistency. We note that the definition of the b-quark mass (and the choice of a particular value for it) is a long-standing problem in perturbative QFT. Perturbative calculations including the production of b quarks should be accompanied with an uncertainty related to the variation of the b mass. A conservative choice which covers the range of b masses that seem to reproduce the experimental data is $4.5 < m_b[\text{GeV}] < 5$.
- The top mass value was set to $m_t = 172.5$ GeV [48]
- The masses of the rest of the Standard Model particles and the elements of the CKM matrix are taken from the 2010 PDG values [49]
- Particular care must be taken in choosing the values for the electroweak gauge-boson masses, the mixing angle θ_W and the Fermi constant G_F. These are not independent of one another and choosing arbitrary values can lead to a violation of gauge invariance and consequently unitarity. For consistency with the rest of the MC11 production samples we choose G_F, m_W, m_Z as input parameters set to their 2010 PDG values and calculate the mixing angle and the electroweak coupling constant from the tree-level electroweak relations

$$\sin^2\theta_W = 1 - \frac{m_W^2}{m_Z^2} \tag{1.83}$$

$$\alpha(m_Z) = \frac{\sqrt{2} m_W^2 \left(1 - \frac{m_W^2}{m_Z^2}\right) G_F}{\pi} \tag{1.84}$$

Chapter 2

THE ATLAS EXPERIMENT

2.1 The LHC

The Large Hadron Collider [50] is a synchrotron accelerator designed to accelerate protons up to a centre-of-mass energy of $\sqrt{s} = 14$ TeV and lead ions (Pb^{82+}) up to a center-of-mass energy of $\sqrt{s_{NN}} = 2.76$ TeV per nucleon pair. Some interesting design characteristics of the LHC are presented in Table 2.1. The LHC is located underground at a depth ranging from 45 to 170 meters. After a startup period with the LHC working at $\sqrt{s} = 900$ GeV, from the beginning of 2010 the LHC has been operating at $\sqrt{s} = 7$ TeV, delivering a total integrated luminosity of 5.61 fb^{-1} at Interaction Point 1, where the ATLAS detector [51] is located (Fig. 2.1).

TABLE 2.1: LHC design characteristics

Parameter	Value
Circumference	26.7 km
Proton Energy per Beam	7 TeV
Lorentz γ factor	7461
Particles per bunch	$1.15 \cdot 10^{11}$
Bunches per beam	2808
Peak Luminosity	10^{34} cm^{-1}s^{-1}
Field of main bends	8.33 T
Revolution frequency	11.245 kHz
Collision rate	40 MHz
Stored Energy per beam	362 MJ
Bunch crossing interval	25 ns

Before entering the LHC, the protons are accelerated to 450 GeV and grouped into bunches circulating with the LHC frequency. This is achieved by the accelerator complex that precedes the LHC as illustrated in Fig. 2.2. Protons are extracted from Hydrogen gas, by applying an electric field. The protons are then accelerated by LINAC2 up to 50 MeV. The beam is then injected into the Proton Booster reaching an energy of 1.4 GeV. In the next step the beam is transferred to the Proton Synchrotron, where it is accelerated to 26 GeV and circulated with the same frequency and bunch spacing as the LHC. The final step before entering the LHC is the Super Proton Synchrotron, which accelerates the beams to 450 GeV. Once the beams are inside the LHC accelerator, it takes

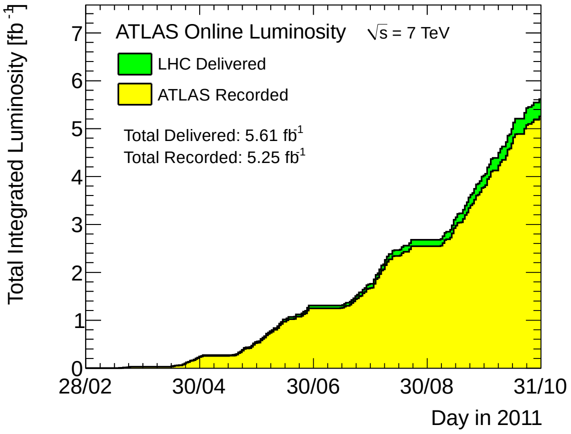

FIGURE 2.1: Total integrated luminosity delivered at Interaction Point 1 and recorded by the ATLAS detector in the 2011 proton runs [52].

approximately 20 minutes for them to be accelerated to the peak energy. The average beam lifetime is around a day, after which, it is dumped into a block of a 8-meter long cylinder of graphite.

2.2 The ATLAS detector

At design luminosity 23 interactions per beam-crossing are expected with an event rate of 40 MHz (the minimum between bunch train crossings being 25 ns). The guiding principle in the construction of the ATLAS experiment was the maximization of the discovery potential for new physics, notably the search for the Higgs boson. The study of such kind of events requires (a) a hermetic coverage in pseudorapidity and azimuthal angle for the accurate determination of $\not{E}_T$ and jet energy directions, (b) electromagnetic and hadronic calorimeters with adequate energy resolution for measurements of EM and hadronic objects and (c) muon spectrometers with a capacity for high-precision muon measurements.

The overall detector layout is shown in Fig. 2.3. ATLAS is a general purpose detector and is composed of 4 major parts: (i) the inner detector, (ii) the calorimeter system, (iii) the muon spectrometers and (iv) the magnets. The Inner Detector (depicted in Fig. 2.4) measuring 6.2 m in length and 2.1 m in diameter is comprised of 3 subdetectors: (a) the pixel detector, (b) the Semiconductor Tracker (SCT) and (c) the Transition Radiation Tracker (TRT). It is immersed in a solenoidal magnetic field with intensity $B = 2$ T and has a pseudorapidity coverage of $|\eta| < 2.5$. With the use of very high-granularity detectors close to the interaction point, the Inner Detector is used for the determination of impact parameters, particle momentum and vertexing. The Pixel Detector is designed for identifying short-lived particles, such as B hadrons. The TRT provides tracking to enhance pattern recognition and using the transition radiation characteristics of electrons, provide the electron identification.

The calorimeter system (shown in Fig. 2.5) is comprised of 3 parts: (a) the electromagnetic calorimeter, (b) the hadronic calorimeter and (c) the Forward calorimeters. The electromagnetic and hadronic calorimeters are divided into two regions: (i) barrel, covering the pseudorapidity range and $|\eta| \leq 1.475$ (ECal) and $|\eta| \leq 1.7$ (HCal) and (ii) end-cap, covering the pseudorapidity range $1.375 \leq |\eta| \leq 3.2$ (ECal) and $1.5 \leq |\eta| \leq 3.2$ (HCal). The forward calorimeter covers the region $3.1 < |\eta| < 4.9$. The electromagnetic (barrel and end-cap), forward and hadronic end-cap Calorimeters use Liquid Argon for the active medium and lead (ECal), copper (HCal and FCal) or tungsten (FCal) for the absorbers. The hadronic barrel Calorimeter uses plastic scintillating tiles embedded in an iron absorber. The calorimeter system measures the energy of electromagnetic and hadronic objects, providing an en-

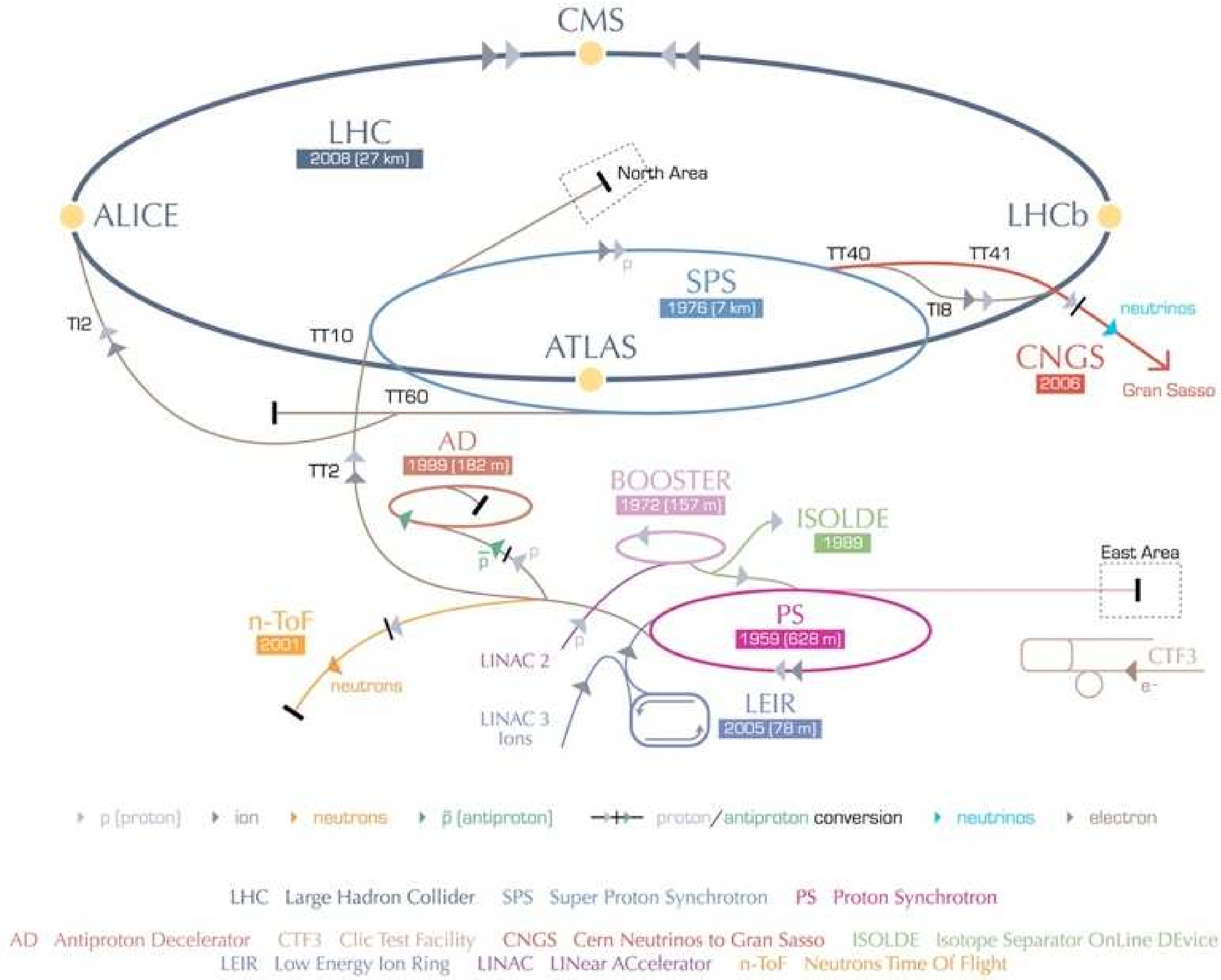
CMS
LHC
2008 (27 km)
North Area
ALICE
LHCb
TT40
TT41
SPS
1976 (7 km)
TI8
neutrinos
TI2
TT10
ATLAS
CNGS
2006
Gran Sasso
TT60
AD
1999 (182 m)
TT2
BOOSTER
1972 (157 m)
ISOLDE
1989
p̄
p
East Area
n-ToF
2001
PS
1959 (628 m)
CTF3
e-
neutrons
LINAC 2
LINAC 3
Ions
LEIR
2005 (78 m)
p (proton)
ion
neutrons
p̄ (antiproton)
proton/antiproton conversion
neutrinos
electron
LHC Large Hadron Collider
SPS Super Proton Synchrotron
PS Proton Synchrotron
AD Antiproton Decelerator
CTF3 Clic Test Facility
CNGS Cern Neutrinos to Gran Sasso
ISOLDE Isotope Separator OnLine DEvice
LEIR Low Energy Ion Ring
LINAC LINear ACcelerator
n-ToF Neutrons Time Of Flight

FIGURE 2.2: The CERN accelerator complex.

ergy resolution parametrized by $\frac{\sigma(E)}{E} = \frac{a}{\sqrt{E[\mathrm{GeV}]}} \oplus b$, where a is a stochastic term and b is a constant term reflecting local non-uniformities in the response of the calorimeter. In the barrel region, one has $a = (10.1 \pm 0.4)\%\sqrt{\mathrm{GeV}}$ and $b = (0.2 \pm 0.1)\%$ for electromagnetic objects in the ECal. The energy resolution for hadronic objects in the HCal is around $80\%\sqrt{\mathrm{GeV}}$, with a constant term of zero within the associated uncertainties.

The calorimeter system is surrounded by the muon spectrometer. The muon spectrometer consists of muon chambers utilizing different detector technologies to measure muons and a toroidal magnet system producing a magnetic field of approximately 0.5 T and 1 T in the barrel and end-cap regions respectively. The muon spectrometer is designed to trigger on muons within the range $|\eta| < 2.4$ with dedicated subdetectors and measure the muons' momenta in the range $|\eta| < 2.7$.

2.3 Trigger

With the expected interaction rate reaching approximately 1 GHz at design luminosity and the current hardware and storage limitations only allowing a storage rate of approximately 100 Hz, the task of the Trigger/DAQ system of the ATLAS detector is required to achieve rejection factors of the order of 10^7, while maintaining an excellent efficiency in recording rare processes. The trigger consists of three

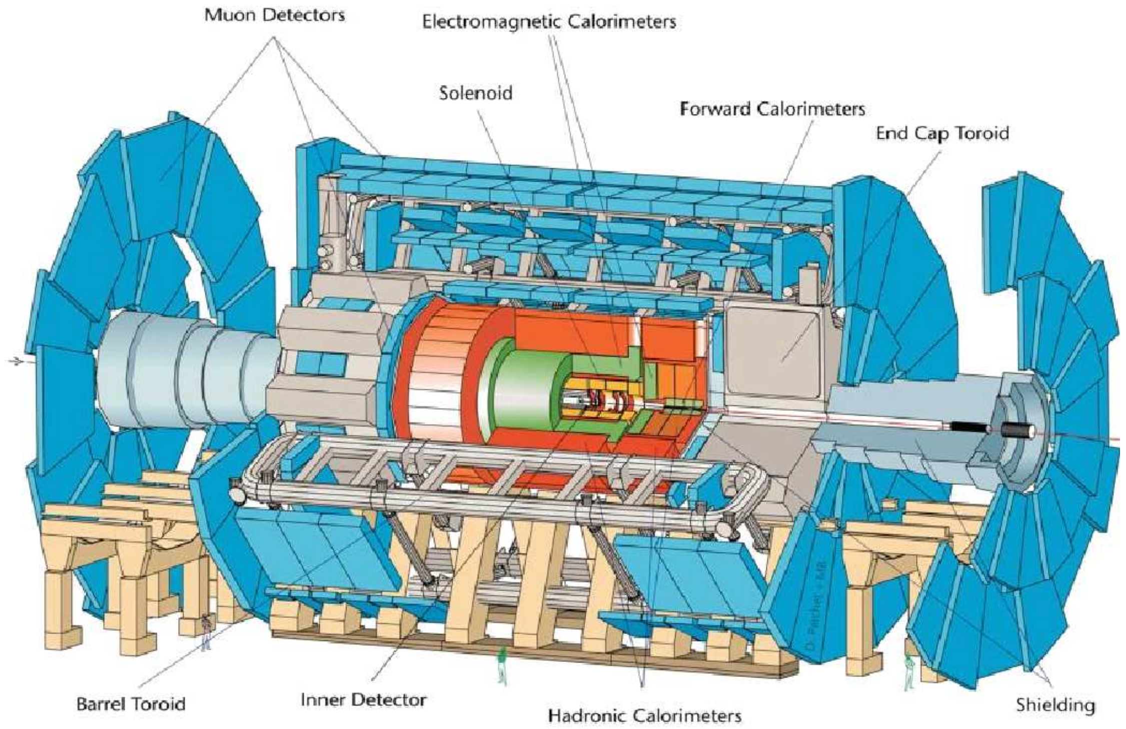

FIGURE 2.3: Layout of the ATLAS detector.

levels of event selection: the Level-1 (L1), Level-2 (L2) and the Event Filter (EF). The L1 trigger is exclusively hardware based while the High-Level Trigger (L2 and EF) are software based.
The L1 trigger uses all the calorimeter subsystems and the Resistive Plate Chambers (RPC) and Thin-Gap Chambers (TGC) of the muon system to search for high-p_T muons, electrons, photons, jets and hadronically decaying τ leptons. The L1 trigger reduces the accepted events rate to 75 kHz. The time taken from the bunch crossing until the L1 trigger decision is made is required to be less than 2.5 μs. The L2 trigger is seeded by Regions-of-Interest (ROI), based on coordinates, energy, and type of signatures identified by the L1 trigger. The accept rate is reduced by L2 to below 3.5 kHz with an average processing time of 40 ms per event. The EF then further reduces the accept rate to approximately 200 Hz with an average processing time of 4 s per event.

2.4 Coordinate system

The coordinate system used by the ATLAS experiment is defined with respect to the LHC beam and the plane of the accelerator. The beam direction defines the z-axis and the $x-y$ plane is the plane transverse to the beam direction. The positive x-axis points from the interaction point towards the center of the LHC ring and the positive y-axis points upwards. The azimuthal angle ϕ is measured around the beam axis and the polar angle θ is measured from the beam axis[1].

---

[1] One most frequently uses the pseudorapidity variable, defined as $\eta = -\ln(\tan\theta/2)$. Transverse variables are defined in terms of their x and y components, e.g. for the transverse momentum we have $p_T = \sqrt{p_x^2 + p_y^2}$. One can also define a distance measure in (η, ϕ) space as $\Delta R = \sqrt{(\Delta\eta)^2 + (\Delta\phi)^2}$.

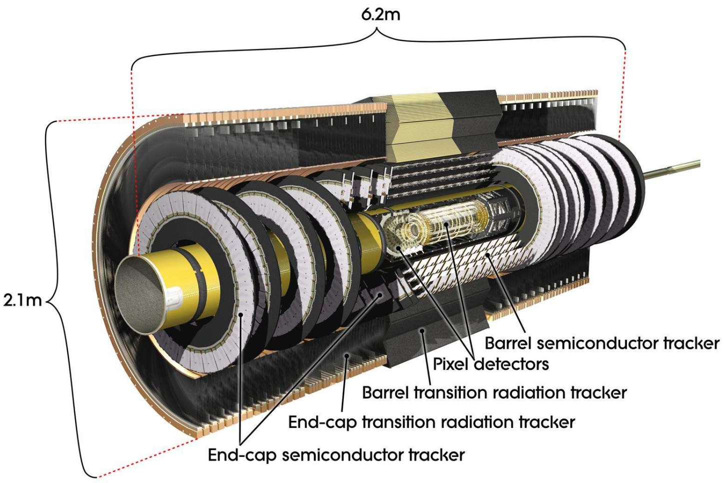
6.2m
2.1m
Barrel semiconductor tracker
Pixel detectors
Barrel transition radiation tracker
End-cap transition radiation tracker
End-cap semiconductor tracker

FIGURE 2.4: Layout of the Inner Detector.

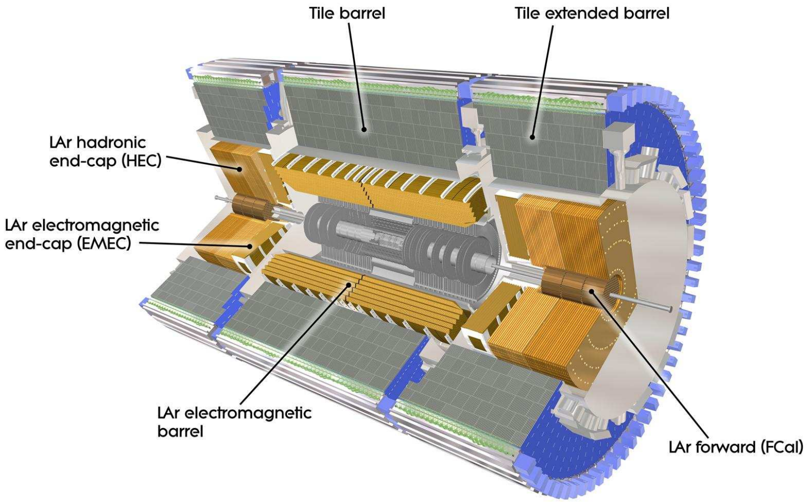
Tile barrel
Tile extended barrel
LAr hadronic end-cap (HEC)
LAr electromagnetic end-cap (EMEC)
LAr electromagnetic barrel
LAr forward (FCal)

FIGURE 2.5: Layout of the Calorimeter system.

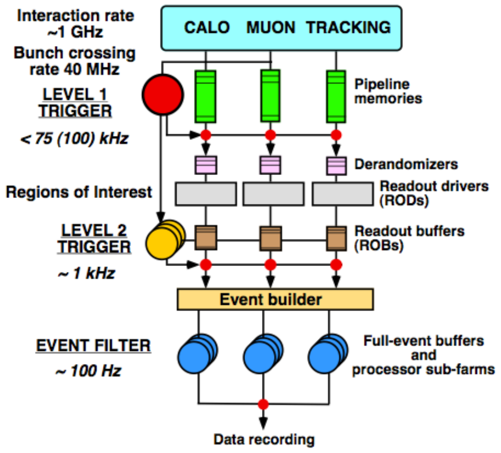
Interaction rate ~1 GHz
Bunch crossing rate 40 MHz
LEVEL 1 TRIGGER
< 75 (100) kHz
Regions of Interest
LEVEL 2 TRIGGER
~ 1 kHz
EVENT FILTER
~ 100 Hz
CALO MUON TRACKING
Pipeline memories
Derandomizers
Readout drivers (RODs)
Readout buffers (ROBs)
Event builder
Full-event buffers and processor sub-farms
Data recording

FIGURE 2.6: Schematic layout of the ATLAS Trigger-DAQ system.

Chapter 3

STUDY OF THE INFRARED AND COLLINEAR REGION IN $t\bar{t}jj$ EVENTS

> *"The status of QCD is that of a successful symbiosis of astrophysics (ideas), astronomy (observation) and astrology (inspiration).*
> *Successful - because it represents a rare example of a field in which we are capable of predicting so much while understanding so little."*
>
> Yu. Dokshitzer.

3.1 Motivation

Probing the origin of the electroweak symmetry breaking or discovering new physics at the LHC requires as a first step the extraction of the corresponding signals from a huge background of mostly uninteresting QCD events (cf. Fig. 3.1). With top-quark pairs being produced at the order of 1 per second at design luminosity, the LHC will be a top-quark factory. This makes events with top quarks important as a signal process as well as a source of background for other processes.

More precisely, the study of top-pair production in association with additional jets serves as a test for

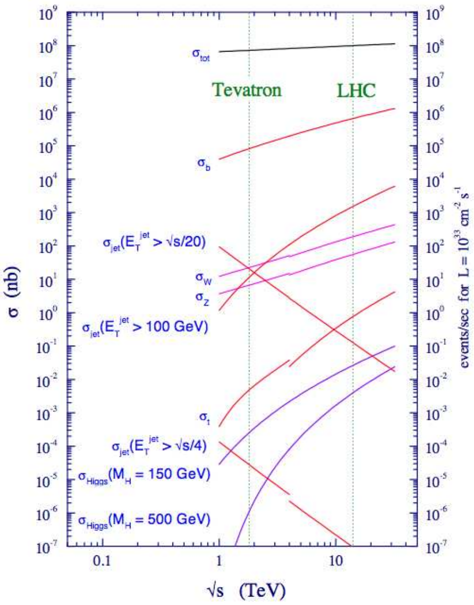

FIGURE 3.1: Predicted contributions to the Standard Model cross section for $pp, p\bar{p}$ collisions [53].

perturbative QCD, with NLO calculations becoming available only recently [54–58]. The measurement of the additional jet production-rates will aid in reducing the modeling uncertainties of Initial and Final State Radiation in $t\bar{t}$ events and also provide a more precise understanding of $t\bar{t}$ events topology, where the presence of the additional jets has been shown to increase significantly the failure rates of the kinematic reconstruction algorithms. Moreover, since the top-quark mass is orders of magnitude higher than the rest of the quarks, it provides a handle for assessing theory predictions at scales where new physics is expected to be found. Top-pair events with additional jets can also provide access to the top-charge asymmetry [59], which is a $\mathcal{O}(a_s^3)$ effect, having thus the potential to shed light on the discrepancy recently reported by the CDF collaboration [60].

On the other hand, $t\bar{t}+$ jets events constitute an important (and sometimes the dominant) background in the Higgs and SUSY searches. The case with 2 additional jets, is particularly important for the Higgs searches in the low-mass region, where the Higgs is produced in association to a $t\bar{t}$ pair and decaying to $b\bar{b}$. For this channel, the $t\bar{t}b\bar{b}$ process constitutes the irreducible background and $t\bar{t}jj$ (with j denoting a light-flavoured jet) constitutes the reducible background, as shown in Fig. 3.2. The latter has to be taken into account due to the finite purity of flavour tagging. It has been shown [61] that although a Higgs signal could be established with 3σ significance in the $t\bar{t}H$ channel with around $\mathcal{L} = 60$ fb^{-1} of integrated luminosity, the signal reconstruction is undermined by the presence of the additional jets which hinders the kinematic reconstruction of the event. A channel whose dominant background comes from $t\bar{t}jj$ production is $pp \to H(W^+W^-)jj$, which is of particular interest for Higgs searches in the mass region $140 \lesssim m_H[\text{GeV}] \lesssim 190$. We see thus that a precise determination of the QCD production of jets in association with $t\bar{t}$ pairs is important for Higgs searches.

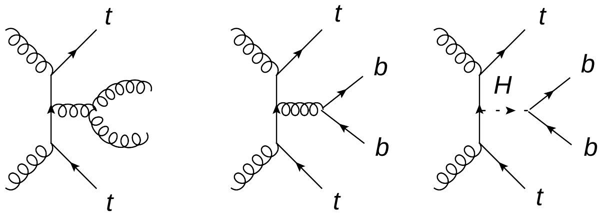

FIGURE 3.2: Reducible (left) and irreducible (center) background to the $pp \to t\bar{t}H(b\bar{b})$ process (right).

The production of $t\bar{t}+$ jets events can also figure among the most important background processes for a series of channels used for SUSY searches, whose typical signatures involve multijet final states

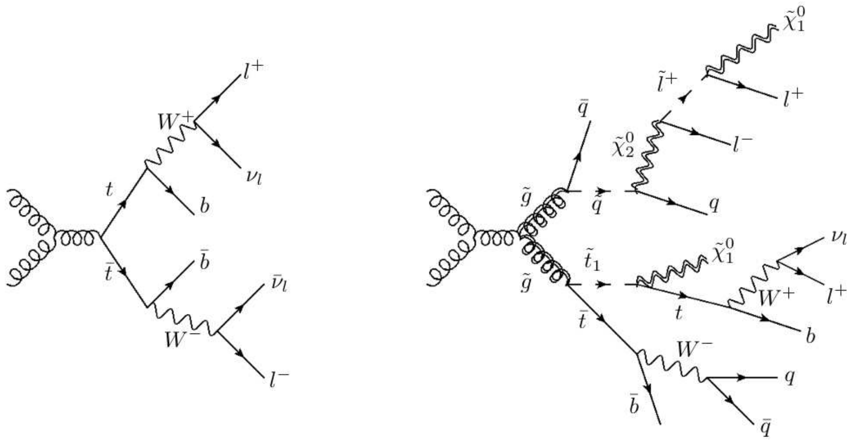

FIGURE 3.3: Top-pair production (left) and gluino production (right).

with a large missing transverse energy. Top-pair events contain b quarks and W bosons, which can also decay hadronically, mimicking the typical SUSY signals. In the case where additional jets are considered, one has a considerable freedom to choose the decay modes of the W bosons and as a consequence, $t\bar{t}+$ jets events can plague several SUSY channels. The situation is deteriorated in the case where the 3rd generation squarks are lighter than the other squark generations [62].

3.2 Matrix element calculation

The existing $t\bar{t}+$ jets calculations [54–58] are performed only at the Matrix Element level, with implementations into showering and hadronization generators barely starting to become available [63]. As a consequence, one cannot use them directly to make predictions for hadron observables before passing them through the subsequent steps of showering, hardronization and decays that we described in the previous chapter. For the $t\bar{t}jj$ calculations [56–58], the first step towards this direction would be to implement these calculations in one of the NLO parton matching schemes: MC@NLO or POWHEG. This going beyond the scope of this work, we will limit ourselves to the study of the soft and collinear region in $t\bar{t}jj$ events[1] and try to see where the parton shower is expected to alter significantly the matrix element spectrum.
The most recent $t\bar{t}jj$ calculations [58] use the setup shown in the Table 3.1. We note that that $t\bar{t}jj$ is the first process among the class of $t\bar{t}+$ jets events, where the Born contributions begin to diverge. This is easily seen if we consider for example eq. (1.41). For the emission of a gluon from a massive quark, the matrix element would now be proportional to

TABLE 3.1: Setup for ME $t\bar{t}jj$ calculation as in [58]

Parameter	Value
$\sqrt{s}$	7 TeV
PDF	MSTW2008NLO [64]
m_t	173.3 GeV
$m_q, q \neq t$	0
Scales	$\mu_R = \mu_F = m_t$
Jet Veto	$p_T^{jet} > 50$ GeV
Rapidity cut	$\|y_j\| < 2.5$
Jet separation	$\Delta R_{jj} > 0.5$

$$\frac{1}{(p_1+k)^2 - m^2} = \frac{1}{2p_1 \cdot k} = \frac{1}{2E_g E_q (1 - \beta \cos\theta_{p_1 g})}, \tag{3.1}$$

where $\beta = |\vec{p}_1|/E_q$ and thus the collinear divergence for $\theta_{p_1 g} \to 0$ becomes a collinear enhancement. One can easily see that in $t\bar{t}j$ events, all possible branchings contain massive quarks, so the matrix element will contain propagators of the form (3.1). However in $t\bar{t}jj$ events there are branchings between 3 massless partons, as shown in Fig. 3.2 and one recovers the infrared and collinear singularities discussed in the introductory chapter. If we recall the probability for generating an unweighted event in a region of the phase space parametrized by x_i: $P = \frac{(d\sigma/dx)_i}{(d\sigma/dx)_{\max}}$, we immediately see that a divergence in $x \to 0$ would lead to a non-physical spectrum with all events being clustered in the first bins in x. In order to overcome this problem, a jet veto is set to $p_T^{jet} = 50$ GeV for the softest jet in the event.

---

[1] We note that, in the following, j refers to a light-flavoured jet.

The goal of the next section is to estimate how much the jet veto can be lowered with the perturbative ME calculation remaining valid, or, in other words, estimate where the soft and collinear logarithms start to dominate the cross section.

3.3 Study of infrared and collinear divergences

In order to estimate the region where the soft and collinear logarithms dominate the $t\bar{t}jj$ cross section, we have to compare a fixed-order calculation with a calculation at the same perturbative order interfaced to a parton shower. For the fixed-order calculation we use the Alpgen generator [65] which provides a LO calculation of $t\bar{t} + n$ jets, with $n \leq 6$. For the parton shower we interface the Alpgen samples with the HERWIG generator [66] and the Jimmy plug-in [67] for the simulation of Multiple Parton Interactions. The parameters used in each step of the event generation can be found in Appendix A.

Alpgen uses the MLM matching scheme with the matching parameters set to $E_T^{clus}, R_{clus}, \eta_{clus}$ as shown in the Table A.1. In order to perform a study of a process containing up to n additional jets, one has to produce the complete set of multiplicities $X + i$ jets, with $0 \leq i \leq n$, with the last sample generated in inclusive mode and the rest of the samples generated in exclusive mode. We note here that when one uses the MLM matching option, the code performs the α_s reweighting according to the MLM algorithm that was presented in Section 1.3.4, thus effectively pushing the Matrix-Element sample away from the soft and collinear region. As a consequence, in order to obtain a pure Matrix-Element sample, one has to disable the MLM matching.

For this study, showered samples containing up to 2 jets coming from the matrix element were produced in exclusive mode, whereas the highest multiplicity sample with 3 additional jets was produced in inclusive mode. Due to the extremely low unweighting efficiency of samples containing high-multiplicity final states in Alpgen, the Matrix-Element sample produced locally (ME) contained only weighted events and was produced with three additional jets in exclusive mode, with the MLM matching disabled. Jets were reconstructed with the anti-k_T algorithm with a radius parameter $R = 0.4$ and they were subject to a minimal set of selection criteria, i.e. $p_T^{jet} > 15$ GeV, $|\eta_{jet}| < 6, \Delta R_{jj} > 0.7^{\dagger}$ which coincide with the generation cuts. Jets were further characterized as coming from a top decay or as additional jets. Jets coming from a top decay were required to contain a decay product of the top quark within a radius $\Delta R = 0.4$ from the jet axis.

In order to see how the parton shower works, one can, as a first step, choose an observable which is well-defined in all of the phase space, such as the p_T spectrum of the top quark, shown in Fig. 3.4. All of the distributions presented here are normalized to $N = \int_0^{500} \frac{dN}{dp_T} dp_T$ and the error bars on the respective plots account only for the statistical errors. It is obvious from Fig. 3.4, that adding the parton shower makes the p_T spectrum softer due to gluon emissions that carry away a part of the p_T of the parent quarks. The spectra of the leading and subleading additional jets (Fig. 3.5) follow the same pattern, with the ME spectrum being finite at low p_T as expected.

Fig. 3.6 shows the p_T distribution of the 3rd leading additional parton in the event (or its associated jet in the case of the showered samples). In the low-p_T region it is clear that the ME calculation diverges due to the large logarithms from soft and collinear gluon emission. The Parton Shower on the other hand systematically resums such kind of contributions, thus rendering the observable finite at low p_T. As shown in Fig. 3.6(b), the parton shower p_T spectrum displays a turning point at $p_T \approx 23$ GeV, which produces the characteristic "Sudakov peak". This signals the breakdown of the fixed order perturbative result (ME). One can thus say that at values $p_T \lesssim 25$ GeV the ME result is not valid. In the high-p_T region ($p_T \gtrsim 80$ GeV) the two spectra have the same slope, which indicates that the ME contribution dominates the high-p_T region, as expected.

One could also establish a rule of thumb for estimating where the logarithms from soft and collinear

---

[†] Here j denotes both jets containing top-decay products and additional jets.

gluon emission become important by recalling that the leading logarithms are of the form $\alpha_s \ln^2 \frac{Q^2}{\mu^2}$, where Q is the hard scale of the process. Solving for μ one has

$$\mu = Q \exp\left[-\frac{1}{2\sqrt{\alpha_s}}\right]. \tag{3.2}$$

Logarithms from soft and collinear gluon emission will spoil the convergence of the fixed order expansion for $\mu = \mathcal{O}(1)$. It is obvious from (3.2), that the 'soft scale' μ is proportional to the hard scale Q and thus the region where soft and collinear logarithms dominate the cross section is process dependent. For example, for top-quark production, with the hard scale set by the top mass, this argument leads to a soft scale of $p_T \lesssim 35$ GeV, while for the production of SUSY particles, this region could extend to hundreds of GeV.

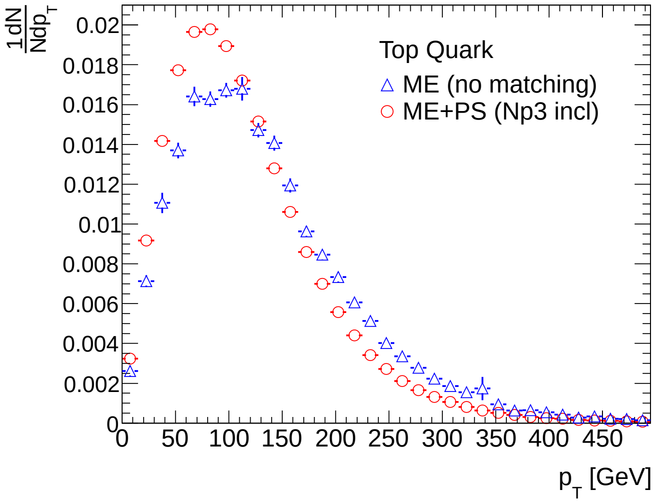

FIGURE 3.4: p_T spectrum of the top quark (or associated jet) given by the ME (without matching) and ME+PS (Np3 inclusive sample) calculations. Only statistical uncertainties are shown.

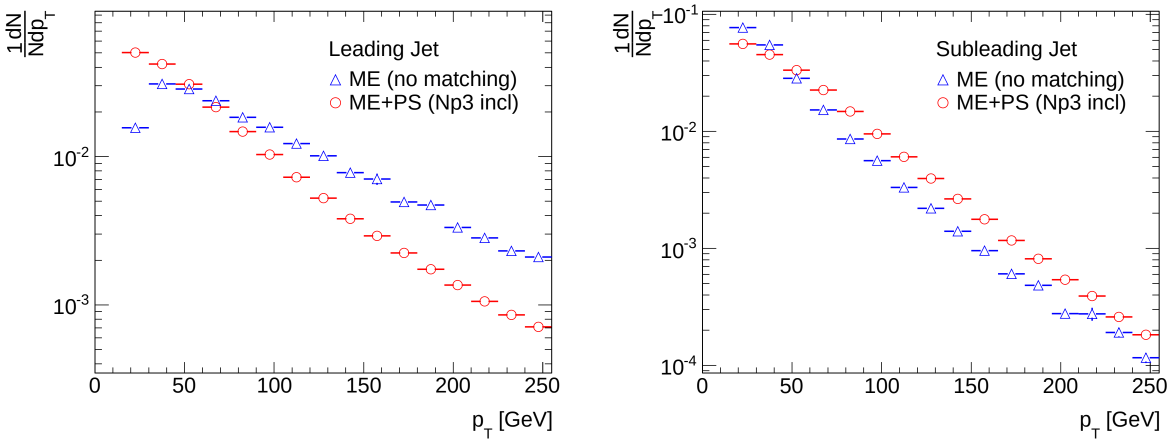

(a) Leading Jet (b) Subleading Jet

FIGURE 3.5: p_T spectrum of the leading (a) and subleading (b) additional parton (or associated jet) given by the ME (without matching) and ME+PS (Np3 inclusive) calculations. Only statistical uncertainties are shown.

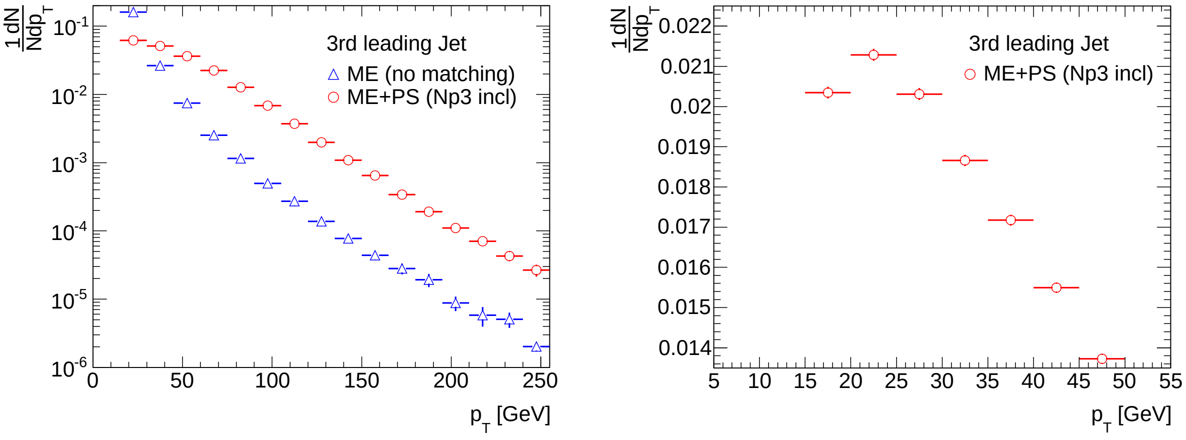

(a) (b)

FIGURE 3.6: (a): p_T spectrum of the 3rd leading additional parton (or associated jet) given by the ME (without matching) and ME+PS (Np3 inclusive) calculations. (b): Same as (a), but plotted on a linear scale and with finer binning. Only statistical uncertainties are shown.

3.4 Conclusions

This chapter addressed the question of where large logarithms spoil the convergence of fixed order perturbative calculations for $t\bar{t}+$ jets processes. By reconstructing the p_T spectrum of the 3rd hardest jet in the event, it was proven that the region $p_T \lesssim 25$ GeV is dominated by soft and collinear emissions and can thus only be described correctly by resumming the associated large logarithms through the parton shower approach.

The problem of merging the parton shower calculation with the fixed order result at LO can be addressed by the MLM matching scheme. There one needs to define two set of parameters for the matching: the generation cuts $p_T^{\min}, \Delta R_{\min}, \eta_{\max}$ and the matching parameters $E_T^{clus}, R_{clus}, \eta_{clus}$. Additional partons are produced by the matrix element in the region $p_T^{parton} > p_T^{\min} \leq E_T^{clus}, \Delta R_{parton} > \Delta R_{\min} \leq R_{clus}, |\eta_{parton}| < \eta_{\max} \geq \eta_{clus}$ and from the parton shower in the complementary region. The generation cuts should be tighter than the matching cuts, so as to ensure a complete coverage of the phase space. A usual choice is to set $E_T^{clus} = \max\left(p_T^{\min} + 5, 1.2 p_T^{\min}\right)$. Choosing a lower energy scale would force the ME generator to fill-in a larger part of the phase space. Eventually generated events which would lie in the Sudakov region would have to be rejected by the matching procedure, enhancing the merging effects. If the matching is done in a consistent way, the observables should be independent of the parton-level generation cuts and in particular should converge for $p_T^{\min}, \Delta R_{\min} \to 0$. Some dependence on the matching and generation cuts may however still be present in the distributions after the parton-jet matching. This should eventually be accounted for in the systematics.

It has to be emphasized, that although these studies might give an indication as to how the process phase-space is generally structured, when one wants to implement a merging scheme for a NLO calculation, a similar study should be performed in the framework of the NLO matching scheme for consistency [68]. For processes involving divergent Born contributions, the typical procedure is to apply a generation cut $p_T^{\min}$ at the matrix-element level and an analysis cut $p_T^{an} > p_T^{\min}$ after the parton shower. The generation cut should then be lowered with the analysis cut remaining fixed, until the sample obtained after the analysis cut remains unchanged under the change $p_T^{\prime\min} < p_T^{\min}$.

Chapter 4

CALCULATION OF $Wb\bar{b}$ WITH aMC@NLO

4.1 Motivation

The production of electroweak bosons in association with jets, in particular jets originating from b quarks, are among the most prominent backgrounds for a series of interesting signal processes under study at the Tevatron and the LHC (Fig. 4.1). More precisely, $Wb\bar{b}$ is a background to single top or top-pair production, whose mechanism involves the decay of the top to a W boson and a b quark, the "Higgsstrahlung" process [69] which involves a W boson produced in association with a Higgs decaying to a $b\bar{b}$ pair and also to certain searches for physics beyond the Standard Model. The MSSM or 2-Higgs Doublet Models [70] feature signals, whose final states ($H/Ab\bar{b} \to \tau^+\tau^-b\bar{b}$) can have a contamination from $Zb\bar{b} \to l^+l^-b\bar{b}$. Moreover, the recent measurements of $W + b$-jet production from the CDF collaboration [71] and from the ATLAS collaboration [2], indicate an excess over the theoretical prediction by a factor of $2.5 - 3.5$ (CDF) and 1.5σ (ATLAS). A precision calculation of $Wb\bar{b}$ production is thus interesting per se.
In this chapter we will use the new aMC@NLO software [72] to study the $Wb\bar{b}$ process, calculating its cross section and presenting several differential distributions with full NLO accuracy. In the beginning of the chapter we will briefly describe the software and the details involved in the theoretical calculation of the $Wb\bar{b}$ process. Then we will present a series of consistency checks performed on a $Z/\gamma^*b\bar{b}$ sample. Finally we will present the result of our calculation.

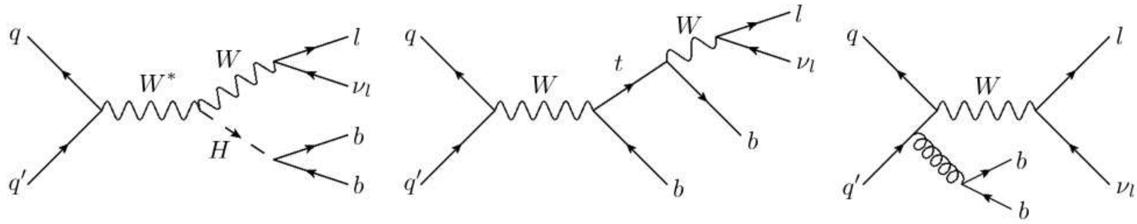

FIGURE 4.1: Example of processes containing a $Wb\bar{b}$ final state: WH production (left), single top (middle), QCD $Wb\bar{b}$ (right).

4.2 The aMC@NLO framework and details on the calculation

The aMC@NLO[1] is a matrix element generator, which can *a priori* be used for the generation of unweighted events described by a given theory and interfaced with the currently available showering

---

[1] 'a' stands for automatic.

and hadronization generators. We stress the ‘a priori’, since its current implementation is bound by certain restrictions[2], inherited from the software on which aMC@NLO is built.
Recalling eq. (1.63), it is clear that for a numerical NLO calculation one needs the Born and real contributions together with the finite part of the virtual contributions and the counterterms. In aMC@NLO the Born and real contributions and the counterterms are calculated by MadFKS [76]. MadFKS uses MadGraph for the calculation of the Born matrix elements and the FKS subtraction formalism [77] to calculate the real contributions and the counterterms. The FKS formalism proposes a way to partition the phase space, in which, in each partition there is at most one infrared and at most one collinear divergence. For partons i, j that can generate infrared or collinear divergences one introduces a set of partition functions $\mathcal{S}_{ij}$ that must satisfy $\sum_{i,j} \mathcal{S}_{ij} = 1$ and uses the “plus-prescription” (1.25) to regulate the real-emission divergences:

$$d\tilde{\sigma}^R = \sum_{i,j} \left(\frac{1}{\xi_i}\right)_+ \left(\frac{1}{1-y_{ij}}\right)_+ \xi_i(1-y_{ij})\mathcal{S}_{ij}|M_{n+1}|^2 d\Phi_{n+1}, \tag{4.1}$$

with $\xi_i = E_i/\sqrt{\hat{s}}$, $y_{ij} = \cos\theta_{i,j}$ and the infrared and collinear divergences appearing for $\xi \to 0$ and $y_{i,j} \to 1$ respectively. The part of the framework that calculates the one-loop corrections is dubbed MadLoop. It uses the OPP reduction method [78] for the evaluation of tensor integrals as implemented in CutTools [79]. MadLoop’s working concept is based on the principle that any loop diagram can be obtained by cutting one and only one of the propagators in the loop. MadLoop thus uses MadGraph which can generate the so-called L-cut diagrams, containing two additional final-state partons[3]. The loop diagrams are then reconstructed by appropriately sawing the L-cut diagrams as shown in Fig. 4.2. Lastly, in order to get predictions for physical observables, one needs to add the parton shower to the parton level results. In the aMC@NLO framework, the MC@NLO method is used for the matching. We also note that the code contains a reweighting module that can be used to compute the cross-section uncertainties coming from the variation of the scales and the PDF set without having to regenerate the events. For this, an extended Les Houches Event record [80] is written, containing all the weight information. The idea is then to reweight the unweighted events with a factor $\sigma(\mu, \mathrm{PDF})/\sigma_0$, where σ_0 corresponds to the cross section obtained by the central value of the scales and PDF and $\sigma(\mu, \mathrm{PDF})$ represents the cross section obtained with a different set of scales and/or PDF. The associated uncertainties are then calculated using the formulae in Section 1.5.

The $Wb\bar{b}$ and $Z/\gamma^* b\bar{b}$ processes have already been studied by the aMC@NLO authors in [1]. For the former case, the aMC@NLO calculation included massive b quarks and off-shell W as was previously

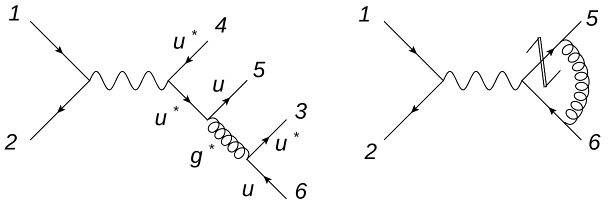

FIGURE 4.2: Working concept of MadLoop: generation of loop diagram (right) from L-cut diagram (left) obtained with MadGraph.

---

[2] The current version of the code, based on MadGraph4 [73], has the following constraints [74]: (i) the process must have a contribution at the Born level, (ii) the process must not contain any 4-gluon vertices, (iii) all Born contributions must contain the same powers of α_s and α_{EW}, (iv) at least one quark must be present in the external states of the input process, (v) the process must not contain correction involving EW gauge bosons circulating in the loops and (vi) finite-width effects of unstable massive particles appearing in the loops cannot be treated, (vii) only Standard Model processes are allowed. These restrictions will be overcome once the interface to MadGraph5 [75] becomes available.

[3] These can also be Fadeev-Popov ghosts.

presented in [81]. The $Z/\gamma^* b\bar{b}$ calculation with aMC@NLO was the first to include massive b quarks together with off-shell effects and full spin correlations. The main difference of the calculation in Section 4.4 from the one in [1] lies in the use of an off-diagonal CKM matrix and the inclusion of massive τ leptons.

4.3 Consistency checks on the $Z/\gamma^* b\bar{b}$ sample

Before using the code for the generation of new processes, a consistency check was performed on the parton shower and hadronization steps of the calculation using an existing $Z/\gamma^* b\bar{b}$ sample generated with aMC@NLO, with the aim of reproducing the results found in [1]. The sample used for showering was produced by the authors of aMC@NLO[4] with the settings used in [1]. The parton-level sample contained a cut on the dilepton invariant mass $m_{l^-l^+} > 30$ GeV. The same cut was applied at the particle level. HERWIG was used for showering and hadronization. The necessary input parameters are given in Table A.3 of Appendix A. We note that the B hadrons have been set stable, in order to avoid reconstructing leptons coming from B-hadron decays. Jets were reconstructed with the anti-k_T algorithm with radius parameter $R = 0.5$ and each jet was required to have $p_T > 20$ GeV$and|\eta| < 2.5$. A b jet was defined as a jet that contained at least one B hadron within $\Delta R \leq 0.5$ of the jet axis and a bb jet was defined as a jet containing at least two B hadrons within $\Delta R \leq 0.5$ of the jet axis.
A series of distributions obtained with the analysis described above is shown in Figs 4.3-4.13. The histogram entries were weighted by the factor σ/N, where $\sigma = 15.94$ pb is the total cross-section obtained with the settings of [1] and N is the number of entries of each histogram. Fig. 4.3 shows the b-jet multiplicity as a fraction of the total number of events. The bb-jet/b-jet fraction is given by $\frac{N_{1,bb}}{N_{1,bb}+N_{1,b}}$, where $N_{1,bb}$ is the number of events containing exactly one bb jet and $N_{1,b}$ is the number of events containing exactly one b jet. Events containing more than 2 b jets or more than 1 bb jet are below the per mille level. Fig. 4.4 shows the invariant mass distribution of the e^-e^+ pair produced by the decay of the vector boson in the hard scattering. The distribution peaks at the Z pole mass as expected and the low $m_{l^-l^+}$ tail is due to the γ^* contribution. Figs. 4.5 and 4.6 show respectively the transverse momentum and pseudorapidity spectrum of the electrons and positrons produced in the hard scattering. Figs. 4.7 and 4.8 show respectively the transverse momentum and rapidity spectrum of the dilepton pairs from the hard scattering. Figs. 4.8 and 4.9 show respectively the transverse momentum spectrum of the leading and subleading b jet produced in the hard subprocess, while Figs. 4.11 and 4.12 show the pseudorapidity spectrum of the leading and subleading b jets. The distributions are in agreement with the results presented in [1].

4.4 Results from the $Wb\bar{b}$ calculation with the ATLAS MC11 defaults

The main goal of this thesis was the generation and study of a $Wb\bar{b}$ sample with aMC@NLO using the ATLAS MC11 defaults quoted in Table A.4 of Appendix A. The generation of the full $Wb\bar{b}$ sample requires to generate separately the contributions of each individual channel $W^+b\bar{b}$, $W^-b\bar{b}$ in each possible W decay modes, i.e. e, μ and τ, and to calculate the real emission corrections in each channel separately. After this step the individual channels have to be stitched together and the virtual corrections have to be calculated. The sample receives contributions from 288 channels, 48 of which require virtual corrections.
For the generation of the sample no cuts were used, since the underlying Born process doesn't contain

---

[4] All samples are publicly available at `http://amcatnlo.web.cern.ch/`.

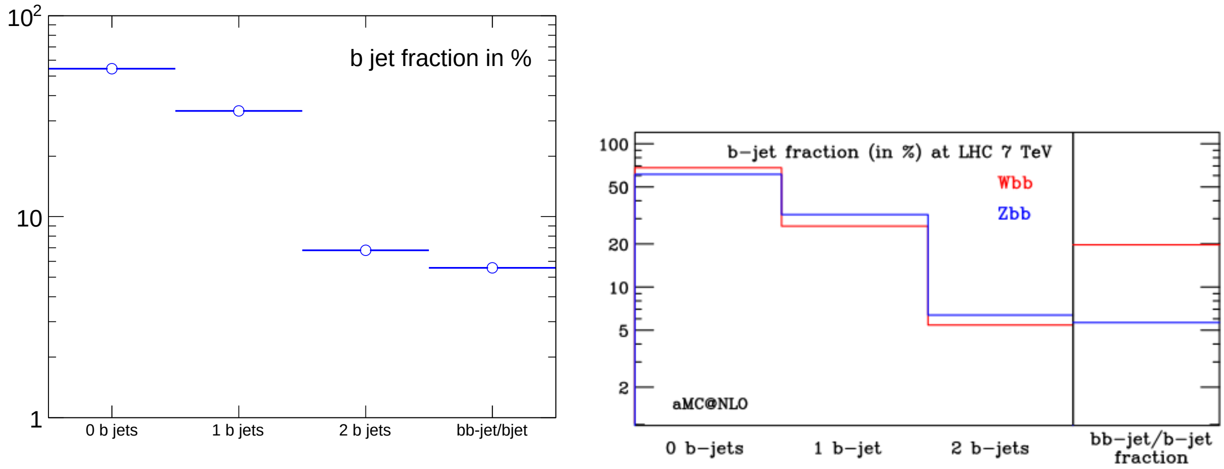

FIGURE 4.3: Fraction of total events containing exactly $0, 1$ and 2 b jets. Left panel: result from the calculation described in the text for the $Z/\gamma^* b\bar{b}$ sample. Right panel: result from [1].

any divergent contributions. The renormalization and factorization scales were set equal to

$$\mu_R = \mu_F = \sqrt{m_{l\nu}^2 + p_T^2(l\nu) + \frac{m_b^2 + p_T^2(b)}{2} + \frac{m_b^2 + p_T^2(\bar{b})}{2}}. \tag{4.2}$$

The obtained cross section at LO was

$$\sigma_{LO}^{Wb\bar{b}} = (46.098 \pm 0.007)\ \text{pb} \tag{4.3}$$

and at NLO:

$$\sigma_{NLO}^{Wb\bar{b}} = (112.144 \pm 0.064)\ \text{pb}, \tag{4.4}$$

giving a K-factor of 2.43. The quoted uncertainty is due to the Monte Carlo integration only. The size of the unweighted-events sample was 10^5 events. For showering and hadronization the HERWIG generator was used and Jimmy was added for simulating multiparton interactions. It has to be stressed out that in approximately 13% of events the Monte Carlo truth-record was broken. This happened only in events containing τ leptons. These events were discarded from the analysis. As a result we expect that the differential distributions presented here will not reproduce the cross section quoted in Eq. (4.4).

The showering was performed with the ATLAS software. Jets were reconstructed with the anti-k_T algorithm with radius parameter $R = 0.4$ and each jet was required to have $p_T > 25\ \mathrm{GeV} and |y| < 2.1$. A b jet (bb jet) was defined as a jet that contained at least one (two) B hadron within $\Delta R \leq 0.4$ of the jet axis. A series of observables, similar to those presented in the $Z/\gamma^* b\bar{b}$ analysis, are shown in Figs. 4.15-4.20. Unless otherwise specified, the histogram entries were weighted by the factor σ/N, where $\sigma = 112.144$ pb is the total cross-section and N is the number of entries of each histogram.

Figure 4.15(a) shows the shows the b-jet multiplicity as a fraction of the total number of events. The bb-jet/b-jet fraction is defined in the same way as for the $Z/\gamma^* b\bar{b}$ sample, i.e. $\frac{N_{1,bb}}{N_{1,bb}+N_{1,b}}$. Events containing more than two b jets are below the per mille level and events containing more than one bb jet were approximately 1.5%. One notices that the fraction of bb quarks in the $Wb\bar{b}$ sample is higher than the one in the $Z/\gamma^* b\bar{b}$ sample. As Fig. 4.15(b) suggests, this happens because the ΔR separation between the B hadrons is smaller for $Wb\bar{b}$ production. This can be explained if we consider

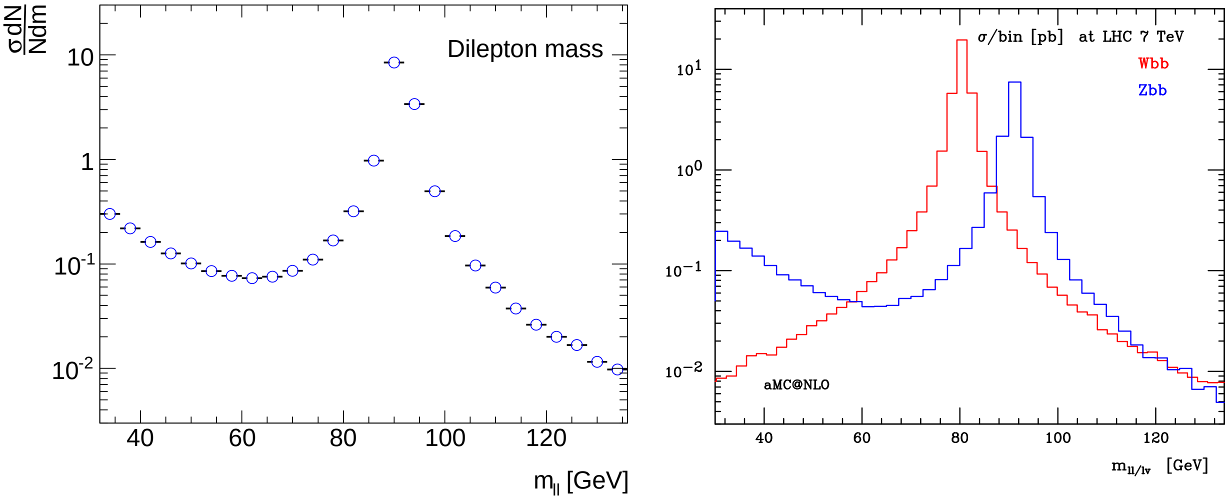

FIGURE 4.4: Invariant mass distribution of final-state dilepton pair. Left panel: result from the calculation described in the text for the $Z/\gamma^* b\bar{b}$ sample. Right panel: result from [1].

the production mechanisms for the 2 processes, shown in Fig. 4.14. For the case of $Wb\bar{b}$, the heavy-quark pairs are produced by gluon splittings and are thus expected to be close in pseudorapidity. This produces the plateau at low ΔR in Fig. 4.15(b). Since the B hadrons will tend to be closer to each other, they will be more often reconstructed as one jet, which in turn leads to an increase of the bb/b-jet fraction. For the case of $Z/\gamma^* b\bar{b}$ production, the dominant production channel is gluon-gluon fusion, where the final-state heavy-quark pairs will tend to have a larger separation in pseudorapidity. Figures 4.16(a) and 4.16(b) show the invariant mass of the dilepton pairs produced by the decay of the W boson in the hard-scattering process and the transverse energy of the associated neutrinos. Figure 4.17(a) shows the transverse momentum distribution of the positively and negatively charged leptons produced in $W^+b\bar{b}$ and $W^-b\bar{b}$ events respectively. Unlike the $Z/\gamma^* b\bar{b}$ case, there is an asymmetry in the two distributions, with the positively charged leptons being produced with a higher cross section. This is expected from the surplus of positive charge in the initial state.

Figure 4.18(a) shows the transverse momentum spectrum of the dilepton pairs produced by the decay of the W boson in the hard scattering process. Figure 4.17(b) shows the pseudorapidity spectrum of the positevely and negatively charged leptons. Comparing this with the same plot for the $Z/\gamma^* b\bar{b}$ sample (Fig. 4.6), one observes two differences. Unlike $Z/\gamma^* b\bar{b}$, in $Wb\bar{b}$ production there is an asymmetry in the pseudorapidity spectra of the positively and negatively charged leptons, with the positively charged ones being produced more centrally. This is explained by the difference of the parton luminosities that are involved in the production mechanisms. This also explains the appearance of a plateau in the rapidity distribution of the dilepton pairs coming from the decay of the W boson, shown in Fig. 4.18(b). Unlike the Z/γ^* production, which is dominated by gluon fusion, W production involves quarks, which tend to carry a larger fraction of the parent hadron's momentum, thus resulting in the production of W bosons at higher rapidities. Figures 4.19 and 4.20 show the transverse momentum and pseudorapidity distribution of the two hardest b jets in the event.

It was found that during the generation of this sample, the same random number seed was used for several of the contributing channels. This would lead to an unphysical clustering of the generated events in certain regions of the phase space. This effect is expected to be more pronounced in regions of low statistics. The unphysical features seen in the high-p_T tail of the lepton, dilepton and subleading b-jet distribution (Figs. 4.17(a), 4.18(a), 4.19(b)) are possibly due to this effect and require further investigation.

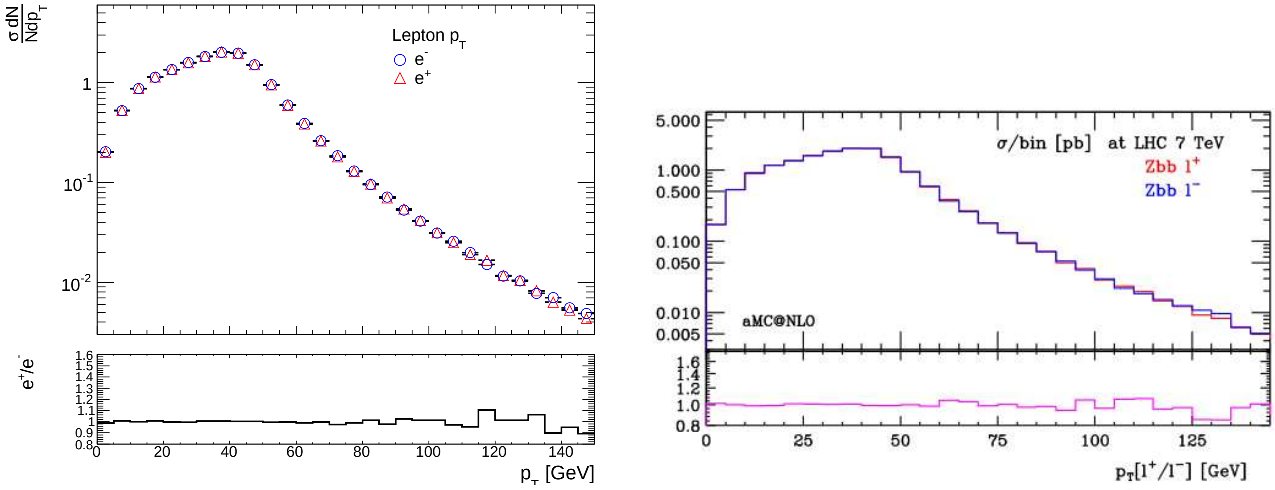

FIGURE 4.5: Transverse momentum of electrons (blue) and positrons (red). Left panel: result from the calculation described in the text for the $Z/\gamma^* b\bar{b}$ sample. Right panel: result from [1]. The inset shows the ratio e^+/e^-.

4.5 Comparison with ATLAS data

In order to compare the aMC@NLO predictions for $Wb\bar{b}$ with data, one has to reduce the aMC@NLO sample, which was produced with no cuts, to the fiducial phase space defined in the recent ATLAS measurement [2] and apply the same selection for the objects. This is achieved by applying the following set of cuts. Leptons are selected if they are matched to a W boson[5] and if they satisfy $p_T^l > 20$ GeV and $|\eta^l| < 2.5$. Neutrinos are selected if they satisfy $p_T^\nu > 25$ GeV. Jets are reconstructed with the anti-k_T algorithm with a radius parameter $R = 0.4$. The jet selection requires $p_T^j > 25$ GeV, $|y^j| < 2.1$. A jet that passes the selection criteria is tagged as a b jet if at least one B hadron is found within a distance $\Delta R_{Bj} < 0.3$ of the jet axis. An event is rejected if no charged leptons or no neutrinos which pass the selection criteria is found. Events containing τ leptons that pass the selection criteria are also rejected. Events are only kept if they further satisfy the following criteria: $m_T^W \equiv \sqrt{2p_T^l p_T^\nu [1 - \cos(\phi^l - \phi^\nu)]} > 40$ GeV, where p_T^l, p_T^ν, ϕ^l, ϕ^ν are the transverse momenta and azimuth of the charged lepton and neutrino that are matched to a W boson. Events are rejected if $n > 2$ or $n_b < 1$ or $n_b > 2$, where n, n_b are the multiplicities of all jets and b jets that pass the selection criteria. An event is also rejected if a selected lepton is found within a distance $\Delta R_{lj} \leq 0.5$ of a selected jet.

Figure 4.21 shows the prediction of aMC@NLO for $Wb\bar{b}$ production, together with the data measured by the ATLAS collaboration [2] in the 1,2 and 1+2 jet exclusive bins, as well as the theoretical predictions obtained with other generators, as described in [2]. Table 4.1 gives the values of the measured fiducial cross section in the combined electron plus muon channel in the 1,2 and 1+2-jet exclusive bins together with the respective quantities predicted by the aMC@NLO calculation.

The predicted result for the combined 1+2-jet bin lies below the measured value, but it is consistent at the 2.1 σ level. The deviation from the measured values is even higher (2.5 σ) for the 2-jet bin. As noted in the previous section, aMC@NLO predicts a high rate of events, where the two b quarks are close enough to be reconstructed as a single b jet. This decreases the predicted cross section in the 2-jet exclusive bin. A measurement with higher precision is necessary in order to draw conclusions and

---

[5] The matching is done using the Monte Carlo truth record and searching for a W boson among the parents of a given particle.

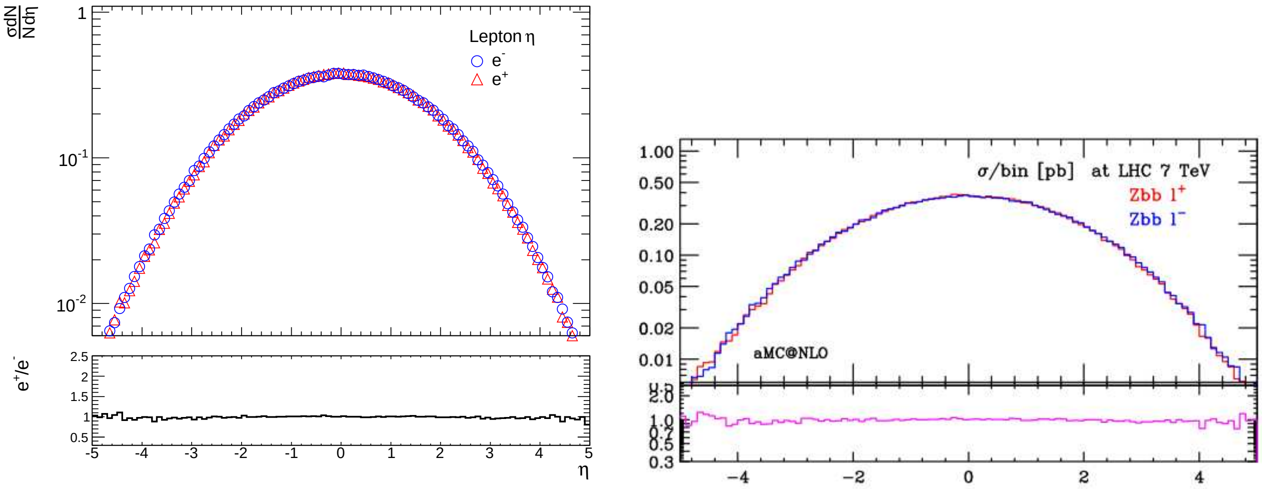

FIGURE 4.6: Pseudorapidity of electrons (blue) and positrons (red). Left panel: result from the calculation described in the text for the $Z/\gamma^* b\bar{b}$ sample. Right panel: result from [1] The inset shows the ratio e^+/e^-.

TABLE 4.1: Predicted and measured values of the $W + b$-jet fiducial cross section in the combined electron plus muon channel.

Fiducial cross section - data [pb]	
1 jet	$4.5 \pm 1.3_{\text{stat}} \pm 1.3_{\text{sys}}$
2 jet	$5.7 \pm 1.3_{\text{stat}} \pm 1.4_{\text{sys}}$
1+2 jet	$10.2 \pm 1.9_{\text{stat}} \pm 2.6_{\text{sys}}$
Fiducial cross section - aMC@NLO prediction [pb]	
1 jet	2.4896
2 jet	0.979
1+2 jet	3.486

further cross-checks are necessary to assess how the unphysical features in the distributions presented in the previous section affect the cross-section prediction.

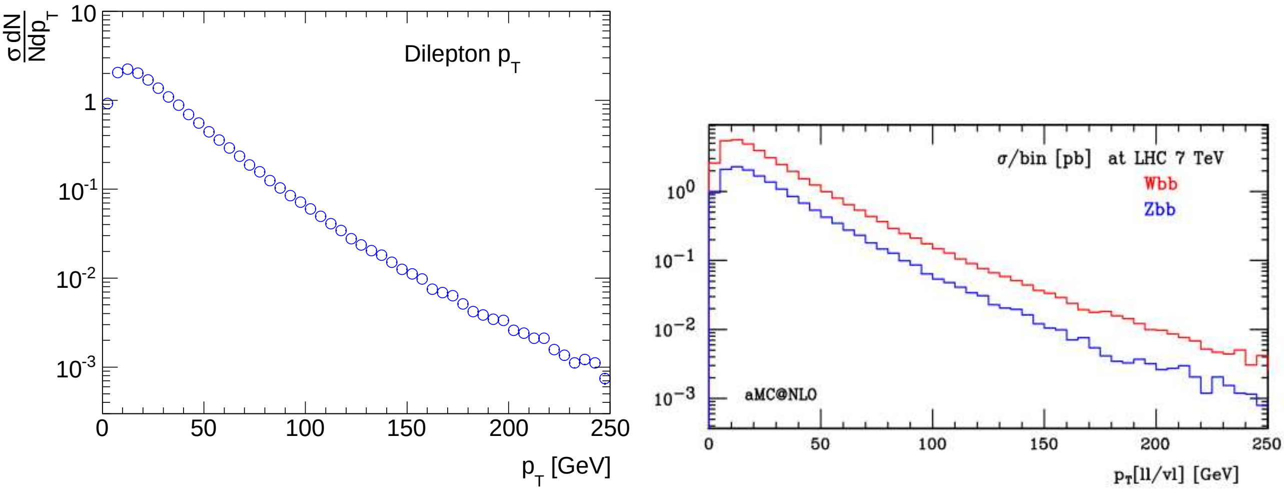

FIGURE 4.7: Transverse momentum of e^+e^- pair. Left panel: result from the calculation described in the text for the $Z/\gamma^* b\bar{b}$ sample. Right panel: result from [1].

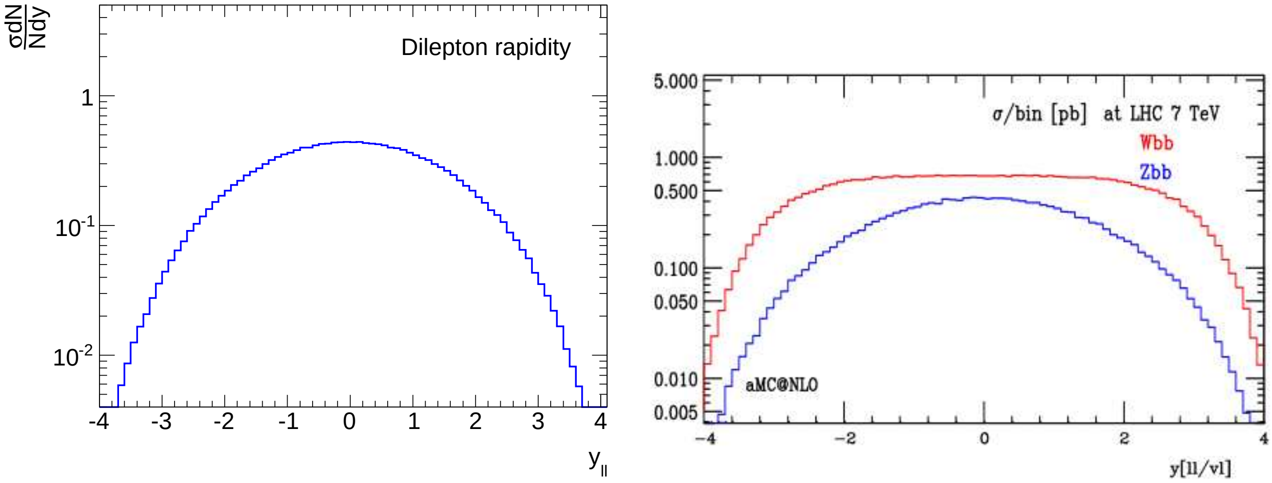

FIGURE 4.8: Rapidity of e^+e^- pair. Left panel: result from the calculation described in the text for the $Z/\gamma^* b\bar{b}$ sample. Right panel: result from [1].

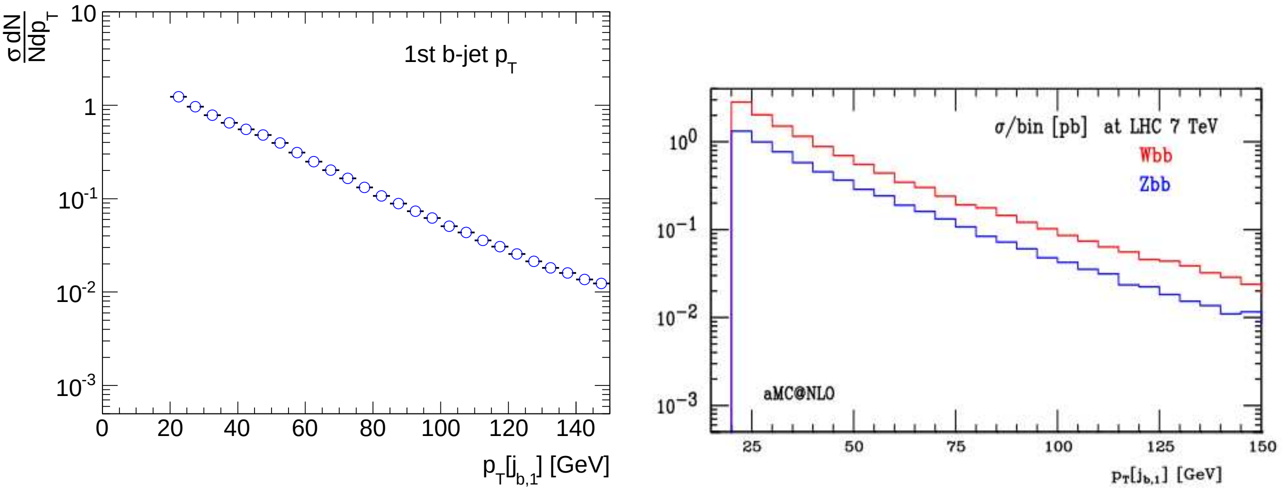

FIGURE 4.9: Transverse momentum of hardest b jet. Left panel: result from the calculation described in the text for the $Z/\gamma^{*}b\bar{b}$ sample. Right panel: result from [1].

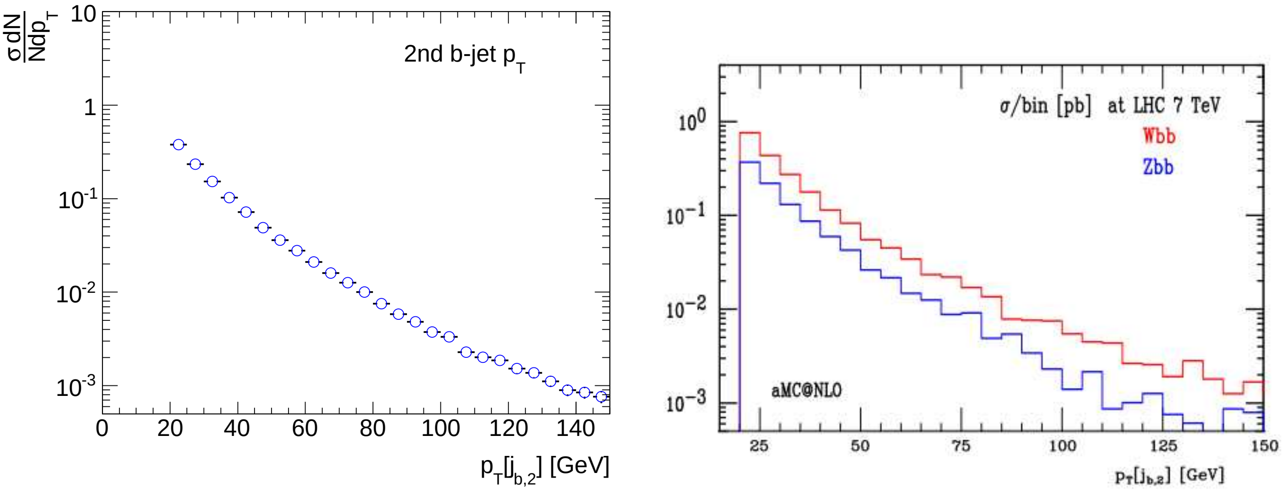

FIGURE 4.10: Transverse momentum of second hardest b jet. Left panel: result from the calculation described in the text for the $Z/\gamma^{*}b\bar{b}$ sample. Right panel: result from [1].

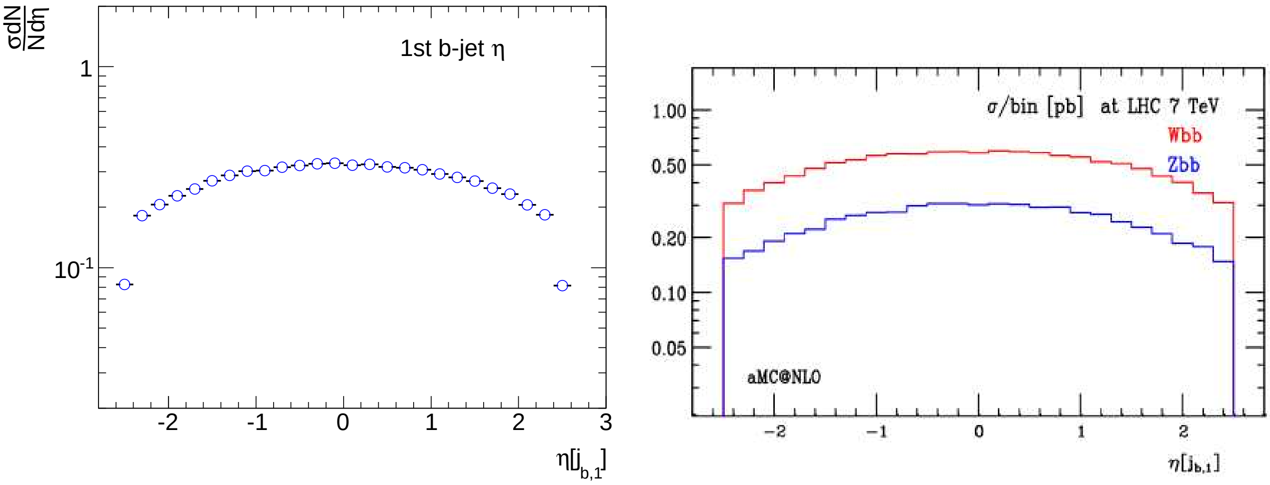

FIGURE 4.11: Pseudorapidity of hardest b jet. Left panel: result from the calculation described in the text for the $Z/\gamma^* b\bar{b}$ sample. Right panel: result from [1].

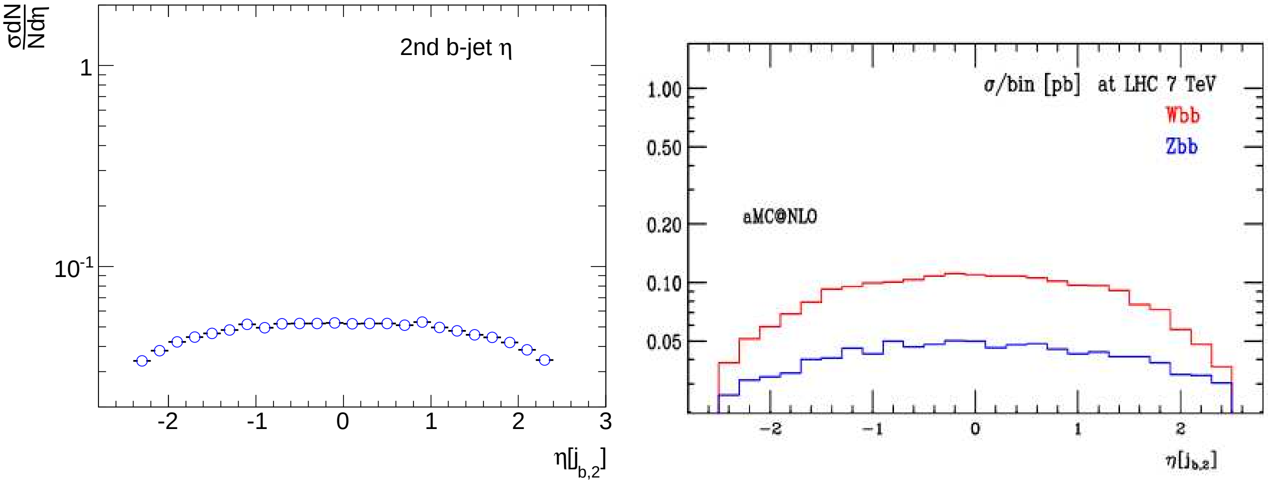

FIGURE 4.12: Pseudorapidity of second hardest b jet. Left panel: result from the calculation described in the text for the $Z/\gamma^* b\bar{b}$ sample. Right panel: result from [1].

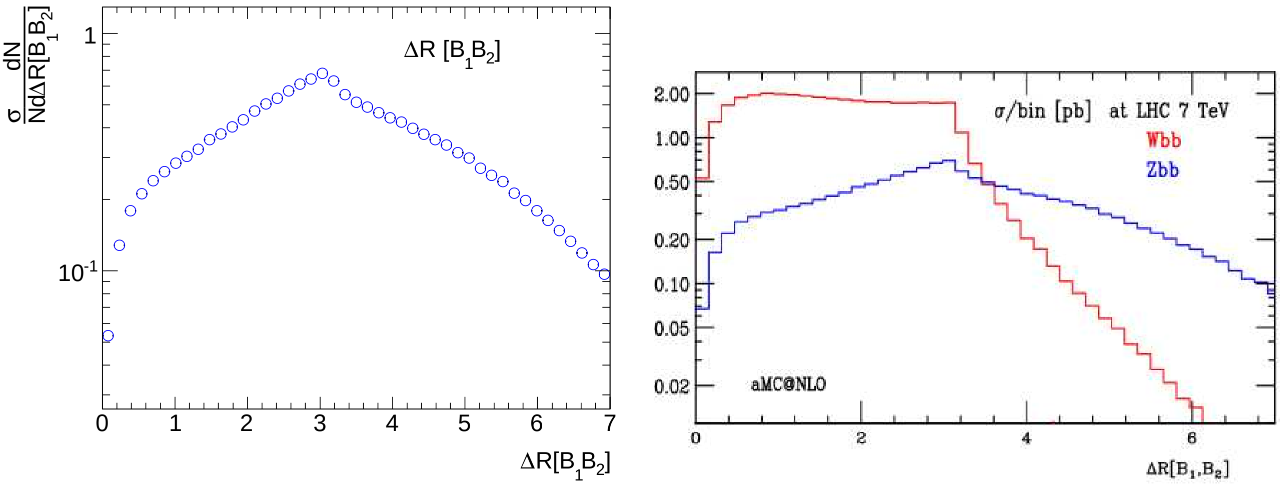

FIGURE 4.13: ΔR separation between the two hardest B hadrons. Left panel: result from the calculation described in the text for the $Z/\gamma^* b\bar{b}$ sample. Right panel: result from [1].

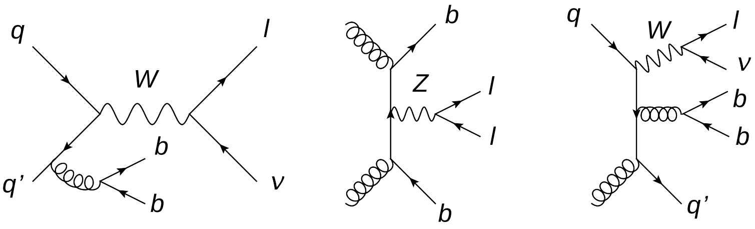

FIGURE 4.14: $Wb\bar{b}$ and $Z/\gamma^* b\bar{b}$ production diagrams at LO (left and center) and NLO (right).

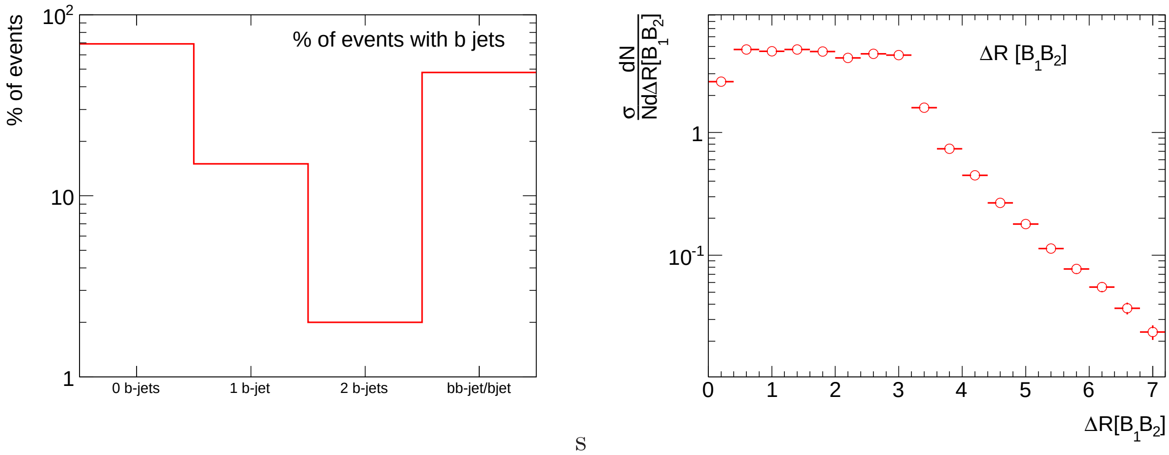

(a) (b)

FIGURE 4.15: (a): Fraction of total events containing exactly $0, 1$ and 2 b jets. (b): ΔR separation between the two hardest B hadrons. The distributions were produced from a $Wb\bar{b}$ sample with the MC11 settings. Only uncertainties associated to the MC integration are shown.

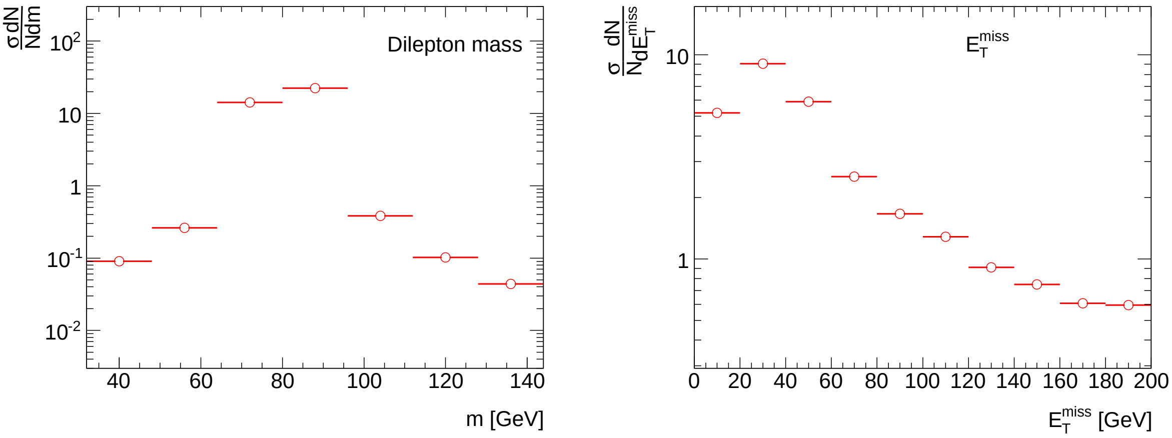

(a) (b)

FIGURE 4.16: (a): Invariant mass of dilepton pairs. (b): Missing transverse energy distribution. The distributions were produced from a $W b\bar{b}$ sample with the MC11 settings. Only uncertainties associated to the MC integration are shown.

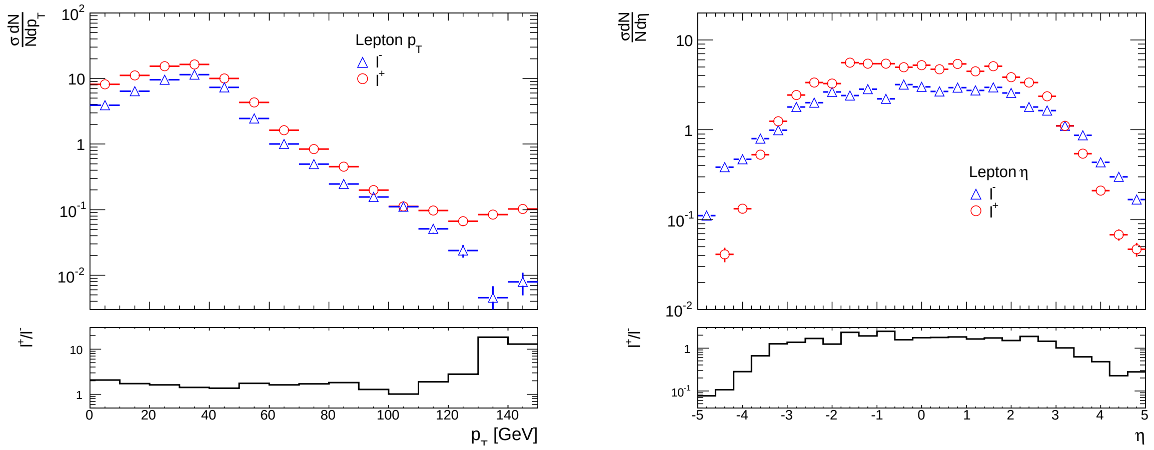

(a) (b)

FIGURE 4.17: Transverse momentum (a) and pseudorapidity distribution (b) of positively (red) and negatively charged leptons (blue) produced by the decay of the W boson. The distributions were produced from a $W b\bar{b}$ sample with the MC11 settings. The insets show the ratio l^+/l^-. The red curves are normalized to $\sigma_{l^+} = 68.9263$ pb and the blue curves are normalized to $\sigma_{l^-} = 43.2172$ pb. Only uncertainties associated to the MC integration are shown.

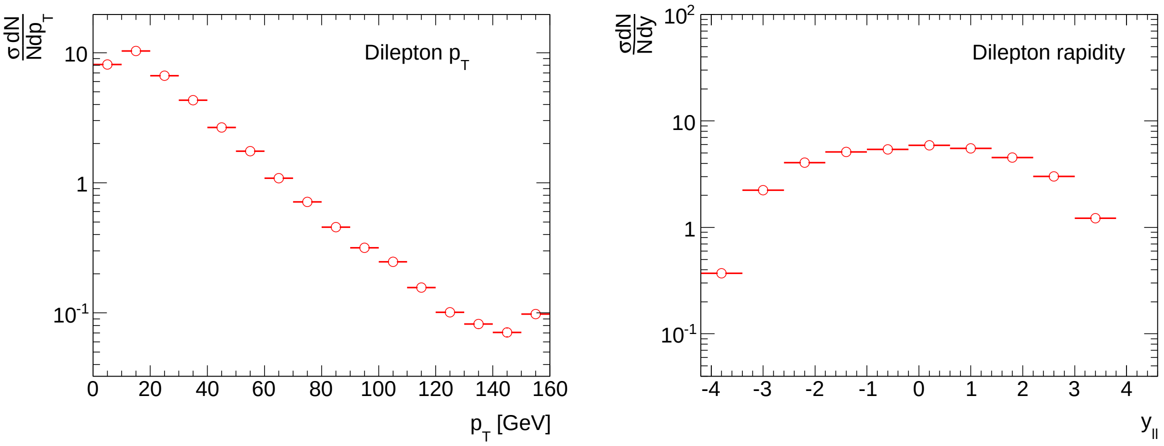

(a)

(b)

FIGURE 4.18: Transverse momentum (a) and rapidity distribution (b) of dilepton pairs produced by the decay of the W boson. The distributions were produced from a $Wb\bar{b}$ sample with the MC11 settings. Only uncertainties associated to the MC integration are shown.

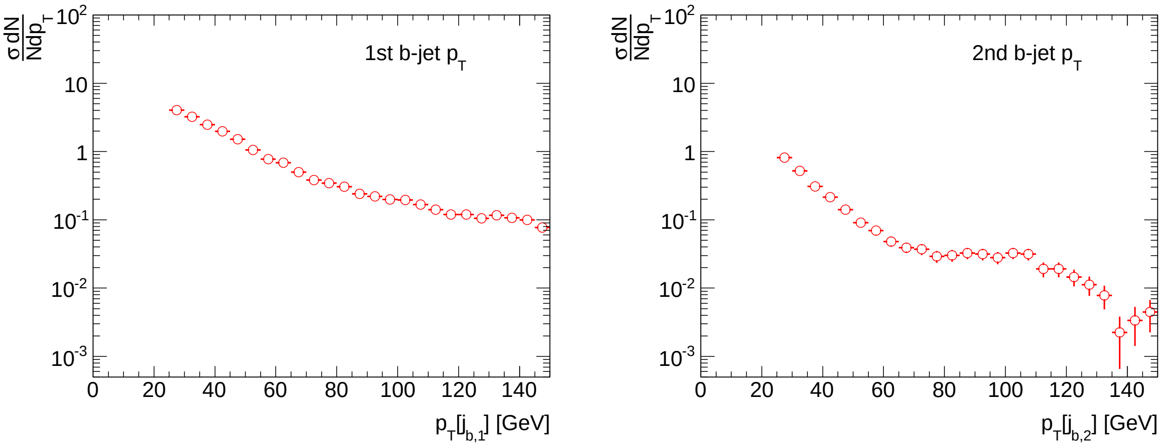

(a) Leading b jet

(b) Subleading b jet

FIGURE 4.19: Transverse momentum distribution of the leading (a) and subleading (b) b-jets in the event. The distributions were produced from a $Wb\bar{b}$ sample with the MC11 settings. The leading b-jet distribution is normalized to $\sigma_{b_1} = 19.7204$ pb and the subleading one to $\sigma_{b_2} = 2.5972$ pb. Only uncertainties associated to the MC integration are shown.

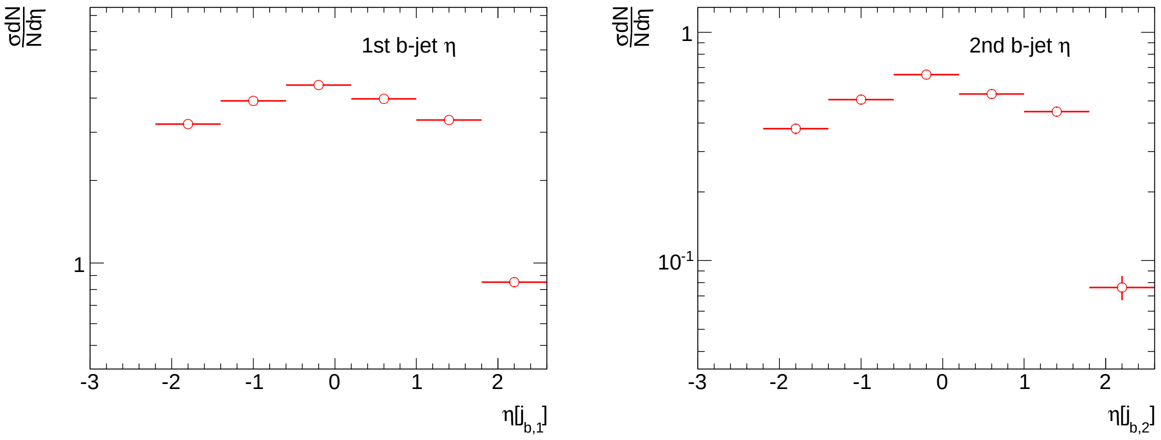

(a) Leading b jet (b) Subleading b jet

FIGURE 4.20: Pseudorapidity distribution of the leading (a) and subleading (b) b-jets in the event. The distributions were produced from a $Wb\bar{b}$ sample with the MC11 settings. The leading b-jet distribution is normalized to $\sigma_{b_1} = 19.7204$ pb and the subleading one to $\sigma_{b_2} = 2.5972$ pb. Only uncertainties associated to the MC integration are shown.

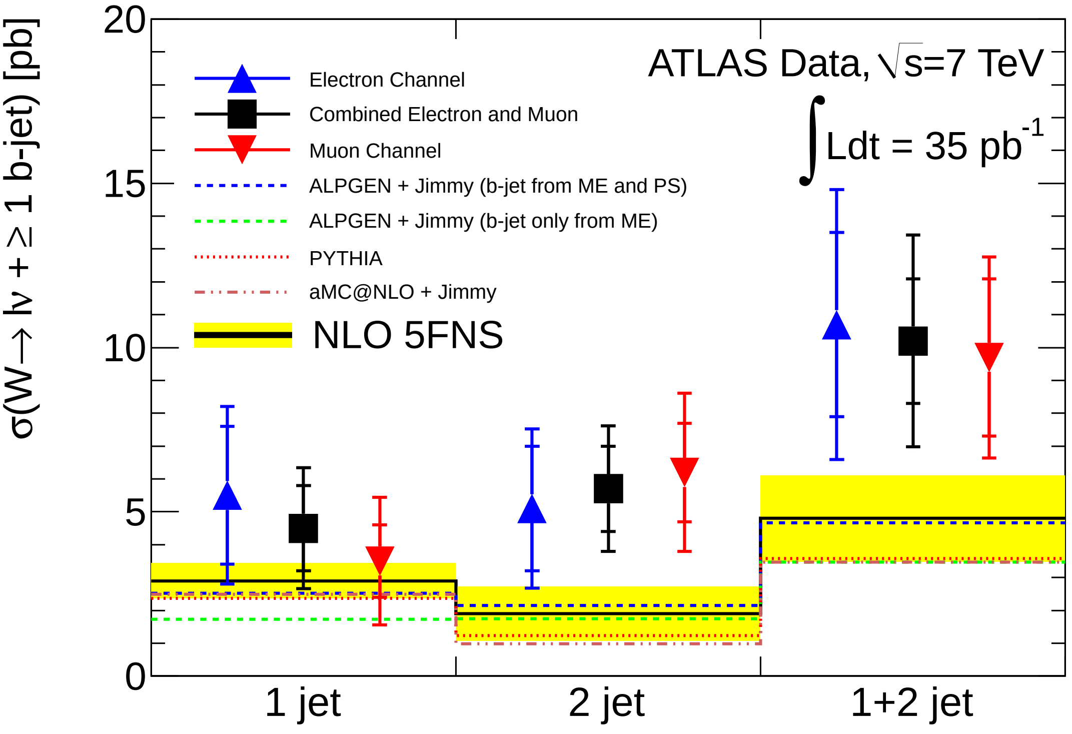

FIGURE 4.21: Fiducial cross section for the production of a W boson in association with one or two b jets measured by ATLAS [2] in the 1, 2 and 1+2 jet exclusive bins. The aMC@NLO prediction is given in brown, in addition to the rest of the theoretical predictions described in [2]. For the aMC@NLO prediction, only the central value is given.

SUMMARY AND PROSPECTS

In this work we studied the soft and collinear region in $t\bar{t}$+jets events and the production of W bosons in association with $b\bar{b}$ pairs at $\sqrt{s} = 7$ TeV.
For the study of the divergences in the low-p_T region in $t\bar{t}$ + jets events we compared the p_T spectra of the softest jets from a Matrix Element calculation produced with Alpgen (with the MLM matching turned off) with a matched calculation produced by interfacing the Alpgen samples with the HERWIG parton shower. The shape of the two spectra suggested that the region $p_T \lesssim 30$ GeV is dominated by soft and collinear emissions and is thus described well by the parton shower, whereas the region $p_T \gtrsim 50$ GeV is hard enough to be described by a fixed-order matrix-element calculation. In the intermediate region, one needs a merging scheme in order to interface a matrix-element calculation with a parton shower. At Leading Order this is achieved e.g. by the MLM scheme, with which the samples used in this study were produced. For the case of a NLO calculation matched to parton shower, a similar study should be redone within the generators that use the existing NLO matching schemes. There, one should set a p_T cut at the matrix-element level, in order to avoid the low-p_T divergences, and an analysis cut p_T^{an} after the parton shower. The optimal value of the generation cut $p_T^{\min}$ would then be equal to the maximum value of $p_T^{\min}$ for which the physical observables obtained after the analysis cut remain unchanged after the substitution $p_T^{\min} \to p_T^{\prime\min}$, with $p_T^{\prime\min} < p_T^{\min}$.
We also calculated the $Wb\bar{b}$ process at NLO accuracy with the aMC@NLO software using the ATLAS MC11 input parameters. This was the first calculation performed with the aMC@NLO software that included an off-diagonal CKM matrix and τ leptons. The complexity of the process required some modifications of the original code. The physical observables presented here were obtained after interfacing the matrix-element calculation of aMC@NLO with the HERWIG generator, within the ATLAS framework. The calculated cross section was $\sigma_{NLO}^{Wb\bar{b}} = (112.144 \pm 0.064)$ pb at NLO and $\sigma_{LO}^{Wb\bar{b}} = (46.098 \pm 0.007)$ pb, giving a K-factor of 2.43. The aMC@NLO prediction was compared against the recent ATLAS measurement [2] of W production in association with one or two b jets. The predicted cross section was below the measured one, although consistent within 2.1 σ for the combined electron plus muon channel and for the 1+2-jet bin.
The aMC@NLO sample was found to contain some unphysical features, which are probably due to the random number seed being the same for several contributing channels. Further cross checks are necessary to assess how this affects the observables presented in this thesis and the predicted cross section. As a following step, one should calculate the cross-section uncertainties related to the PDF and scale choice, as well as to the variation of the b-quark mass. One could also produce a similar sample interfacing with the Herwig++ shower [82] and with PYTHIA[6] [83].

---

[6] At the time of writing of this thesis, only the interface to the virtuality-ordered shower of Pythia6 was available. The interface to Pythia8 was expected to become available in a short time.

APPENDIX A

Input parameters for the generation of the $t\bar{t}+$ jets and $Wb\bar{b}$ samples

A.1 Alpgen parameters

The $t\bar{t}jj$ samples were produced with Alpgen version 2.13 and the parton shower was added with HERWIG version 6.510 interfaced with Jimmy version 4.31. The simulated showered events were taken from the official ATLAS MC samples produced with the MC10 parameter defaults and correspond to the dataset numbers 105894-105897. More precisely the datasets used are the following:

```
mc10_7TeV.105890.AlpgenJimmyttbarlnlnNp0_baseline.merge.NTUP_TOP.e600_s933_s946_r2302_r2300_p572_tid366962_00
mc10_7TeV.105890.AlpgenJimmyttbarlnlnNp0_baseline.merge.NTUP_TOP.e600_s933_s946_r2302_r2300_p572_tid366963_00
mc10_7TeV.105891.AlpgenJimmyttbarlnlnNp1_baseline.merge.NTUP_TOP.e600_s933_s946_r2302_r2300_p572_tid366964_00
mc10_7TeV.105891.AlpgenJimmyttbarlnlnNp1_baseline.merge.NTUP_TOP.e600_s933_s946_r2302_r2300_p572_tid366965_00
mc10_7TeV.105892.AlpgenJimmyttbarlnlnNp2_baseline.merge.NTUP_TOP.e600_s933_s946_r2302_r2300_p572_tid366966_00
mc10_7TeV.105892.AlpgenJimmyttbarlnlnNp2_baseline.merge.NTUP_TOP.e600_s933_s946_r2302_r2300_p572_tid366967_00
mc10_7TeV.105893.AlpgenJimmyttbarlnlnNp3_baseline.merge.NTUP_TOP.e600_s933_s946_r2302_r2300_p572_tid366968_00
mc10_7TeV.105893.AlpgenJimmyttbarlnlnNp3_baseline.merge.NTUP_TOP.e600_s933_s946_r2302_r2300_p572_tid366969_00
```

The fixed-order samples were produced locally with Alpgen version 2.14 and using the same input parameters as the showered events. The parameters needed for the event generation are given in the Table A.1. The rest of the input parameters are set to the default values coded in Alpgen. The parameters needed for the parton shower and the multi-parton interactions simulation with HERWIG/Jimmy are given in TableA.2. The MC samples use the tuning parameters of the ATLAS Underlying Event Tune 1 [84].

A.2 HERWIG parameters for $Z/\gamma^{*}b\bar{b}$ showering and hadronization

Table A.3 contains all the necessary input parameters that the user has to input in the driver that interfaces the Matrix Element calculation from aMC@NLO with HERWIG 6.520 for showering and hadronization.

TABLE A.1: Setup for $t\bar{t}jj$ calculation with Alpgen

Parameter	Value
Beam energy	`ebeam`$= 3500$
Top mass	`mt`$= 172.5$
PDF	`ndns`$= 9$ (CTEQ6L1 [85])
Scale functional form	`iqopt`$= 1$ $\left(\mu = \sqrt{\sum m_T^2}\right)$
Parton matching	`ickkw`$= 1$ (for MLM matching)
EW parameter scheme	`iewopt`$= 3$ $(m_W = 80.419\ \text{GeV}, m_Z = 91.188\ \text{GeV}, G_F = 1.16639 \cdot 10^{-5}\ \text{GeV}^{-2})$
CKKW α_s scale	`ktfac`$= 1$
Top decay mode	`itdecmod`$= 4(l\nu qq)$ or `itdecmod`$= 5(l\nu l\nu)$
Light jet veto	`ptjmin`$= 15$ (GeV)
Maximum light-jet rapidity	`etajmax`$= 6$
Maximum b-quark rapidity	`etabmax`$= 6$
Maximum c-quark rapidity	`etacmax`$= 6$
Maximum photon rapidity	`etaphmax`$= 6$
Jet separation $\Delta R_{jj} = \Delta R_{jQ}$	`drjmin`$= 0.7$
MLM clustering energy (E_T^{clus})	`501 20` (20 GeV)
MLM clustering radius (R_{clus})	`502 0.7`
MLM clustering pseudorapidity (η_{clus})	`503 6`
Inclusive or exclusive mode	`504 0` (inclusive) or `504 1` (exclusive)

A.3 aMC@NLO parameters for $Wb\bar{b}$ generation with the ATLAS MC11 defaults

Table A.4 contains the input parameters needed for the generation of the $Wb\bar{b}$ sample with aMC@NLO using the ATLAS MC11 default parameter settings[1] . The parameter `bwcutoff` determines weather a resonance is written in the LHE file. More precisely, if the generated mass of the resonance X is $m_X <$ `bwcutoff` $\cdot\, \Gamma_X$, then X will be written in the event record as an intermediate state and the showering and hadronization generators will not change its mass.

---

[1] We note that the CT10 PDF set used for the calculation contained floating-point format errors in some of the uncertainty eigenvector sets that have to be fixed by
`sed -i.bak 's/[0-9]{7}-[0-9]{3}/0.00000E+00/g' CT10.LHgrid ; rm CT10.LHgrid.bak`.

TABLE A.2: Setup for $t\bar{t}jj$ Parton Shower with HERWIG/Jimmy

Parameter	Value
Cut-off scheme for ISR	`ISPAC`= 2
UE (2 → 2 scattering)	`JMUEO`= 1
Multi-Parton Interactions	`MSFLAG`= 1
Soft Underlying Event	`PRSOFT`= 0
Primordial k_T width	`PTRMS`= 1.2
Inverse proton radius squared	`JMRAD(73)`= 1.69
Minimum p_T of secondary scatters	`PTJIM`= 4.14
$\mathtt{PTJIM} = \mathtt{PTJIM0}\frac{\sqrt{s}}{1800}\mathtt{EXP}$	`PTJIM0`= 2.857 `EXP`= 0.273
PDF set	`AUTPDF=HWLHAPDF` `MODPDF`= 20650 (MRST2007lomod [86])
Mesons/Baryons ratio in B decays	`CLPOW`= 1.2
Lifetime cut (K_s, Λ stable)	`PLTCUT`= 0.0000000000333

TABLE A.3: Setup for $Z/\gamma^* b\bar{b}$ Parton Shower with HERWIG

Parameter	Value
PDF set	`IPDF`= 1,`AUTPDF(I)`=LHAPDF, `AUTPDF(I)`= 23300 MSTW2008NLO [64]
Process number	`IPROC`= −8000 Underlying Event ON with events provided by external LHE file
Λ_{QCD}	`TMPLAM`= −1 (HERWIG default)
Z mass and width	`RMASS(200)`= 91.188, `GAMZ`= 2.4414
W mass and width	`RMASS(198)`= 80.419, `GAMW`= 2.0476
Top mass and width	`RMASS(6)`= 172.5, `GAMT0`= 1.4
Higgs mass and width	`RMASS(201)`= 120 ,`GAMH`= 0.0049
d, u, s, c, b, g masses	`RMASS(1)`= 0.32,`RMASS(2)`= 0.32,`RMASS(3)`= 0.5 `RMASS(4)`= 1.55,`RMASS(5)`= 4.5,`RMASS(13)`= 0.75
$m_e = m_\mu = 0$	`RMASS(121)=0.D0, RMASS(123)=0.D0` `RMASS(127)=0.D0, RMASS(129)=0.D0`
Photon radiation from ISR	`ZMXISR`= 0 (OFF)
Z decay mode	`MODBOS(I)`= 2 Only $Z \to e^+e^-$ decays

TABLE A.4: Setup for $Wb\bar{b}$ generation with aMC@NLO - MC11 defaults

Parameter	Value
Model	`smckmNLO` for massive b quarks and off-diagonal CKM matrix
Proton and Jet parton content	`P dd uu ss cc g`, `J dd uu ss cc g` `maxjetflavor`= 4 (for massive b quarks)
PDFset	`pdlabel 'lhapdf'`, `lhaid 10800` CT10 [87]
Electroweak coupling constant	`alpha_em(MZ)(-1)=1.32348905E+02`
Fermi constant	`G_Fermi 1.16637000E-05`
Strong coupling constant	`alpha_s(MZ) 1.18400000E-01`
Z mass	`9.11876000E+01`
W mass	`MW 8.03990000E+01`
Weinberg mixing angle	`sinthetaW**2 0.22262652E+00`
b quark pole mass	`4.75000000E+00`
Top pole mass	`1.72500000E+02`
Top width	`0.00000000E+00`
Z width	`2.49520000E+00`
W width	`2.08500000E+00`
τ mass	`1.77682000E+00`

CKM Matrix Elements	`Vud 9.74280000E-01 Vus 2.25300000E-01 Vub 3.47000000E-03`
	`Vcd 2.25200000E-01 Vcs 9.73450000E-01 Vcb 4.10000000E-02`
	`Vtd 8.62000000E-03 Vts 4.03000000E-02 Vtb 9.99152000E-01`

Breit-Wigner cutoff	`bwcutoff=100`

References

[1] R. Frederix, S. Frixione, V. Hirschi, F. Maltoni, R. Pittau and P. Torrielli, "*W and Z/γ^* boson production in association with a bottom-antibottom pair*", JHEP **1109** (2011) 061 [arXiv:1106.6019]

[2] The ATLAS collaboration, "*Measurement of the cross section for the production of a W boson in association with b-jets in pp collisions at* $\sqrt{s} = 7$ TeV *with the ATLAS detector*", CERN-PH-EP-2011-132 [arXiv: 1109.1470v1]

[3] J. Iliopoulos, "*Progress in gauge theories*", Rapporteur's talk given at the 17th International Conf. on High Energy Physics, London 1974.

[4] L.D. Landau, Zh. Eksp. Teor. Fiz. **7** 19 (1937), L. Landau, Phys. Z. Sowjetunion **11** 26 (1937).

[5] L. D. Landau, Zh. Eksp. Teor. Fiz. **7** 627 (1937), L. Landau, Phys. Z. Sowjetunion **11** 545 (1937)

[6] P. Higgs, "*Broken Symmetries, Massless Particles and Gauge Fields*", Phys. Lett. **12** (1964) 132.

[7] F. Englert and R. Brout, "*Broken Symmetries, Massless Particles and Gauge Fields*", Phys. Lett. **13** (1964) 321.

[8] P. Higgs, "*Broken Symmetries and the Masses of Gauge Bosons*", Phys. Rev. Lett. **13** (1964) 508.

[9] G.S. Guralnik, C.R. Hagen and T.W.B. Kibble, "*Global Conservation Laws and Massless Particles*", Phys. Rev. Lett. **13** (1964) 585.

[10] P. Higgs, "*Spontaneous Symmetry Breakdown without Massless Bosons*", Phys. Rev. **145** (1966) 1156.

[11] S.L. Glashow, "*Partial Symmetries of Weak Interactions'*", Nucl. Phys. **22** (1961) 279.

[12] A. Salam, "*Renormalizability of Gauge Theories*", Phys. Rev. **127** (1962) 331.

[13] S. Weinberg, "*A Model of Leptons*", Phys. Rev. Lett. **19** (1967) 1264.

[14] M. Gell-Mann, "*A Schematic Model of Baryons and Mesons*", Phys. Lett. **8** (1964) 214.

[15] G. Zweig, "*An $SU(3)$ Model for Strong Interaction Symmetry and its Breaking*", CERN Report No.8182/TH.401

[16] M.Y. Han and Y. Nambu, "*Three-Triplet Model with Double $SU(3)$ Symmetry*", Phys. Rev. **139** (1965) B1006.

[17] R. F. Schwitters, Proc. 1975 Int. Symposium on Lepton-Photon Interactions at High Energies, Stanford, 1975, p. 5.

[18] R. Brandelik *et al.* (TASSO collaboration), "*Evidence for Planar Events in e+e- Annihilation at High Energies*", Phys. Lett. **B86** (1979) 243.

[19] The CTEQ collaboration, "*Handbook of perturbative QCD*".

[20] S. Bethke, "*Experimental Tests of Asymptotic Freedom*", Prog. Part. Nucl. Phys. **58** (2007) 351.

[21] R.P. Feynman, "*Very High-Energy Collisions of Hadrons*", Phys. Rev. Lett. **23** (1969) 1415.

[22] J.D. Bjorken and E.A. Paschos, "*Inelastic Electron-Proton and γ-Proton Scattering and the Structure of the Nucleon*", Phys. Rev. **185** (1969) 1975.

[23] S.D. Drell and T.M. Yan, "*Partons and their Applications in High Energies*", Ann. Phys. **66** (1971) 578.

[24] J.C. Collins and D.E. Soper, "*The Theorems of perturbative QCD*", Ann. Rev. Nucl. Part. Sci. **37** (1987) 383.

[25] R.K. Ellis, W.J. Sterling and B.R. Webber, "*QCD and Collider Physics*", Cambridge University Press.

[26] V.N. Gribov and L.N. Lipatov, Sov. J. Nucl. Phys. **15** (1972) 438.

[27] L.N. Lipatov, Sov. J. Nucl. Phys. **20** (1975) 95.

[28] G. Altarelli and G. Parisi, "*Asymptotic Freedom in Parton Language*", Nucl. Phys. **B126** (1977) 298.

[29] Yu.L. Dokshitzer, Sov. Phys. JETP **46** (1977) 641.

[30] F. Bloch and A. Nordsieck, "*Note on the Radiation Field of the Electron*", Phys. Rev. **52** (1937) 54.

[31] T. Kinoshita, "*Mass Singularities of Feynman Amplitudes*", J. Math. Phys. **3** (1962) 650.

[32] T.D. Lee and M. Nauenberg, "*Degenerate Systems and Mass Singularities*", Phys. Rev. **133B** (1964) 1549.

[33] A.H. Mueller, "*On the Multiplicity of Hadrons in QCD Jets*", Phys. Lett. **104B** (1981) 161.

[34] A.H. Mueller, "*Perturbative Quantum Chromodynamics*", World Scientific.

[35] G.P. Salam, "*Towards Jetography*", [arXiv:0906.1833]

[36] M. Cacciari, G. P. Salam and G. Soyez,"*The anti-kt jet clustering algorithm* JHEP **0804** (2008) 063 [arXiv:0802.1189]

[37] K. Hamilton and P. Nason, "*Improving NLO-parton shower matched simulations with higher order matrix elements*", JHEP **06** (2010) 039 [arXiv:1004.1764]

[38] S. Höche, F. Krauss, M. Schonherr, F. Siegert, "*NLO matrix elements and truncated showers*", JHEP **1108** (2011) 123.

[39] S. Catani, F. Krauss, R. Kuhn and B.R. Webber, "*QCD Matrix Elements + Parton Showers*", JHEP **0111** (2001) 063 [arXiv:hep-ph/0109231].

[40] L. Lönnblad, "*Correcting the Colour-Dipole Cascade Model with Fixed Order Matrix Elements*", JHEP **0205** (2002) 046 [arXiv:hep-ph/0112284]

[41] M.L. Mangano, M. Moretti, F. Piccini, and M. Treccani, "*Matching matrix elements and shower evolution for top-pair production in hadronic collisions*", JHEP **0701** (2007) 013 [arXiv:hep-ph/0611129]

[42] S. Frixione and B.R. Webber, "*Matching NLO QCD computations and parton shower simulations*", JHEP **0206** (2002) 029 [arXiv:hep-ph/0204244]

[43] P. Nason, "*A New method for combining NLO QCD with shower Monte Carlo algorithms*", JHEP **0411** (2004) 040, [arXiv:hep-ph/0409146]

[44] S. Frixione, P. Nason and C. Oleari, "*Matching NLO QCD computations with Parton Shower simulations: the POWHEG method*", JHEP **0711** (2007) 070, [arXiv:0709.2092]

[45] S. Alioli, K. Hamilton, P. Nason, C. Oleari and E. Re, "*Vector boson plus one jet production in POWHEG*", [arXiv:1012.3380v1]

[46] H-L. Lai *et al*, "'New Parton Distributions for Collider Physics", Phys. Rev. **D82** (2010) 074024 [arXiv:1007.2241]

[47] M. Cacciari *et al*, "Updated predictions for the total production cross sections of top and of heavier quark pairs at the Tevatron and at the LHC", JHEP **0809** (2008) 127.

[48] The ATLAS collaboration, "Understanding Monte Carlo Generators for Top Physics", ATL-COM-PHYS-2009-xxx.

[49] K. Nakamura *et al* (Particle Data Group), J. Phys. **G 37** (2010) 075021.

[50] L. Evans and P. Bryant, "*LHC machine*", JINST **3** (2008) S08001.

[51] The ATLAS collaboration, "*The ATLAS Experiment at the CERN Large Hadron Collider*", JINST **3** (2008) S08003.

[52] The ATLAS collaboration, *ATLAS public results*, https://twiki.cern.ch/twiki/bin/view/AtlasPublic/LuminosityPublicResults.

[53] J.M. Campbell, J.W. Huston and W.J. Stirling, "*Hard Interactions of Quarks and Gluons: a Primer for LHC Physics*", Rept. Prog. Phys. **70** (2007) 89 [arXiv:hep- ph/0611148]

[54] S. Dittmaier, P. Uwer and S. Weinzierl, "Next-to-Leading-Order QCD Corrections to $t\bar{t}+$ jet Production at Hadron Colliders", Phys. Rev. Lett. **98** (2007) 262002.

[55] A. Bredenstein, A. Denner, S. Dittmaier and S. Pozzorini, "NLO QCD corrections to top anti-top bottom anti-bottom production at the LHC: 1. quark-antiquark annihilation", JHEP **0808** (2008) 108 [arXiv:0807.1248]

[56] A. Bredenstein, A. Denner, S. Dittmaier and S. Pozzorini, "NLO QCD corrections to top anti-top bottom anti-bottom production at the LHC: 2. full hadronic results", JHEP **1003** (2010) 021 [arXiv:1001.4006]

[57] G. Bevilacqua, M. Czakon, C.G. Papadopoulos and M. Worek, "Dominant QCD Backgrounds in Higgs Boson Analyses at the LHC: A Study of $pp \to t\bar{t} + 2$ jets at Next-To-Leading Order", Phys.Rev.Lett. **104** (2010) 162002 [arXiv:1002.4009]

[58] G. Bevilacqua, M. Czakon, C.G. Papadopoulos and M. Worek, "Hadronic top-quark pair production in association with two jets at Next-to-Leading Order QCD", [arXiv:1108.2851]

[59] J.H. Kühn and G. Rodrigo, "*Charge asymmetry of heavy quarks at hadron colliders*", Phys. Rev. **D59** (1999) 054017 [arXiv:hep-ph/9807420v1]

[60] The CDF collaboration, "*Evidence for a Mass Dependent Forward-Backward Asymmetry in Top Quark Pair Production*", Phys.Rev. **D83** (2011) 112003 [arXiv:1101.0034]

[61] The ATLAS collaboration, "*Expected Performance of the ATLAS experiment - Detector, Trigger and Physics*", [arXiv:0901.0512]

[62] M.L. Mangano, "*Standard Model Backgrounds to Supersymmetry Searches*", Eur. Phys. J. **C59** (2009) 373.

[63] M. V. Garzelli, A. Kardos and Z. Trócsányi, "*NLO event samples for the LHC*", [arXiv:1111.1446]

[64] A.D. Martin, W.J. Stirling, R.S. Thorne, and G. Watt, "*Parton Distributions for the LHC*", Eur. Phys. J. **C63** (2009) 189 [arXiv:1007.3178]

[65] M.L. Mangano, M. Moretti, F. Piccinini, R. Pittau and A. Polosa, "*ALPGEN, a generator for hard multiparton processes in hadronic collisions*", JHEP **0307** (2003) 001[arXiv:hep-ph/0206293]

[66] G. Gorcella *et al*, "*HERWIG 6.5: an event generator for Hadron Emission Reactions With Interfering Gluons (including supersymmetric processes)*", JHEP **0101** (2001) 010 [arXiv:hep-ph/0011363]

[67] J.M.Butterworth, J.R.Forshaw and M.H.Seymour, "*Multiparton Interactions in Photoproduction at HERA*", Z. Phys. **C72** (1996) 637 [arXiv:hep-ph/9601371]

[68] S. Alioli, P. Nason, C. Oleari and E. Re, "*Vector boson plus one jet production in POWHEG*", JHEP **1101** (2011) 095 [arXiv:1009.5594v1]

[69] The ATLAS collaboration, "*ATLAS sensitivity to the Standard Model Higgs in the HW and HZ channels at high transverse momenta*", ATL-PHYS-PUB-2009-088 (2009).

[70] H-S. Goh and S. Su, "*Phenomenology of the left-right twin Higgs model*", Phys. Rev. **D75** (2007) 075010 [arXiv:hep-ph/0611015]

[71] The CDF collaboration, "*First measurement of the b-jet cross section in events with a W boson in $p\bar{p}$ collisions at $\sqrt{s} = 1.96$ TeV*", Phys. Rev. Lett. **104** (2010) 131801 [arXiv:0909.1505]

[72] V. Hirschi, R. Frederix, S. Frixione, M.V. Garzelli, F. Maltoni and R. Pittau, "*Automation of one-loop QCD corrections*", JHEP **1105** (2011) 044 [arXiv:1103.0621]

[73] J. Alwall *et al*, "*MadGraph/MadEvent v4: The New Web Generation*", JHEP **0709** (2007) 028 [arXiv:arXiv:0706.2334]

[74] V. Hirschi, "*New developments in MadLoop*", PoS(RADCOR2011)018 [arXiv:1111.2708]

[75] J. Alwall, M. Herquet, F. Maltoni, O. Mattelaer and T. Stelzer, "*MadGraph 5 : Going Beyond*", JHEP **1106** (2011) 128, [arXiv:1106.0522]

[76] R. Frederix, S. Frixione, F. Maltoni andT. Stelzer, "*Automation of next-to-leading order computations in QCD: the FKS subtraction*", JHEP **0910** (2009) 003 [arXiv:0908.4272]

[77] S. Frixione, Z. Kunszt and A. Signer, Nucl. Phys. **B467** (1996) 399 [arXiv:hep-ph/9512328]

[78] G. Ossola, C.G. Papadopoulos and R. Pittau, "*Reducing full one-loop amplitudes to scalar integrals at the integrand level*", Nucl.Phys. **B763** (2007) 147 [arXiv:hep-ph/0609007]

[79] G. Ossola, C.G. Papadopoulos and R. Pittau, "*CutTools: a program implementing the OPP reduction method to compute one-loop amplitudes*", JHEP **0803** (2008) 042 [arXiv:0711.3596]

[80] E. Boos *et al*, "*Generic User Process Interface for Event Generators*", [arXiv:hep-ph/0109068]

[81] S. Badger, J. M. Campbell, and R. K. Ellis, "*QCD corrections to the hadronic production of a heavy quark pair and a W-boson including decay correlations*", JHEP **03** (2011) 027, [arXiv:1011.6647]

[82] M. Bahr *et al.*, "*Herwig++ Physics and Manual*", Eur. Phys. J. **C58** (2008) 639 [arXiv:0803.0883v3]

[83] H.-U. Bengtsson, "*The Lund Monte Carlo for high-p_T physics*", Comput. Phys. Commun. **31** (1984) 323.
H.-U. Bengtsson and G. Ingelman, "*Improved Lund Monte Carlo for high-p_T physics*", Comput. Phys. Commun. **34** (1985) 251.
H.-U. Bengtsson and T. Sjöstrand, "*The Lund Monte Carlo for hadronic processes PYTHIA version 4.8*", Comput. Phys. Commun. **46** (1987) 43.
T. Sjöstrand, "*High-energy-physics event generation with PYTHIA 5.7 and JETSET 7.4*", Comput. Phys. Commun. **82** (1994) 74.

[84] A.G. Buckley and H. Schulz, "*First tuning of HERWIG/JIMMY to ATLAS data*", ATL-COM-PHYS-2010-620

[85] J. Pumplin *et al*, "*New Generation of Parton Distributions with Uncertainties from Global QCD Analysis*", JHEP **0207** (2002) 012 [arXiv:hep-ph/0201195]

[86] A. Sherstnev, and R.S. Thorne, "*Parton Distributions for LO Generators*", Eur.Phys.J. **C55** (2008) 553 [arXiv:0711.2473]

[87] H-L. Lai *et al*, "*New parton distributions for collider physics*", Phys.Rev. **D82** (2010) 074024 [arXiv:1007.2241]